DIGITAL ACCESS TO SCHOLARSHIP AT HARVARD
DASH.HARVARD.EDU

HARVARD LIBRARY
Office for Scholarly Communication

The Sensory and Behavioral Basis of Drosophila Larval Phototaxis

Citation

Kane, Elizabeth Anne. 2012. The Sensory and Behavioral Basis of Drosophila Larval Phototaxis. Doctoral dissertation, Harvard University.

Permanent link

http://nrs.harvard.edu/urn-3:HUL.InstRepos:10344927

Terms of Use

This article was downloaded from Harvard University's DASH repository, and is made available under the terms and conditions applicable to Other Posted Material, as set forth at http://nrs.harvard.edu/urn-3:HUL.InstRepos:dash.current.terms-of-use#LAA

Share Your Story

The Harvard community has made this article openly available.
Please share how this access benefits you. Submit a story .

Accessibility

© 2012 -*Elizabeth Anne Kane*
All rights reserved.

Aravinthan D. T. Samuel Elizabeth Anne Kane

The sensory and behavioral basis of *Drosophila* larval phototaxis

Abstract

The avoidance of light by fly larvae has been studied for over a century. Early 20th-century investigators found that larvae crawled away from light sources incident at an angle (e.g. a sunlit window). Contemporary studies project light from directly above or below and find that larvae accumulate in shadows and have stereotyped responses to sudden changes in light intensity. Now, as then, both the sensory and behavioral mechanisms for phototaxis remain controversial. Here, I unify the historic and modern approaches in the *Drosophila* larva using a novel apparatus and high-resolution behavioral analysis to allow for the precise quantification of larval movement in response to photosensory inputs. Larval locomotion is composed of sequences of runs (periods of forward movement) that are interrupted by abrupt turns, where the larva pauses and sweeps its head back and forth (head-sweeping) until it begins a new run in a new direction. My analysis reveals that the larva uses head-sweeps as spatiotemporal probes of local light information to determine the direction of successive runs. I find all forms of phototaxis are mediated by the same sensorimotor transformation and establish the necessity of the larval eye to decode the direction of incident light. This work provides the necessary foundation for the decryption of the neural circuits controlling phototaxis.

Contents

1 Introduction **1**

1.1 A systems level understanding of behavior 1

1.2 The *Drosophila melanogaster* larva as a model for systems neuroscience 2

1.3 Navigational strategies 2

1.3.1 Kineses 2

1.3.2 Taxes 3

1.4 Larval phototaxis and photosensation 3

1.4.1 Historical studies 3

1.4.2 Contemporary studies 8

1.4.3 Phototaxis circuit 10

1.4.4 non-Rhodopsin mediated photoreception 12

1.5 Motivation for thesis work 12

2 The sensory and behavioral basis of *Drosophila* larval phototaxis **14**

2.1 Introduction 14

2.2 Results 15

2.2.1 Checker lightscape navigation 15

2.2.2 Square-wave temporal lightscape 20

2.2.3 Linear spatial gradient lightscape 23

2.2.4 Triangle-wave temporal lightscape 24

2.2.5 Directional lightscape navigation 24

2.3 Discussion 33

2.4 Materials and Methods 35

2.4.1 Strains 35

2.4.2 Phototaxis apparatus . . . 36
2.4.3 Light intensity determination . . . 36
2.4.4 Behavior experiments . . . 39
2.4.5 Laser Ablation . . . 42
2.4.6 Microscopy . . . 43
2.5 Accompanying Videos . . . 43
2.5.1 Video 1 . . . 43
2.5.2 Video 2 . . . 43
2.5.3 Video 3 . . . 44
2.5.4 Video 4 . . . 44
2.5.5 Video 5 . . . 45
2.5.6 Video 6 . . . 45
2.6 Acknowledgements . . . 45
2.7 Author contributions . . . 46
2.8 Manuscript information . . . 46

3 A screen to identify phototaxis circuit components 47
3.1 Introduction . . . 47
3.2 Strategy for identifying phototaxis circuit neurons . . . 48
3.2.1 Janelia Farm GAL4 collection . . . 48
3.2.2 Design of primary and secondary screens . . . 49
3.2.3 Behavioral assays to determine defects in phototaxis circuit function . . . 49
3.3 Progress . . . 51
3.4 Contribution notes . . . 51

4 Appendix1: Rictor/TORC2 regulates fat metabolism, feeding, growth and life span in *Caneorhabditis elegans* 60
4.1 Authors . . . 60
4.2 Publication note . . . 60
4.3 Abstract . . . 61
4.4 Introduction . . . 61
4.5 Results . . . 63

4.5.1 Identification and expression of the *C. elegans* homolog of Rictor, RICT-1 63
4.5.2 RICT-1 regulates fat mass and the response to different diets 64
4.5.3 RICT-1 partially regulates fat via insulin-like signaling through AKT 68
4.5.4 RICT-1 regulates life span in a diet-dependent manner . . 74
4.5.5 Insulin-like signaling through AKT is necessary but not sufficient for the short life span of *rict-1* mutants 76
4.5.6 Mutations in *sgk-1* phenocopy and do not enhance *rict-1* growth, reproductive, and life-span defects 76
4.5.7 RICT-1/TORC2 regulates fat mass through AKT and SGK . 82
4.5.8 RICT-1 regulates fat mass and whole organism growth via the intestine 85
4.6 Discussion 86
4.6.1 RICT-1 acts through SGK-1 to regulate life span, growth, reproduction, and both SGK-1 and AKT to regulate fat mass 86
4.6.2 RICT-1 and SGK-1 modulate life span in a nutrient-dependent manner 87
4.6.3 Fixative-based fat staining differs from labeling with BODIPY-labeled fatty acids in the case of the insulin-like signaling pathway mutants 89
4.6.4 Genetic pathways upstream of and downstream from RICT-1/TORC2 89
4.7 Materials and Methods, Supplemental Figures 91
4.7.1 Strains used 91
4.7.2 Body fat assessment 92
4.7.3 Pharyngeal pumping rates 93
4.7.4 Oxygen consumption 93
4.7.5 Brood size determination 94
4.7.6 Body size determination 94
4.7.7 Egg-to-egg time 94
4.7.8 Feeding RNAi 94
4.7.9 Longevity assay 95
4.7.10 Gompertz-Makeham survival analysis 95

4.8 Acknowledgements . . . 95
4.9 Author contributions . . . 96
4.10 References . . . 96

5 Appendix 2: Two alternating motor programs drive navigation in *Drosophila* larva 120
5.1 Authors . . . 120
5.2 Publication note . . . 120
5.3 Abstract . . . 121
5.4 Introduction . . . 121
5.5 Results . . . 123
5.5.1 Visualizing motor dynamics in freely moving larvae . . . 123
5.5.2 Motor dynamics during navigational decision-making . . . 128
5.6 Discussion . . . 137
5.7 Materials and Methods . . . 141
5.7.1 Fly strains . . . 141
5.7.2 Image acquisition and tracking . . . 141
5.7.3 Image analysis . . . 142
5.7.4 Statistical procedures . . . 143
5.8 Videos . . . 144
5.8.1 Video 1 . . . 144
5.8.2 Video 2 . . . 144
5.8.3 Video 3 . . . 144
5.8.4 Video 4 . . . 144
5.8.5 Video 5 . . . 145
5.9 Acknowledgments . . . 145
5.10 Author Contributions . . . 145
5.11 References . . . 145

6 Appendix 3: Controlling airborne cues to study small animal navigation 148
6.1 Authors . . . 148
6.2 Publication note . . . 148
6.3 Abstract . . . 148
6.4 Introduction . . . 149

6.5 Results . . . 150
6.5.1 Gradient generation . . . 150
6.5.2 Behavioral analysis . . . 152
6.5.3 Navigation in spatial gradients . . . 154
6.5.4 Navigation in temporal gradients . . . 158
6.6 Discussion . . . 161
6.7 Methods . . . 162
6.7.1 Strains . . . 162
6.7.2 Odor gradient apparatus . . . 162
6.7.3 Behavior experiments . . . 164
6.7.4 Behavioral analysis . . . 165
6.7.5 Statistical model for heading change distributions after turns . . . 166
6.7.6 Supplementary Methods . . . 167
6.7.7 Camera and Lighting . . . 173
6.7.8 Calibration of Temporal Gradients . . . 175
6.7.9 MAGAT analyzer algorithms . . . 176
6.8 Videos . . . 179
6.8.1 Video 1 . . . 179
6.8.2 Video 2 . . . 179
6.8.3 Video 3 . . . 179
6.8.4 Video 4 . . . 180
6.8.5 Video 5 . . . 180
6.8.6 Video 6 . . . 180
6.9 Acknowledgements . . . 180
6.10 Author contributions . . . 181
6.11 References . . . 181

Dedicated to my parents, Kenneth and Margaret Kane, and my aspiring scientist fiancé, Jeremy Todd.

Author List

The author for Chapter 1 is Elizabeth A. Kane.

The authors for Chapter 2 are Elizabeth A. Kane, Marc Gershow and Aravinthan D. T. Samuel.

The author for Chapter 3 is Elizabeth A. Kane.

Acknowledgments

This thesis is the culmination of help by many individuals over the past five years. I cannot hope to list them all here, but I'd like to thank a few of the most important.

First, my advisor, Aravinthan D. T. Samuel, for taking a chance on a second year graduate student with no background in the physical training his lab is founded on. Aravi's thoughtful mentorship, guidance and integrity make the lab a uniquely friendly and intensely collaborative place to pursue ambitious science. It is hard to imagine a better place to be a graduate student. I also owe thanks to my unofficial co-mentor and friend, Benjamin de Bivort, for putting me in touch with Aravi and countless scientific discussions over the years.

In the Samuel lab, Marc Gershow, has been my right-hand man, teaching me the basics of programming and engineering and never failing to help me solve a seemingly insurmountable problem. The influence of his ambitiousness, drive and diligent nature have undoubtedly raised the quality of my graduate work. I thank Mason Klein for his help on everything from optics to proposals, and for sharing countless lab snacks with me. I thank Ashley Carter for help with preliminary experiments and showing me the ropes when I first joined the Samuel lab. I also thank the other graduate students in the Samuel lab, Ashley Vonner and Andrew Leifer, for critical graduate student solidarity.

I have had the pleasure of working with three gifted undergraduates: Kristen Hunter, Samantha Whitmore and Hanna Retallack. I thank them for their dedication and refreshing enthusiasm.

Thanks to our collaborators, Simon Sprecher and Paul Garrity, for reagents and critical scientific thinking and advice.

I would like to thank my undergraduate research advisor, Justin Blau, for his challenging yet encouraging guidance, and for inspiring me to pursue an academic career path.

Thanks to the members of my Dissertation Advisory Committee: Howard Berg, Paul Garrity, David Van Vactor, and Benjamin de Bivort; and my Defense Committee: David Van Vactor, Michael Francis, Hopi Hoekstra and Sam Kunes. Thanks to the members of the Biological and Biomedical Sciences administrative office: Kate

Hodgins, Maria Bollinger and Stephen Obuchowski.

I am fortunate to unwavering support of my my parents, Margaret and Kenneth Kane. They have always been incredibly supportive of my scientific curiosities. I thank them for allowing me to turn their house into an amateur science lab whenever I wished. I also thank my sister and missed former-roommate, Victoria Kane, for her support. And although they can't read this, I thank my dogs, Thistle and Ellie, for their wagging tails and happy faces, which never failed to brighten even the most challenging of graduate school days. They put the "companion" in "companion animal."

Lastly, I want to thank my soon-to-be husband, Jeremy Todd, who has played many different supportive roles throughout graduate school: copy editor, dog care-taker, kite boarding instructor. The energy he brings to all of his interests is contagious, and his zest for the uncharted is a wonderful balancing force in my life that has inspired me in many ways.

I received financial support from the National Institute of Health National Research Service Award under grant number NS073325-01.

1 Introduction

1.1 A systems level understanding of behavior

A central goal of systems neuroscience is to determine how behavior is encoded in the organization and function of the nervous system. Vertebrate nervous systems can be so complex (the human brain contains 100 billion neurons, a veritable "cathedral of complexity" [13]), that behavior cannot be comprehensively understood at the neural and molecular levels. For comprehensive understanding of behavior and brain, one must turn to tractable genetic model organisms, like the *Drosophila melanogatser* larva, which has fewer than 10,000 neurons in its central brain [60]. With simpler, smaller animals, one can hope to gain a systems level understanding of behavior and principles of neuroscience that apply to all animals.

1.2 The *Drosophila melanogaster* larva as a model for systems neuroscience

The *Drosophila* larva is rapidly becoming a favored model for systems neuroscience owing to its robust genetically encoded behaviors, optical accessibility, relatively compact central nervous system and powerful genetic tool-kit.

1.3 Navigational strategies

Reports of the organized movements animals employ to seek out preferred regions in their environment are among the oldest and most comprehensive studies of animal behavior. The specific navigational strategy utilized by an organism can be inferred from a thorough characterization of its movement in response to defined spatiotemporal stimulus environments. The canonical orienting reaction used to introduce the concept of navigational strategies is a biased random walk, best studied in the context of *Escherichia coli* navigation in chemosensory gradients [6, 7]. *E. coli's* biased random walk is composed of two alternating behavioral states: runs, periods of forward movement where the cell's flagellar motor counter-clockwise rotation propels it along a straight path, and tumbles, where the cell's flagellar motor changes its rotation direction to clockwise, causing the cell to tumble chaotically and reorient to a new direction. In order to find preferred odorant environments, *E. coli* modulate their tumbling probability as a function of the temporal derivative of odorant concentration. If the odorant is attractive, the cell will decrease its tumbling probability when the derivative is positive, resulting in longer runs towards the preferred direction. The timing and direction of these reorientation events are intrinsically random, hence the name, biased random walk.

1.3.1 Kineses

Although colloquially referred to as chemotaxis, *E. coli*'s movement in chemosensory gradients is actually an example of kinesis, defined as a behavior in which reorientations are lacking a directional reorientation bias. Kineses can be subdivided into two types: ortho-kineses, in which the speed of forward movement depends on the stimulus intensity (observed in woodlice navigating humidity gradients [25]) and klino-kineses, in which the frequency of turning is dependent on

the intensity of the stimulus (as is the case for *E. coli* navigating in chemosensory gradients [7]) [17].

1.3.2 Taxes

Orientation reactions where an animal's turning movement is directed toward or away from a stimulus are known as taxes, which result in more efficient navigation than kineses. Taxes can also be subdivided into two types based on the method by which the animal extracts spatial information about the orienting stimulus: klino-taxes and tropo-taxes. In klino-taxis, the stimulus direction is determined by a temporal comparison of stimulus intensity, usually by sequential sampling. Since klino-kineses rely on temporal sampling, they can be performed with a single point sensor. In tropo-taxis, the animal computes the stimulus direction instantaneously via a spatial comparison between two identical sensors.

1.4 Larval phototaxis and photosensation

1.4.1 Historical studies

Phototaxis

The navigational strategy underlying the avoidance of light by common fly larvae has been studied for over a century. It was first investigated by Georges Pouchet in 1872 in the maggots of the green-bottle (*Lucilia caesar*) and the blue-bottle or blow-fly (*Calliphora erythocephala*) [54]. He observed that larvae feeding on rotting meat were located on its surface during the night, but were hidden by day, found instead burrowed into the food. This observation prompted him to investigate the behavior of larvae under different light conditions. In his first experiments, he placed fly larvae on a table that was lit on one side by either daylight or artificial light and observed that the larvae crawled away from the lit side. To ensure that this effect was not due to heat emanating from the light, he replaced the light with a large bowl of hot water and observed that larvae instead crawled toward the bowl. Taken together, these experiments demonstrate that larvae exhibit a light-avoiding (photophobic) reaction.

Soon after Pouchet's work, Jacques Loeb began studying the reactions of animals to light with the goal of explaining their behavior in terms of physical and

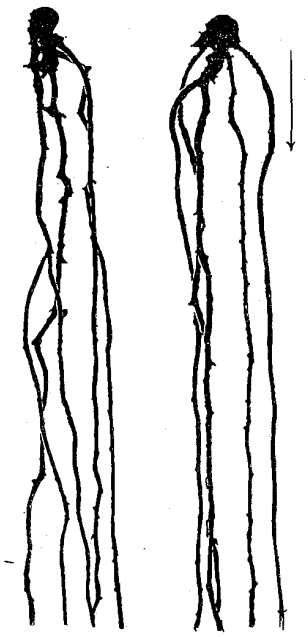

Figure 1.1: Tracks of ten larvae moving away from light-rays, indicated by arrow in upper right corner. Tracks were made by placing a drop of methylen blue on the larva navigating on paper. From [8].

chemical reactions taking place within the animal [46]. This represented a shift from the anthropomorphic descriptions of behavior (i.e., "animals moved toward light because it aroused their curiosity") that had marked the previous century. Loeb was heavily influenced by the studies of plant heliotropism, which at the time explained the bending of plants toward sunlight as a consequence of asymmetrical chemical reactions due to the local difference in light intensity on the plant's surface. Loeb adapted this idea in his "tropism theory", which states that bilateral body plans allow animals to extract spatial information about their environment through the sensation of external forces acting asymmetrically on symmetric body halves.

Loeb cited his studies of fly larval light avoidance as supporting evidence for the tropism theory. He observed that *Musca vomitoria* larvae can orient themselves parallel to incident light rays (Figure 1.1), with their heads pointing away from the light source, stating that:

> "They crept with a mathematical precision in the direction of the rays...They acted as though they were impaled on a ray of light which

passed through their median plane." [45]

He theorized that this orientation could be explained as a consequence of the light inducing an asymmetrical reaction in the larva's body that was proportional its intensity, with the more intensely illuminated side being more activate than the other. Thus, larval light avoidance was the result of larvae acting to balance the two light-induced chemical reactions on each left-right body half (an example of tropo-taxis). If light was shining with greater intensity on the right half of the larva, the less-active left side would be relatively contracted, causing the larva to turn its head to the left, away from the light. This asymmetrical contraction would continue until the larva balanced the light intensity on each half, so that it was crawling directly away from the light [45–47].

Loeb believed that he had found proof of his theory when he observed that larvae exposed to light from two windows would crawl perpendicularly to the line connecting the light rays coming from each window. If Loeb's theory were correct, it makes the prediction that larvae should display an ortho-kinetic reaction, crawling faster in higher intensity light. Although Loeb did not look for this effect himself, two of his colleagues, Samuel Ottmar Mast and Wiliam Hermes, determined the time it took fly larvae to travel a fixed distance in high and low intensity light and found no substantial difference [31, 49], refuting Loeb's theory.

Many of Loeb's contemporaries disagreed with his tropo-tactic explanation of the light responses of fly larvae. Loeb substantially resisted these criticisms, even as other investigators were collecting mounting evidence to the contrary, which became known as the "tropism controversy" among ethologists in the early- to mid-1900s.

A main critic of Loeb, Samuel Holmes, observed the crawling of the fly larva in isotropic environments and noted that larvae have two primary movements: (1) the forward crawling achieved by the coordinated motion of the larva thrusting its anterior end straight forward, followed by a peristaltic contraction from posterior to anterior and (2) the swinging of the larva's anterior from side-to-side via the asymmetrical contraction of the head segments [34, 35]. The same movements were observed in the presence of light or other stimuli. Holmes noted that if the larva is suddenly exposed to light, it will often initiate the side-to-side movements of its head. This led Holmes to theorize that larvae orientat themselves by "trial

and error." He stated,

> "If a strong light is thrown upon a larva from one side it may swing the head either towards or away from the light. If the head is swung towards the light, it may be withdrawn or flexed in the opposite direction... If it is turned away from the light the larva usually follows up the movement by (forward) locomotion....The orientation of these forms is essentially a selection of favorable chance variations of action and following them up." [34]

Importantly, the initial direction that the larva swings its head is random. However, random head swinging that results in movement toward preferable lower light intensity environments is followed up by forward locomotion.

In his doctoral thesis at Harvard University, Bradley Patten quantitatively described the orientating reaction of blow-fly larvae in response to two opposing beams of light [52]. He systematically varied the intensities of the two beams and quantified in exacting detail the resulting path taken by individual larvae. Similar to Loeb, he observed that some larvae will orient themselves perpendicular to the line connecting two light rays. After watching the head swinging movements of individual larvae, Patten believed that their orientation was achieved by the trail and error means suggested by Holmes. Curiously, he also observed a large majority of larvae that appear to have an innate orientation bias toward a particular side, as if the light intensity perceived on that side is brighter than its actual intensity. These animals oriented reliably to angular deflection of the perpendicular line. Patten was able to correct for this angular deflection by adjusting the relative intensities of the lights.

An important experiment by Gottfried Fraenkel and Donald Gunn further supports the idea that the larva does not have or cannot act on information regarding light ray direction or intensity before its trial head swinging movements [18]. They placed larvae on a piece of ground glass that was illuminated from above. They watched the movements of the larva and as it began to swing its anterior end to the right, they would turn on an additional lamp, increasing the light intensity (Figure 1.2). This manipulation of light intensity was sufficient to induce the larva to turn to the left, such that its path was composed of counter-clockwise

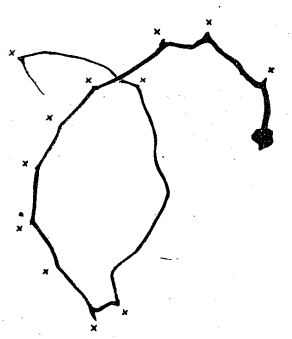

Figure 1.2: An example track from a larva that was illuminated from above every time it turned toward the right. From [8].

circular movements.

The identification of Bolwig's Organ, the larval eye

The fact that larvae orient their heads parallel to the direction of light rays, possibly so that their head is maximally shaded by their body, suggests that the larva's anterior contains the light-sensitive structures for phototaxis. The identification of the light sensitive organs proved to be rather difficult, and in fact they weren't properly identified until more than half a century after the initial studies of larval light avoidance. Initially, Pouchet erroneously thought that the imaginal discs of the larva were the light sensitive organs. Many others believed that the "conical tubercles" present on the larva's cephalic oral lobes were the principle photosensory structure, noting their eye-like appearance consisting of a round chitinized ring that was covered by an external transparent sheet of cuticle.

William Herms [30, 31] and Joe Ellsworth [16] tried to localize the larval photosensory structure by shining a 2 mm small spot of light onto the anterior end of the larva. They were able to conclusively localize the light sensitive structures to the larval head, but the spot was too large to discriminate between the cephalic lobes or any other part of the larva's head. In his doctoral thesis, Neils Bolwig [8] was able to further reduce the size of the light spot to 0.20 mm and observed the responses of larva under dark room illumination (to which larvae are insensitive) in relation to the location of the light spot. From these experiments, Bolwig was able to conclude that the cephalic lobes do not contain any photosensory structures. The cephalic lobes are now known as the dorsal organ, the larva's primary

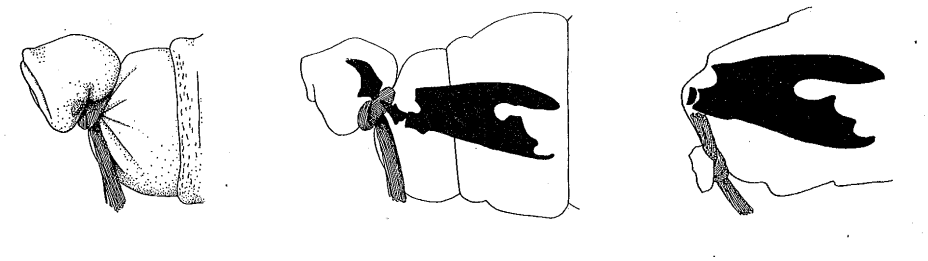

Figure 1.3: Sketches from Bolwig's vivisection experiments to determine the location of the fly larval eye. Left, anterior portion to be removed was tied off from the rest of the larval body by a fine string. Middle, the precise location of the string relative to the cephalopharyngeal skeleton was noted. Right, the anterior portion of the larva above the string was removed using surgical forceps. From [8].

olfactory structure [4, 28, 60].

To determine the larval photosensory structure, Bolwig completed a series of technically remarkable vivisection experiments on house fly larvae [8]. He carefully removed varying amounts of larval head thoracic segments by tying a fine string around the larva, such that the head segments that would be removed were hanging from the front of the larva, like a sac. He then used a pair of surgical tweezers to remove the segments in front of the string (Figure 1.3) . Surprisingly, larvae could survive for many days after the surgery. Bolwig then quantified the larval directional light orientation response in his post-surgery larvae. He conducted several thousand surgeries before localizing the light sensitive organs to a cluster of cells lining a pouch near the condyle spine of the cephalopharyngeal skeleton, which send a single nerve posteriorly to the brain. This organ later became known as Bolwig's Organ.

1.4.2 Contemporary studies

Phototaxis

The large majority of contemporary studies of larval phototaxis quantify aggregation in binary choice assays, measuring the percentage of animals that dwell in the dark or light half of a Petri plate (referred to as the binary assay from now on) [5, 12, 22, 27, 39, 40, 51, 58]. In addition to the binary assay, Ana Campos' group

developed a temporal on-off assay to quantify the larval response to brief light pulses [10, 26, 56, 59]. Using the outline of the larval body, they found that the larva is more likely to change direction when the lights turn on. However, their analysis was limited to the animal's center of mass only (this is the only parameter extracted from their videos of larval behavior), so they were unable to analyze the head swinging behavior that was hypothesized to underly larval light avoidance by early ethologists.

Bolwig's Organ

The Bolwig's Organ can be easily visualized in an overhead view of an intact larva owing to its transparent cuticle (Figure 1.4). Recent molecular studies have determined that the Bolwig's Organ is composed of two photoreceptor subtypes: a cluster of eight neurons which express the green-peaked *Rhodopsin-6* (*Rh6*), and a cluster of four neurons that express the blue-peaked *Rhodopsin-5* (*Rh5*). Unfortunately, knowledge of the cellular structure of Bolwig's Organ has not advanced significantly since its discovery. It is thought that the Bolwig's Organ is composed of ciliary photoreceptors[1], but this has not been conclusively determined by electron microscopy.

Although little is known about its structure, the genetic programs and intracellular signaling cascades that mediate photoreception in the Bolwig's Organ have been well studied. The homeobox transcription factor *sine oculis* and the zinc-finger-containing transcription factor *glass* are both required for proper Bolwig's Organ morphogenesis [14, 15, 61]. Larval mutants in either gene display morphological defects in Bolwig's Organ and fail to accumulate in low luminosity regions using the binary assay. Additionally, there is behavioral evidence that Bolwig's Organ phototransduction is mediated by the canonical adult photoreceptor signaling cascade; mutants disrupting the essential adult photoreceptor phototransduction signaling cascade genes *no receptor potential* (*norpA*), the fly homologue of phospholipase C, and *transient-receptor potential* (*trp*) also fail to aggregate in binary assays [27, 59]. Double mutants lacking both of the larvally expressed Rhodopsins (*Rh5*; *Rh6*) also fail to phototax [12, 40, 50]. Recent work has shown that only

[1] Personal communication with Volker Hartenstein.

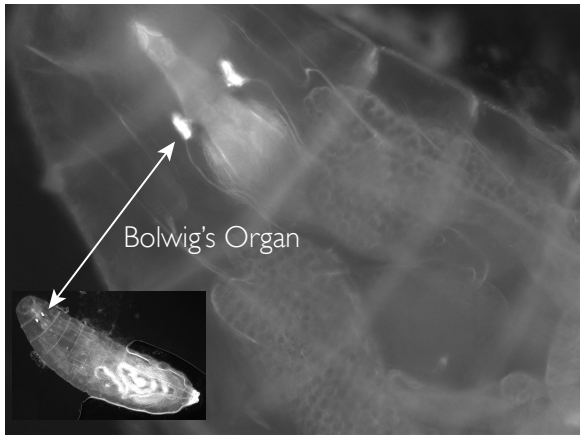

Figure 1.4: Bolwig's Organ is the larval eye, visualized using the *Rhodopsin-6* promoter to direct expression of Green Fluorescent Protein (GFP).

the *Rh*5 photoreceptor subset of the Bolwig's Organ is essential for phototaxis [12, 27, 40], whereas either photoreceptor subtype can relay light information to entrain the molecular rhythms of the larva's circadian clock [40].

1.4.3 Phototaxis circuit

There has been significant effort to identify neurons in the phototactic circuit. Unfortunately, the literature contains many conflicting reports, likely due to the relative simplicity of the binary assay used by the majority of studies [22, 27, 39, 40, 50]. There are multiple studies reporting a role for the larval circadian clock neurons in phototaxis, which is composed of three groups of bilaterally symmetric neurons that express the essential circadian clock gene, *timeless* (*tim*), a transcription factor: the small lateral neurons (s-LNs), the dorsal neurons group 1(DN1) and dorsal neurons group 2 (DN2) (Figure 1.5). The s-LNs can be further subdivided: 4 neurons express the neuropeptide Pigment Dispersing Factor (PDF), whereas the fifth neuron is PDF negative. It is likely that the PDF positive s-LNs are disposable for phototaxis; electrically silencing them by inward rectify-

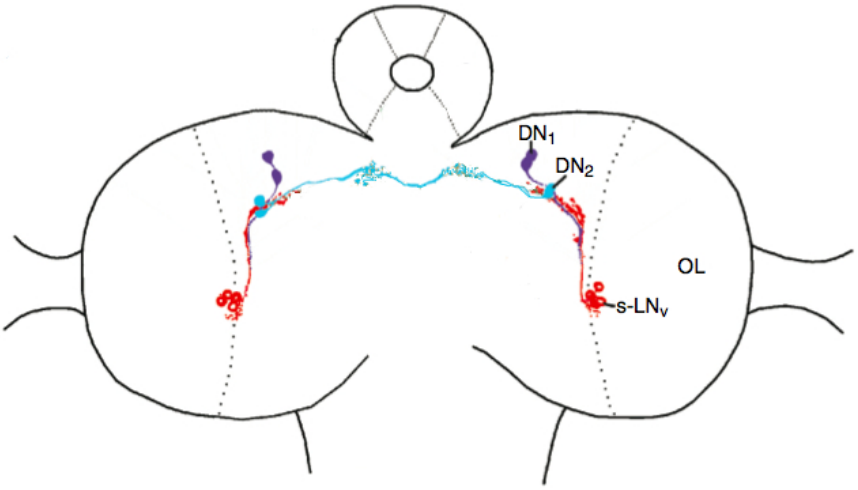

Figure 1.5: The larval brain (black outline) showing the location of the three clock circuit neuron groups and their projections. s-LNv (small Lateral Neurons, DN1, Dorsal Neurons group 1, DN2, Dorsal Neurons group 2, OL, optic lobe. Adapted from [29].

ing potassium channels or genetically ablating them does not affect aggregation in the binary assay. However, genetic ablation or electrical silencing of all *tim* neurons disrupts behavior in the binary assay, with larvae segregating equally between low and high luminosity regions [12, 27, 40]. Silencing just the DN1 and the fifth PDF negative s-LNs also disrupts light avoidance in the binary assay, suggesting that these three neurons, which are likely responsible for the defective phototaxis phenotype observed when all *tim* neurons are silenced, are bona fide circuit components [12, 40]. Two additional neurons that are post-synaptic to the PDF expressing s-LNs reverse larval light avoidance from photo-negative to photo-positive when silenced electrically or synaptically [23].

Work by the Sprecher group has identified sets of candidate phototaxis neurons by a scanning transmission electron reconstruction of the larval optic neuropil (LON, the axon bundle formed by the Bolwig's Organ nerve) [63]. They found that the *Rh5* and *Rh6* photoreceptor axon bundles occupy distinct compartments within the LON, suggesting that they synapse onto different target neurons. Additionally, they find that the projections of individual photoreceptors are spatially

organized, probably reflecting their position in the larval eye (a primitive retinotopy). The s-LNs, including the fifth PDF negative s-LN, extend dendritic arbors into the LON and form bona-fide synapses onto the LON. The LNs then send their axons to the dorsal protocerebrum, a theorized region of higher order sensory processing.

1.4.4 non-Rhodopsin mediated photoreception

A recent paper [67] has shown that larvae are capable of sensing light at high intensities without a functioning Bolwig's Organ via their class IV multidendritic neurons that tile the larval body wall. Multidendritic neurons were previously known to be involved in the peristaltic wave propagation underlying forward movement and the response to nociceptive heat and mechanical stimuli [24, 36, 37, 68]. Surprisingly, class IV multidendritic neuron photoreception is not mediated via the canonical rhodopsin signaling cascade. Instead, it is theorized that the rhodopsin-like gustatory receptor, *Gr28b* mediates primary photoreception and signals intracellularly to the Transient Receptor Potential A1 (TRPA1) cation channel [67]. The relative contribution of the class IV multidendritic neurons to light avoidance is unknown.

1.5 Motivation for thesis work

Nervous systems are computational by their very nature. They turn sensory inputs into neural representations and memories, and then use these sensory representations and memories to calculate and execute the decisions that emerge as purposeful behavior. To understand the computations that underlie behavior, it is important to gain as much information as possible about behavior and neural activity while the animal performs the task under study.

In contrast to the assays of the early 1900s, the binary choice assays used by contemporary researchers do not enable them to obtain information about the behavioral strategy larvae use to pattern their movements in response to photosensory inputs to seek and remain within dark regions. In fact, it is this behavioral strategy that is encoded within neural circuits for phototaxis. Lack of available approaches to quantify this strategy has motivated my graduate work to develop an automated system to quantify the precise movements of *Drosophila* larvae in re-

sponse to defined photosensory inputs, thereby revealing the navigational strategy encoded in the larva's nervous system.

2

The sensory and behavioral basis of *Drosophila* larval phototaxis

2.1 Introduction

Navigating organisms must extract spatial information about their surroundings to orient and move toward preferred environments. The tropism theory, championed by Jacques Loeb in the early 20th century, has been canonically evoked to explain animal orientation; it states that bilateral body plans allow animals to extract spatial information through the sensation of external forces acting asymmetrically on symmetric body halves [46, 47]. Loeb argued that the navigation of fly larvae away from incident light rays represented a direct demonstration of the tropism theory. Some of Loeb's contemporaries disagreed with his mechanistic explanation [49, 52], arguing that temporal comparisons performed by moving animals, also known as klino-taxis, could encode spatial information. For phototaxis, this debate has remained unsettled due to a lack of available tools. We sought to resolve the sensorimotor structure of larval photo-

taxis using the fruit fly, *Drosophila melanogaster*. Beyond settling a long-standing controversy in the physiology of animal behavior, establishing the sensorimotor structure of phototaxis represents the starting point for circuit level dissection of behavioral circuits in the Drosophila larva.

Drosophila larvae are negatively phototactic throughout most of their development [10, 22, 26, 27, 50, 57–59]. It has long been known that larvae sense light through simple bilaterally symmetric eyes, termed Bolwig's Organs [8, 32], each consisting of 12 photoreceptors located in the dorsal region of the cephalopharyngeal skeleton. Eight photoreceptors express the green-tuned Rhodopsin-6; four express the blue-tuned Rhodopsin-5 [40, 62, 63]. Recently, larvae were also shown to be capable of Bolwig's Organ-independent photosensation at high light intensities via the non-Rhodopsin expressing class IV multidendritic neurons [67]. How these photosensitive structures extract and use information about ambient light conditions to perform navigation has not yet been systematically examined.

2.2 Results

2.2.1 Checker lightscape navigation

To identify the relevant properties of an orienting light stimulus, its corresponding sensory structure (Bolwig vs. non-Bolwig vision), and the navigational algorithms for light avoidance, we developed a novel phototaxis assay capable of delivering arbitrary spatiotemporal light landscapes ("lightscapes") to groups of larvae while recording their detailed responsive movements (Figure 2.1A). Larval navigation involves two stereotyped motor patterns: runs, periods of relatively straight forward movement with high velocity, and turns, reorientation events where the larva sweeps its head to one side (head-sweep) (Figure 2.1B) [19, 20, 43, 48]. Turns are composed of at least one head-sweep. A larva can accept a head-sweep by initiating a new run in the direction of its head, or reject the head-sweep by swinging its head back past the midline to initiate another head-sweep (Figure 2.1B). Here, we sought to determine precisely how photosensory input is converted by the larva's photosensory organs and sensorimotor circuits to the motor patterns that drive navigation.

First, we determined the larva's light-intensity-dependent navigational strat-

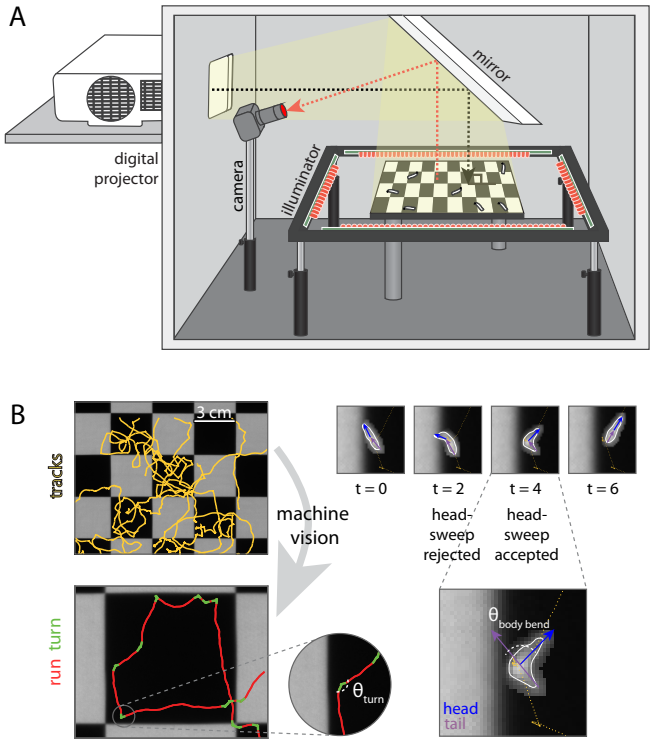

Figure 2.1: Phototaxis apparatus and automated machine vision larval postural analysis. (A) Schematic of phototaxis assay generating a checkerboard lightscape. A digital projector generates arbitrary spatiotemporal light stimuli. Larvae are placed on a 25 x 25 cm dish coated in agar and their resulting behavior is visualized by infrared LEDs and recorded with a camera. (B) Machine vision software segments larval tracks into runs and turns. Turns are composed of accepted and/or rejected head-sweeps.

egy by examining run and turn statistics across populations of wild-type (Canton-S) larvae on a high-contrast checkerboard lightscape [26, 44] (Videos 1 and 2) at light intensities where Bolwig's Organ is required for navigation[1]. We found that larvae initiate turns with greater frequency when crossing from dark to light squares (0°) than when crossing from light to dark (180°) or within the interior of a checker (Figure 2.2A). On the boundary between checkers, the probability of initiating a turn was a smoothly varying function of heading relative to the boundaries between checkerboard squares (Figure 2.2B). Thus, larvae increase their dwell time within dark squares by preferentially turning when pointed in the unfavorable direction at each checkerboard boundary.

In addition to modulating the frequency of turning, larvae biased the size of turns as a function of heading relative to the boundary: the more directly the larva was headed towards a light checker, the larger the subsequent turn (Figure 2.2C). To determine if larvae also modulate turn direction to preferentially orient themselves toward the dark square during each boundary encounter, we examined heading changes achieved during turns on the boundary initiated from diagonal headings. Although larvae make turns of similar size towards light and dark checkers, they executed far more turns toward dark checkers than light checkers (Figure 2.2D), resulting in a net average change towards the dark (Figure 2.2E).

To examine if larvae directly sense spatial light gradients, perhaps by comparing the difference in light intensity between their Bolwig's Organs, we analyzed the statistics of the first head-sweep within diagonally pointed boundary-evoked turns. We found that the direction of the first head-sweep was unbiased (Figure 2.2F), suggesting larvae are indifferent to the local light intensity gradient before initiation of a head-sweep. However, larvae were more likely to accept head-sweeps toward the dark squares (Figure 2.2F). These results suggest that the larvae use head-sweeps as probes to explore their local luminosity environment. As the larva moves its head in a spatially varying light environment, it generates temporal changes in intensity at its photoreceptors, which it uses to determine whether to move in a given direction.

[1] *CS*: 25% +/- 5% time spent in light checker, n=11 (91 larvae), $Rh5^2$; $Rh6^1$: 50% +/- 5% time spent in light checker, n=9 (82 larvae)

Figure 2.2 ***(following page)*****:** Larvae bias turn frequency, size and direction to remain in the dark. Abbreviations: h.s., headsweep, L, left, R, right. n=number experiments (number larvae). For definitions of light intensities see supplementary materials. (A) Schematic of heading angles relative to boundary. Turning rate vs. distance of head from the boundary for -180° and 0° headings, dashed lines indicate boundary region. (B-F) describe turns initiated when the head was in the boundary. (B) Turning rate vs. heading relative to boundary. (C) Turn size (r.m.s.°) vs. heading relative to boundary. (D) Center, schematic of heading angles diagonal to checker boundary. Left and right, polar histograms of heading changes achieved by turns for a fixed initial run heading before turn. Initial heading indicated by arrow. (E) Mean heading change achieved by turns vs. initial heading relative to the boundary. (F) Probability of first head-sweep direction and acceptance to left and right. Numbers indicate total head-sweeps. **, rejection of null hypothesis that probabilities are the same at $p < 0.0001$, binomial statistics.

Figure 2.2: (continued)

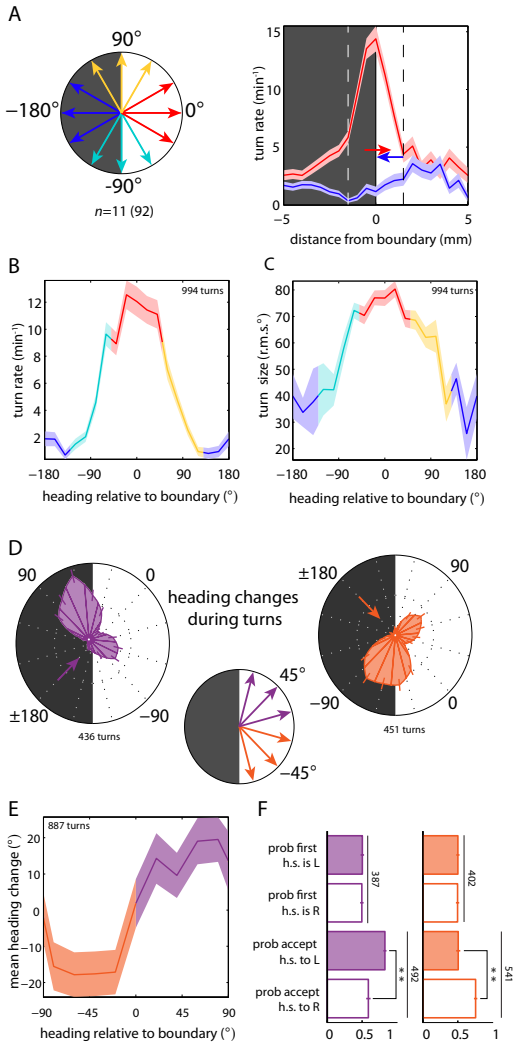

2.2.2 Square-wave temporal lightscape

If the larva utilizes temporal comparisons of light intensity during runs and head-sweeps to identify spatial gradients in local luminosity, then changing light intensity in time but not space (temporal lightscape) should recapitulate two components of navigational strategy: modulation of turn frequency (Figure 2.2A, B) and turn size (Figure 2.2C). We presented larvae with a temporal analog of the checkerboard, a temporal square-wave light stimulus [10, 59] matched in intensity ("low" intensity, dark phase: $< 0.08\frac{W}{m^2}$, light phase: $7 - 13\frac{W}{m^2}$, Figure 2.11) (Figure 2.3A, B, Videos 3, 4). Control *wCS* animals responded to the abrupt increase in light intensity by increasing the frequency and size of their turns, akin to their behavior at the checker boundary. Animals lacking Rhodopsin in both Bolwig's Organ photoreceptor subtypes ($Rh5^2$; $Rh6^1$) did not modulate their turning rate or size (Figure 2.3A,B), demonstrating that Bolwig's Organ Rhodopsin-mediated photoreception is required for behavioral photosensation at the tested light intensity. Using $Rh5^2$ and $Rh6^1$ single mutants, we examined the distinct contribution of Bolwig's Organ photoreceptor subtypes and observed that Rh5 photoreceptors are responsible for behavioral photosensation at low light intensities (Figure 2.3A), in agreement with previously published studies that showed that Rh6 is not required for negative phototaxis [40].

Further analysis of larval behavior in the temporal square-wave lightscape revealed a novel photosensory behavior: pausing (cessation of forward movement without initiation of head sweeps, Figure 2.3C, D, Video 4, compare with 3) in response to an abrupt decrease in light intensity. Dark-induced pausing behavior is mediated by the Rh5 subset of Bolwig's Organ neurons (Figure 2.3C, D). We speculate that dark-induced pausing might be an evasive predatory response; a looming predator might cast a shadow over a larva, which would then cease movement to avoid being detected.

Using the temporal lightscape, we next extended our investigations of phototactic strategy to high light intensity regimes to test the contribution of non-Bolwig's Organ mediated photoreception (photoresponses in Bolwig's Organ ablated larvae have been demonstrated at $88\frac{W}{m^2}$ white light and $39\frac{W}{m^2}$ blue light [67]).

Figure 2.3 ***(following page)*****:** Larvae use temporal comparisons of light intensity to inform phototaxis. Shaded background represents light stimulus. Shaded areas around curves represent +/- s.e.m. n=number experiments (number larvae). For definitions of light intensities see supplementary materials. "Low" intensity: *wCS*: n=4 (98), $Rh5^2$: n=4 (106), $Rh6^1$: n=2 (41), $Rh5^2;Rh6^1$: n=4 (110). "High" intensity: *wCS*: n=4 (107), $GMR-hid$: n=4 (62), $Rh5^2;Rh6^1$: n=5 (119). (A) Turn rate vs. time since light on. (B) Turn size (r.m.s.$^\circ$) vs. time since light on. *wCS*: 2890 turns, $Rh5^2$: 2569 turns, $Rh6^1$: 927 turns, $Rh5^2;Rh6^1$: 3258 turns. (C) Pausing rate vs. time since light off. (D) Average speed and body bend angle (r.m.s.$^\circ$) vs. time since light off. *wCS*: 1299 pauses, $Rh5^2$: 444 pauses, $Rh6^1$: 217 pauses, $Rh5^2;Rh6^1$: 811 pauses. (E) Turn rate vs. time since light on. (F) Turn size (r.m.s.$^\circ$) vs. time since light on. (G) Normalized turning rate vs. time since light on. (H) Average speed vs. time since light on. *wCS*: 3100 turns, $GMR-hid$: 1125 turns, $Rh5^2;Rh61$: 3622 turns.

Figure 2.3: (continued)

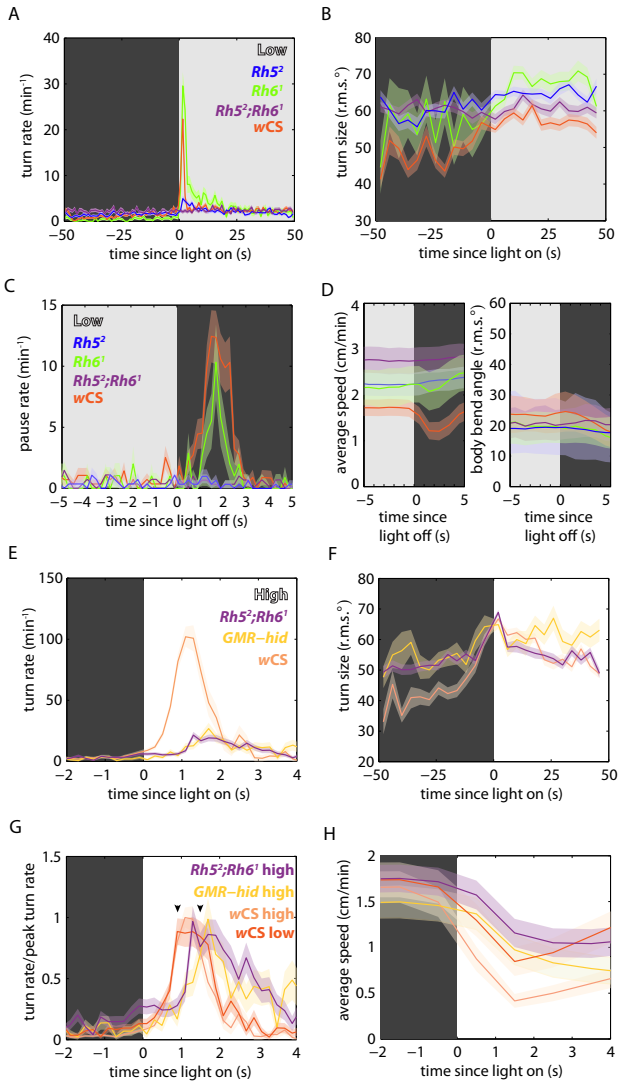

At "high" light intensities (dark phase: $< 0.02 \frac{W}{m^2}$, light phase: $40 - 100 \frac{W}{m^2}$, Figure 2.11) we found that larvae lacking both Rhodopsins ($Rh5^2$; $Rh6^1$) or with their Bolwig's Organs genetically ablated (GMR-hid) respond to light onset by increasing their turning rate and turn size. However, *wCS* control larvae with functioning Bolwig's Organs display a 10-fold higher turning rate in response to light onset as compared to larvae without functioning Bolwig's Organs (Figure 2.3E) and four-fold greater than the "low" light intensity (Figure 2.3A), suggesting that light-evoked turning is primarily mediated by Bolwig's Organ, even at high light intensities. A functioning Bolwig's Organ also contributes to the modulation of turn size at high intensities (Figure 2.3F). An examination of the kinetics of turning onset revealed that animals lacking functional Bolwig's Organ display an approximate 1s delay to peak turning rate (Figure 2.3G, H), relative to animals with functional Bolwig's Organs at both high and low intensities. Thus, Bolwig's Organ mediates rapid photosensory response across the full range of ecologically relevant light intensities.

2.2.3 Linear spatial gradient lightscape

To further probe the larva's ability to sense environmental changes in light intensity, we quantified the navigation of *CS* larvae in response to a defined linear spatial gradient lightscape (Figure 2.4A, B). To concisely quantify larval navigation, we computed a navigational index by dividing the mean velocity of all larvae in the x direction, $\langle vx \rangle$, by the mean crawling speed $\langle s \rangle$ [19]. The navigational index is 1 if larvae are uniformly crawling from dark to light. The index is -1 if larvae are uniformly crawling from light to dark. If the movement is unbiased, the index is zero.

As a control, we also calculated the y-index ($\langle vy \rangle$, navigation perpendicular to the direction of light), which should be zero in all cases due to symmetry. Surprisingly, we found that larvae were unable to navigate on the linear spatial gradient lightscape (Figure 2.4C), the probability of orientation was indistinguishable for all headings (Figure 2.4D). An examination of larval turns from orthogonal headings also showed no evidence of navigation: larvae were equally likely to accept head sweeps to higher and lower intensity directions (Figure 2.4F) resulting in

equal turn frequency to the both directions (Figure 2.4E).

2.2.4 Triangle-wave temporal lightscape

Analysis of larval behavior on checker and square temporal lightscapes revealed that larvae use temporal comparisons of light intensity to extract spatial environmental information that is used for navigation. Why then were larvae unable to navigate on a linear spatial gradient? We speculated that the temporal derivative of light intensity was below the threshold of detection for the larva, such that it adapted over the course of navigation. To test this, we used the temporal analog of a linear spatial gradient, a triangle-wave temporal lightscape. Triangular waveforms with different rates of linearly increasing and decreasing light intensities mimic the temporal stimulus experienced by a larva crawling in a straight line up or down a linear spatial gradient.

During periods of increasing light intensity, larvae reoriented more frequently and made larger turns (Figure 2.5A-C) than periods of decreasing intensity, which is consistent with what we observed on the checker and temporal square-wave lightscapes. The magnitude of the increase in turn rate and size decreases as the linear temporal rate of changes decreases, until the effect is mostly lost at a period of 800 s (Figure 2.5D). The temporal change in light intensity experienced by a larva crawling directly up or down the linear spatial gradient lightscape (Figure 2.4) is approximately half the rate experienced by a larva in the 800 s period triangle-wave lightscape, thus explaining why larvae were unable to navigate the linear gradient lightscape.

2.2.5 Directional lightscape navigation

Early 20th-century blowfly larval phototaxis experiments were conducted using sunlight as a stimulus, with its rays inclined relative to the experimental plane [47, 49, 52] and found that the direction of the stimulus was more important than its intensity - larvae would travel toward areas of higher intensity as long as they were headed away from the source of light. We asked whether Drosophila larvae might also avoid a light source based solely on directional cues. We projected light rays at 45° relative to the plate (Figure 2.6A left, Video 5) and discovered

Figure 2.4 *(following page)*: Larvae do not phototax on a shallow linear spatial gradient. Shaded areas around curves represent $+/-$ s.e.m. n=number experiments (number larvae). (A) Irradiance map of linear gradient lightscape. (B) Irradiance vs. plate distance; blue, average intensity vs. x. red, average intensity vs. y. (C) *CS* larvae navigational index, $\frac{\langle v \rangle}{\langle s \rangle}$, computed for x and y direction on linear gradient lightscape. (D) Left, schematic of linear gradient lightscape. Light incident to plate at 90°. Right, probability of orientation v. heading in runs for linear gradient lightscape. (E) Polar histograms of heading changes achieved by turns, for a fixed initial run heading before turn. Initial heading indicated by arrow. (F) Probability of first head-sweep direction and head-sweep acceptance to left and right sorted by initial heading for linear gradient lightscape.

Figure 2.4: (continued)

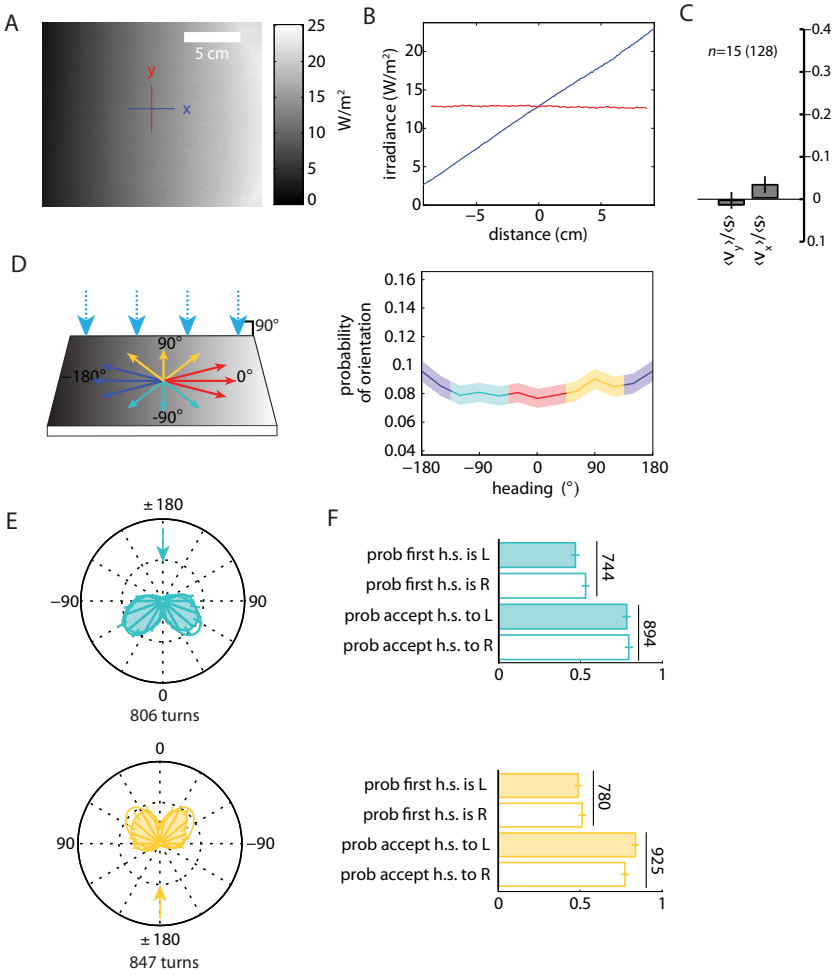

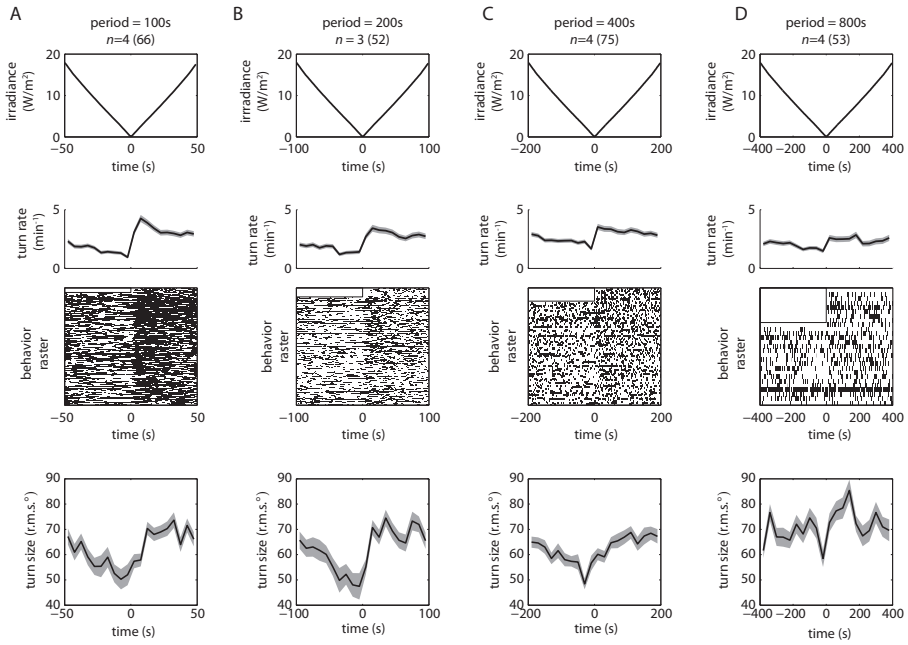

Figure 2.5: Temporal analogs of linear gradient lightscapes (triangle-wave lightscapes). Shaded areas around curves represent +/- s.e.m. n=number experiments (number larvae). (A-D) Statistics of turning decisions for linear temporal gradients delivered as repeating cycles of periods equal to (A) 100 s, (B), 200 s, (C) 400 s, (D) 800 s. From top, one cycle of linear stimulus. Turning rate vs. time. Raster plots represent periods in which an individual larva was turning. Each row represents one larva tracked continuously throughout the cycle. Half period of first cycle discarded for acclimation. Bottom, mean turn size vs. time in cycle.

that wild-type larvae robustly navigated away from the light source (Figure 2.6A, right). Navigation on directional lightscapes could not be attributed to the small spatial luminosity gradient generated by the directional light cue, as larvae failed to navigate on a linear gradient lightscape 25-times as steep (Figure 2.4). To facilitate comparisons between different genotypes and light intensities, we computed a navigational index for all tested strains (Figure 2.6B). We find that wild-type *CS* larvae are capable of direction-based avoidance across a 2,500-fold change in light intensity ($0.04\frac{W}{m^2}$ to $100\frac{W}{m^2}$, the ecologically relevant range [1, 2, 65]) (Figure 2.6B). Bolwig's Organ is strictly required for this behavior at both low and high intensities, as $GMR - hid$ and $Rh5^2$; $Rh6^1$ larvae are unable to navigate away from incident light rays at intensities that are sufficient to induce non-Bolwig's Organ mediated light-evoked turning in the temporal lightscape (Figure 2.6B, Figure 2.3C, D). Since directional light avoidance requires Bolwig's Organ irrespective of light intensity, we determined which subset of photoreceptors mediates directional avoidance by examining the behavior of single Rhodopsin mutants in a low intensity directional assay. As with intensity-based phototaxis, Rh5 neurons, but not Rh6, are required for direction-based phototaxis (Figure 2.6B).

To determine the cellular mechanism for direction-based phototaxis, we examined the morphology and surrounding cephalopharyngeal skeleton of Bolwig's Organ by fluorescence and light microscopy. Bolwig's Organ photoreceptors are located in a thin pocket formed by the the condyle spine and dorsal bridge of the cephalopharyngeal skeleton. Bolwig's Organ sends a single nerve, Bolwig's nerve, posteriorly around the medial region of the pharyngeal skeleton. Confocal microscopy revealed that Bolwig's Organ is shaped like a thin cone, oriented primarily along the dorso-ventral axis, appearing as a small slit when viewed from the top (Figure 2.6C, Video 6). We hypothesized that the opaque cephalopharyngeal skeleton restricts the accessibility of incident light onto Bolwig's Organ, effectively forming a pigment cup eye [3], similarly to what has been proposed in *Calliphora* larvae [32]. When an animal is crawling with a 180° heading or a 0° heading it experiences a relative minimum or maximum of apparent luminosity, respectively (Figure 2.6D). As the animal rotates its head during a head-sweep, it will experience a temporal change in relative luminosity throughout the head-sweep, con-

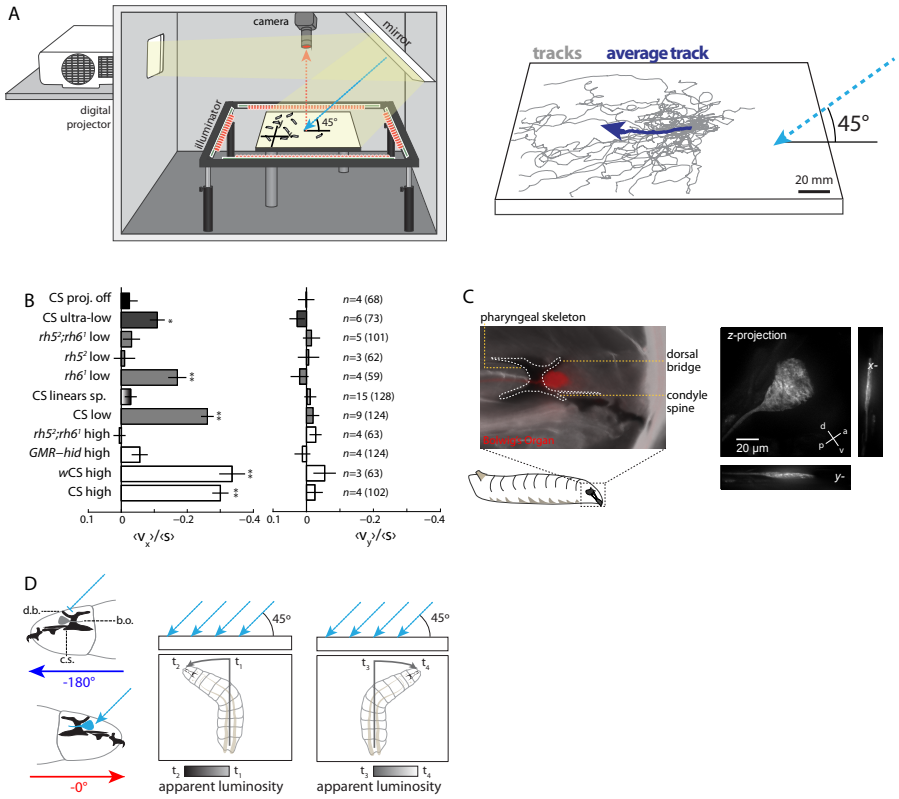

Figure 2.6: Directional lightscape navigation requires the $Rh5$ photoreceptors of the Bolwig's Organ. n=number experiments (number larvae). (A) Left, schematic of directional lightscape apparatus. Light rays are incident to larvae at 45°. Right, tracks (grey) of 30 larvae resulting from navigation on the directional lightscape. Average track plotted in blue. (B) Navigational index, $\frac{\langle v \rangle}{\langle s \rangle}$, computed for x and y direction. *, ** rejection of null hypothesis that data set has same mean as projector-off data set at $p < 0.01$, $p < 0.0001$, respectively, Welch 2-tailed t-test. For light intensities see supplementary materials. (C) Bolwig's Organ sits in pigment cup formed by cephalopharyngeal skeleton. Left, fluorescence microscopy of $GMR - RFP$ merged with bright-field. White dotted line indicates cephalopharyngeal skeleton. Right, maximum intensity projections from 3D confocal microscopy of Bolwig's Organ in $longGMR > CD8 :: GFP$ larva. (D) Schematic of differential view angle of Bolwig's Organ conferred by cephalopharyngeal skeleton.

verting the spatially uniform stimulus into a temporally varying intensity signal that is dependent on head rotation (Figure 2.6D). For instance, a larva oriented at 90° would experience an apparent decrease in light intensity over time as it sweeps its head left and an apparent increase in light intensity over time as it sweeps its head right (Figure 2.6D).

If information acquisition during direction-based phototaxis is achieved through temporal comparison of apparent luminosities during head-sweeps, we would predict that the bulk of navigational strategy would be contained within turning decisions. We quantified the navigational movements of wild-type animals on directional lightscapes to test this hypothesis. On a directional lightscape, a larva is more likely to be oriented away from the light source (-180° heading) (Figure 2.7A), but we found that this orientation bias is not achieved by modulating turn rate as a function of heading (Figure 2.7B, D) or by steering within runs (Figure 2.7C, G). An examination of heading changes resulting from turns pinpointed the origin of the orientation bias: larvae oriented orthogonally to light rays on the directional lightscape are more likely to turn toward the preferred heading, left for +90°, right for -90° (Figure 2.7E, H). Additionally, we found that larvae make larger turns when previously pointed towards rather than away from the incident light rays (Figure 2.7F). The first head-sweep direction is unbiased for all initial headings, but larvae are more likely to accept head-sweeps towards the preferred direction from orthogonal headings (Figure 2.7I). Thus, larvae use head-sweeps to probe the direction of incident light rays, identifying the preferred direction of movement based on a temporal drop in apparent luminosity.

If larvae directly sensed the direction of light by spatial comparisons between their Bolwig's Organs, as predicted by Loeb's tropism theory, we would expect them to steer within runs and/or preferentially initiate head sweeps away from incident light rays; yet, they do not display these biases (Figure 2.7C, G, I). Instead, larvae appear to rely on temporal comparisons during head-sweeps to analyze the direction of light rays. To further test the tropism model, we used laser surgery to unilaterally ablate Bolwig's Organ in larvae whose *Rhodopsin* $-$ 5 expressing photoreceptors were visualized with *GFP* (Figure 2.8A). If larvae rely on comparisons between their eyes to discern the direction of light, then unilaterally ablated lar-

Figure 2.7 ***(following page)*****:** Directional lightscape navigational strategy. n=number experiments (number larvae). Shaded areas represent $+/-$ s.e.m. Top, schematic of headings on directional lightscape. Black and dashed lines are the prediction and 95% confidence interval of a model with biases in turn magnitude and head swing acceptance [19]. (A) Probability of heading during runs. (B) Turn rate vs. heading in run. (C) Mean heading change achieved in run vs. initial run heading. (D) Distribution of run lengths for larval headings into incident light rays (red, 0°, unpreferred heading) and away (blue, 180°, preferred heading). (E) Mean heading change during turn vs. previous run heading. (F) Heading change size (r.m.s °) vs. initial heading (°). (G) Polar histograms of heading changes achieved by runs for a fixed initial heading, indicated by arrow. Numbers inset on polar grid represent number of runs used in graph. (H) Polar histograms of heading changes achieved by turns for a fixed inital heading before turn. Initial heading indicated by arrow. Numbers inset on polar grid represent number of turns used in graph. (I) Probability of first head-sweep direction and acceptance sorted by initial heading. * rejection of hypothesis that mean is 0.5 at $p < 0.01$, binomial statistics. ** rejection of null hypothesis that distributions have same mean at $p < 0.0001$, binomial statistics.

Figure 2.7: (continued)

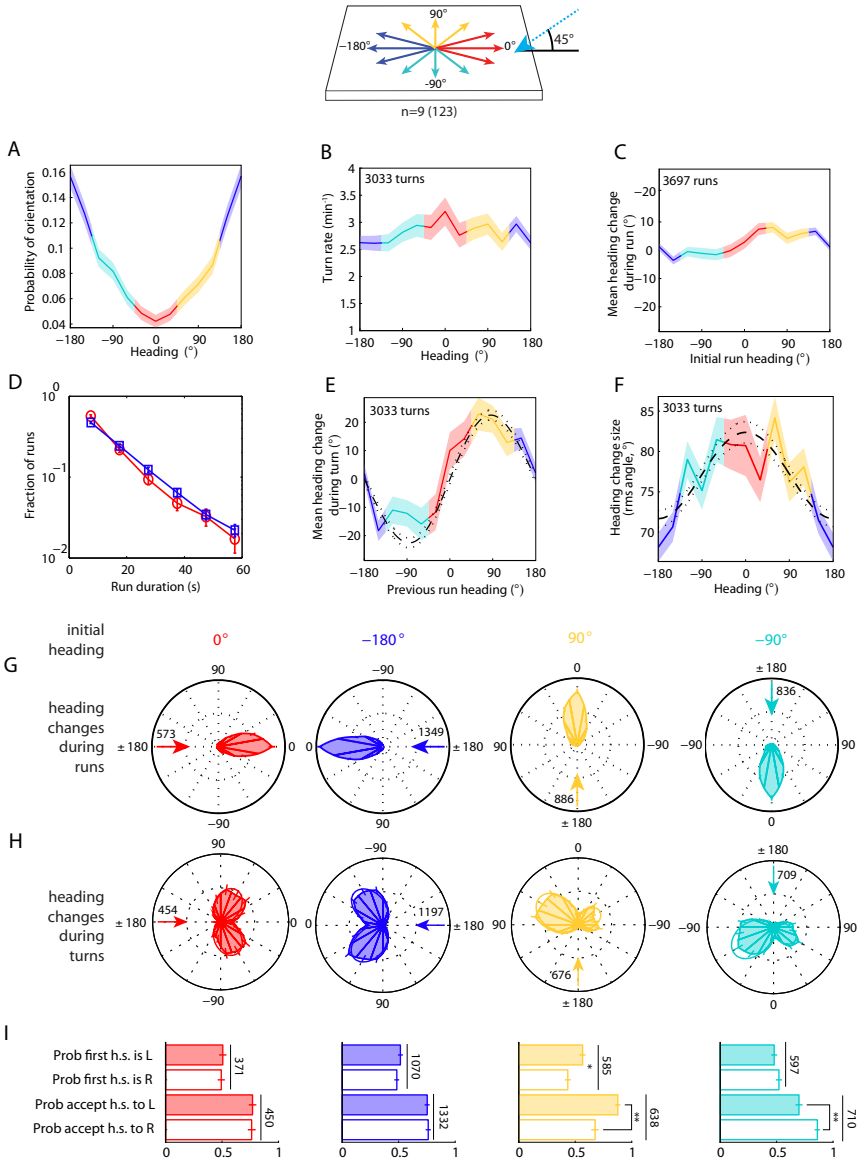

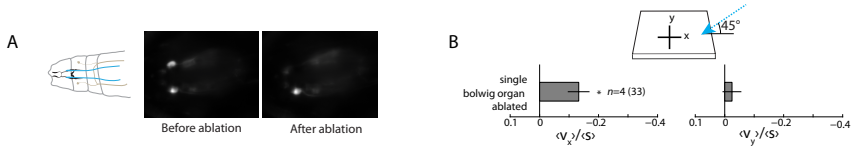

Figure 2.8: (A) Schematic and fluorescence microscopy of $Rh5 - GFP$ larva before and after laser ablation of one eye. (B) Navigational index($\frac{\langle v \rangle}{\langle s \rangle}$) computed for single Bolwig's Organ ablated larvae. *, rejection of null hypothesis that $Rh5^2$ and single Bolwig's Organ ablated animals have the same mean at $p < 0.01$, Welch 2 tailed t-test.]

vae should not be capable of directional lightscape navigation. However, we found that larvae with one eye successfully navigated away from the directional light source, showing that one Bolwig's Organ suffices to extract the direction of light rays (Figure 2.8B).

2.3 Discussion

Figure 2.9 summarizes the sensorimotor structure of larval phototaxis. Larvae modulate their frequency of turning based on temporal changes in light intensity. In continuously varying gradients [19, 21, 48], this results in longer runs in favorable directions (Figure 2.9A). Larvae also bias their turn size, executing larger heading changes following runs toward unpreferred directions and smaller heading changes following runs in the preferred direction (Figure 2.9B). Larvae use temporal head-sweeps as probes to explore local luminosity gradients and identify the preferred direction for successive runs. Initial head sweep direction is unbiased, but larvae are more likely to accept head-sweeps toward the preferred direction (Figure 2.9C).

These strategies all rely on decoding temporal variation in the amount of light incident on the Bolwig's Organs. Bolwig's Organ and the surrounding cephalopharyngeal sclerites encode directional light information in temporal variations of light intensity that are correlated with the orientation of the head with respect to light rays (Figure 2.6D). On directional lightscapes (Figure 2.6), larval head-

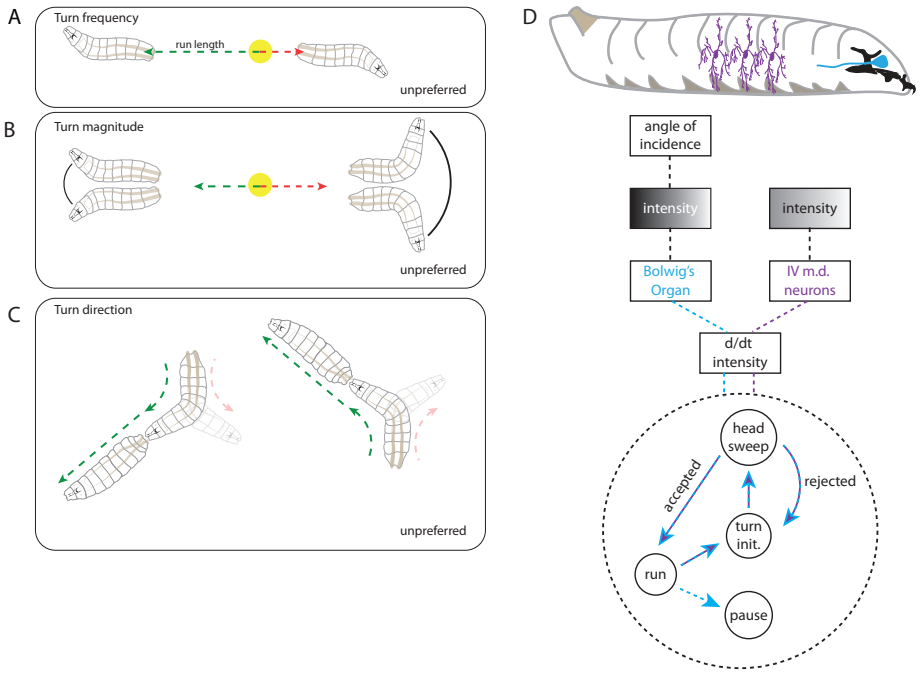

Figure 2.9: Models for phototaxis navigational strategy and photosensory processing. (A) Larvae use temporal comparisons of light intensity during runs to modulate turn frequency. Gradient represents light intensity. (B) Larvae make larger turns from the unpreferred direction, smaller turns from the preferred direction. (C) Larvae use head-sweeps as probes to explore their local environment and to identify the preferred direction for successive runs. Turn direction bias is generated by asymmetrical acceptance of head-sweeps toward the preferred direction. (D) Model of larval photosensory processing as described in text.

sweeps change the amount of light incident on the Bolwig's Organ, whereas the apparent intensity remains constant during straight, forward runs; hence, turn magnitude and direction are biased (Figure 2.9B, C) but not turn frequency.

The larva contains two photosensory structures, Bolwig's Organ (Figure 2.9D, blue) and the class IV multidendritic neurons (Figure 2.9D, purple). Bolwig's Organ is the main photosensory structure, contributing to phototaxis across the full range of ecologically relevant light intensities, and is specifically required for direction-based phototaxis. Multidendritic neurons are capable of sensing light at very high intensities, and contribute to light-evoked turns (Figure 2.3E, compare *GMR−hid*, $Rh5^2$; $Rh6^1$ to *wCS*). Photosensory information obtained from Bolwig's Organ is translated into behavior more rapidly than photosensory information obtained from multidendritic neurons (Figure 2.3G). Behavioral state transitions driven by either photosensory structure are based on temporal comparisons, but the location of Bolwig's Organ in the "pigment cup" formed by the cephalopharyngeal sclerites uniquely allows decoding of incident light direction. Taken together, our results establish the sensorimotor structure of larva phototaxis across the full range of ecologically relevant light intensities. Moreover, our results appear to settle a long-standing controversy in Drosophila larval phototaxis, explaining the apparent tropism in direction-based phototaxis as a joint product of the anatomy of the light-sensing organ and temporal comparisons used during intensity-based phototaxis.

2.4 Materials and Methods

2.4.1 Strains

The following fly strains were used: *CS*, *wCS*, w;GMR-hid (created from Bloomington stock 5771), *w*; $Rh5^2$; $Rh6^1$ (gift from Claude Desplan), *w*; $Rh5^2$, *w*; *Rh*61, *w*; *Rh*5−*GFP* (created from Bloomington stock 8600), *w*; *GMR−myr−RFP* (Bloomington stock 7121), *w*; *longGMR−gal*4 (Bloomington stock 8604), *w*; *UAS−CD*8 :: *GFP* (created from Bloomington stock 5137).

2.4.2 Phototaxis apparatus

Larval behavior was recorded with a USB CCD camera (Mightex BCE-BO5O-U) fitted with a 620 nm bandpass filter (Thorlabs FB620-10) at 5 frames s-1 using dark field illumination with red LEDs (624 nm, outside range of larval vision). For the checkerboard lightscape (Figure 2.1 and Figure 2.2) and linear intensity gradient (Figure 2.4B) only, the dark field illumination was provided by infrared LEDs (875 nm) and behavior was imaged through a longpass filter.

Light stimuli were delivered by either an LCD projector (Epson Powerlite W6, "low" intensities) or DLP projector (ViewSonic PRO8500 XGA DLP, "high" intensities), and were either projected directly onto the agar or reflected off a front surface 10" x 10" mirror (Edmund Optics NT46-653) . The Epson projector red channel was disabled using software to avoid interference with the red LED illuminator, and the projector light was additionally filtered using a 335-610 nm bandpass filter (Thorlabs FGB37S). The filter wheel from the Viewsonic projector was removed to maximize light output. Instead, Viewsonic projector light was filtered through a cyan dichroic (Thorlabs FD1C, Angle of Incidence 0°) to remove red light that would interfere with the red LED illuminators. The behavioral arena was contained within a light-tight custom box (80/20 Inc.).

Video recording and control of the light source were accomplished via custom LabView software. During experiments with temporally varying lightscapes, the software recorded the light state together with the video frame number and elapsed time so that the light intensity and larval behavior could be synchronized in analysis.

2.4.3 Light intensity determination

The irradiance of each light source was measured using a thermopile optical power meter (Thorlabs S310C) and the relative spectral intensity using a CCD based spectrometer (Vernier USB-2000) fiber coupled to a cosine corrector. At the same time, the luminance was also measured using a handheld lux meter (Traceable 3251). Because the spectral distribution of the light sources did not match the spectral distribution of the tungsten lamp with which the lux meter was calibrated, the lux meter did not read true luminance, but the measured value of the light meter was proportional to the irradiance; for each source, this constant was determined by

adjusting the intensity of the source and measuring the irradiance and luminance using the optical power meter and lux meter.

After any adjustments to the apparatus and periodically afterward, the apparatus was calibrated by imaging the projector output on a Lambertian surface (projector screen) using the same camera used to record larva behavior. The camera gray level was proportional to the irradiance, and we measured the constant of proportionality by adjusting the projector intensity while using the lux meter to measure the irradiance and recording the corresponding gray value with the camera.

To calibrate the alignment of the camera to physical space and compensate for any lens distortions, we took a picture of a 1 cm checkerboard placed in the same plane as the agar surface. Due to dispersion, the focal length of the lens was slightly different at the wavelengths in the projected image compared to the dark-field illumination wavelength used to measure behavior. To compensate for the resulting small shift in magnification, we photographed the same checkerboard under both illumination conditions.

For the experiments of Figure 2.2, we used the calibration data to produce an image that when projected produced a checkerboard exactly 3 cm on a side. For all experiments, we imaged the projected light stimulus (checkerboard or constant illumination for directional and temporal experiments) on the Lambertian surface. For directional experiments (Figure 2.6), we also took an image of an array of posts of known height; the length of the posts' shadows allowed us to determine the spatial distribution of the incident light angle. Thus we were able to determine with high accuracy the exact irradiance experienced by a larva based on its position on the camera image.

Precise quantification of lightscape intensities is contained within Figures 2.10 and 2.11. Briefly: for the checker lightscape, the light checker was $12\frac{W}{m^2}$, dark checker was approximately $< 0.08\frac{W}{m^2}$. For the temporal lightscape, "low" intensity square-wave light phase was $7 - 13\frac{W}{m^2}$, dark phase was $< 0.07\frac{W}{m^2}$. "High" intensity square-wave light phase was $40 - 100\frac{W}{m^2}$, dark phase was $< 0.02\frac{W}{m^2}$. For the directional lightscape, "high" intensity was $40 - 100\frac{W}{m^2}$, "low" intensity was $4 - 6\frac{W}{m^2}$, "ultra-low" intensity was $0.05\frac{W}{m^2}$, projector off assay was performed with no projected light, and intensity control was a linear spatial gradient of intensity

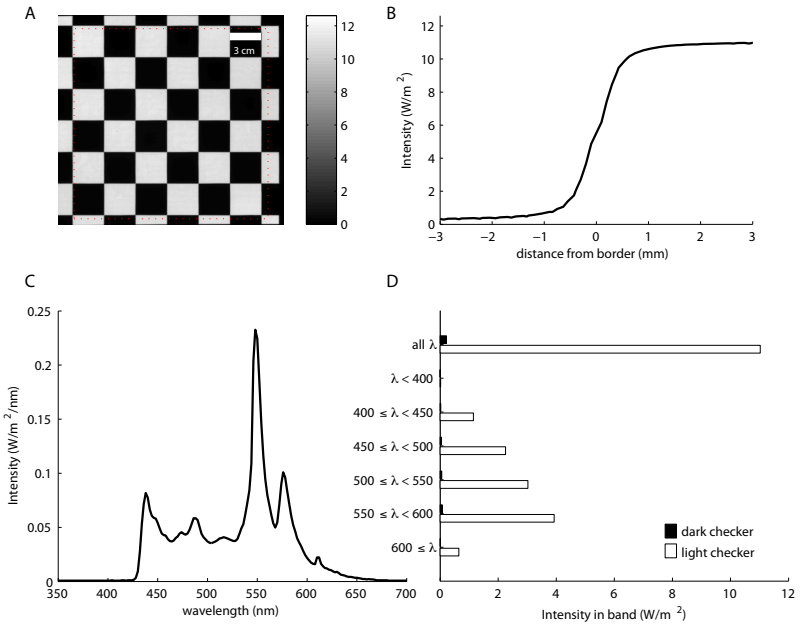

Figure 2.10: Checker lightscape irradiance (refers to Figure 2.2). (A) Irradiance map of checker lightscape. Red dashed line shows region where behavior was analyzed. (B) Irradiance vs. distance from checker border (mm). (C) Spectral irradiance vs. wavelength of projector light. (D) Total irradiance in indicated wavelength band for light and dark checkers.

from $2 - 25 \frac{W}{m^2}$ projected perpendicular to the surface.

2.4.4 Behavior experiments

All experiments were performed on second-instar larvae as verified by spiracle morphology. Adult flies were allowed to lay eggs on grape-juice supplemented agar plates with yeast for 3 hours. After egg laying, plates were kept in a 22°C incubator on a 12 hr light-dark cycle. All experiments were performed during the 12 hour day.

Larvae were sorted by spiracle morphology under a dissecting scope, then kept in the dark on food for at least an hour before phototaxis experiments. After dark treatment, larvae were washed under red illumination at least three times in phosphate-buffered saline and placed on a 10 cm petri dish containing 1% Bacto agar in the dark for at least 5 minutes to allow for adaptation to the medium and removal of any residual food.

Larvae were then transferred from the 10 cm petri dish to the experimental arena using a paint brush. Larvae were distributed evenly over the center region of a 4 mm thick (24 x 24 cm) square 1% Bacto agar gel poured on top of a black, square-anodized aluminum plate. For all experiments, the stimulus light intensity was kept at its lowest level until the beginning of recording. For Figure 2.3, we discarded the first period of stimulus during analysis, during which the larvae were acclimatizing to the apparatus after being handled with a paint brush. For Figures 2.6 and 2.7, we discarded the first two minutes of recorded behavior (acclimatization period) and analyzed the subsequent 15 minutes (after this time, successfully navigating larvae began to pass the edge of the observation window, biasing the statistics of the population). For Figures 2.2, 2.6 and 2.7, experiment duration ranged from 25-30 minutes.

Larval posture was analyzed with the MAGAT analyzer, as previously described [19]. Briefly, larval positions and postures were extracted from video records using custom machine vision software. Each larva is tracked throughout the arena while determining the position of the center of mass, the outline of the body, the position of the head, the tail and a midline running down the center of the larva. After extraction of larval features, data was analyzed using software written in

Figure 2.11 ***(following page)*****:** Temporal and directional lightscape irradiance (refers to Figures 2.3, 2.6, and2.7) (A) - (I) Images of lightscapes used for main Figures sorted by experiment and genotype. Colored outline denotes which projector was used for experiment. Green line indicates projector 1, blue line indicates projector 2. (J) Total irradiance at center of image for lightscapes depicted in (A)-(I). (K) Spectral irradiance vs. wavelength for projectors.

Figure 2.11: (continued)

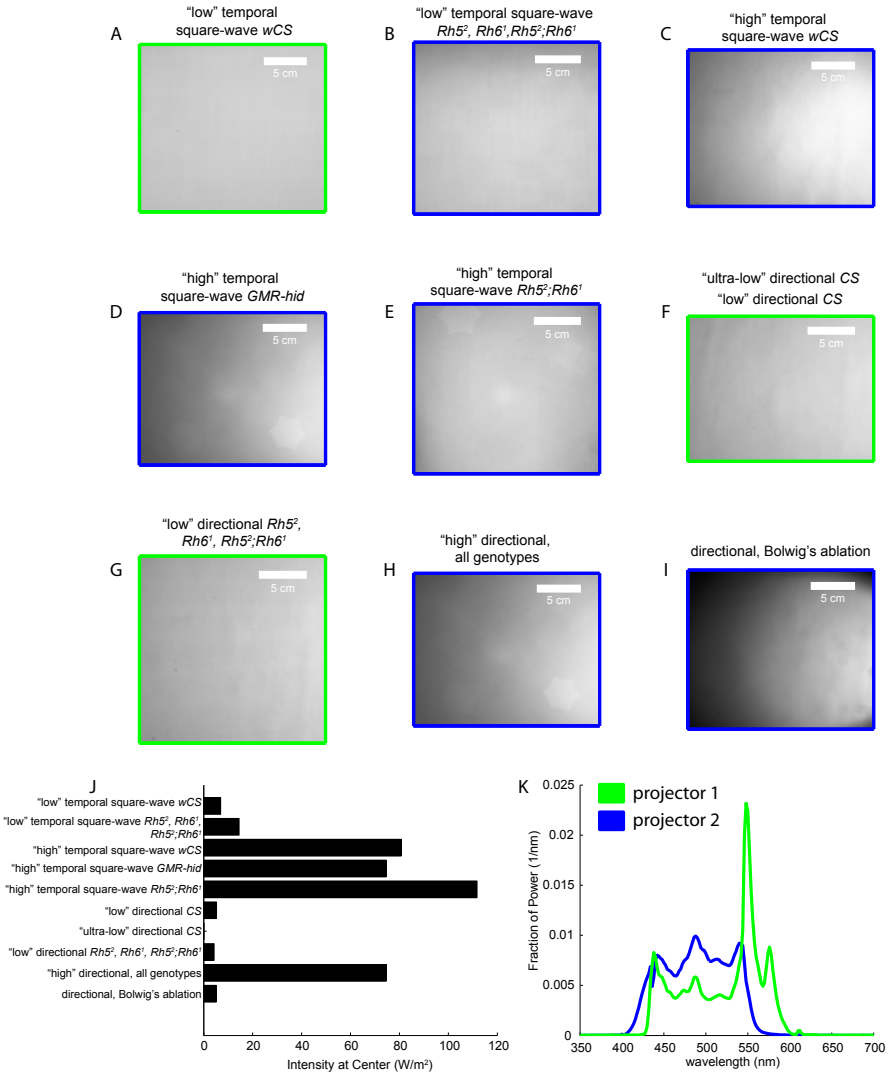

MATLAB (MathWorks). Runs were periods of forward movement with the head aligned with the body, turns were periods of slow or no forward movement accompanied by body bends (head sweeps), and pauses were periods of slow or no forward movement where the head remained aligned with the body. To calculate standard error in Figure 2.7, the number of independent measurements was estimated to be the observation time divided by twice the autocorrelation time of the direction of forward movement.

For Figure 2.2, the distance to the boundary was defined to be the distance from the larva's head to the nearest edge and was positive in light squares and negative in dark squares. For Figure 2.2, only turns within 1.5 mm of an edge and at least 1.5 mm from a corner were considered.

2.4.5 Laser Ablation

Rh5 — GFP early second-instar larvae were immobilized by compression in water; a coverslip mounted on a micrometer was lowered on top of a larva in a droplet of water placed on a glass slide until its head was everted and could no longer move. We used a previously described femtosecond laser ablation technique adapted from use on *C.elegans* [11]. Laser light from an amplified Titanium:sapphire laser system, which emits a 2 MHz train of near infrared pulses ($30\frac{nJ}{pulse}$), was directed through the back-aperture of a Zeiss Plan Apochromat 60x 1.4-NA oil-immersion objective. The same objective was used to image the larval eye by epifluorescence microscopy using a CoolSNAP HQ2 CCD camera (Roper Scientific Photometrics). The image plane of the CCD camera was adjusted to the laser focus. Using fluorescent microscopy, the cell bodies and axonal projections of *Rh5 — GFP* neurons in a single Bolwig's Organ were placed at the focal point of laser pulses and ablated.

After eye ablation, larvae were allowed to recover for 24 hours on a grape juice plate supplemented with yeast paste. Each larva was then examined using epifluorescence microscopy to confirm that the ablated Bolwig's Organ did not regenerate. If fluorescence in the Bolwig's Organ was observed, the animal was discarded.

2.4.6 Microscopy

Fluorescent and bright-field microscopy of Bolwig's Organs were imaged in second-instar *w*; *GMR − myr − RFP* larvae. Epiluorescent and bright field images were taken using a Nikon LV100 microscope, a Nikon 40x air objective (NA 0.95), a Prior Lumen200 illuminator, a standard RFP dichroic set and were imaged on a CoolSNAP EZ CCD camera (Roper Scientific Photometrics). Images were acquired using Nikon Elements software.

3D reconstructions of Bolwig's Organs were carried out on *longGMR > CD8 :: GFP* 2nd-instar larvae. Spinning-disk confocal images were acquired with a Nikon LV100 microscope fitted with an Andor Revolution system (including a Yokogawa CSU22 spinning-disk, an iXon2 EMCCD camera and a 488 nm GFP excitation laser) using a Nikon 60x water-immersion objective (NA 1.20). Spinning-disk confocal images were recorded with Andor iQ software. Maximum intensity *x*-, *y*-, and *z*-projections were constructed using custom software in Igor Pro (Wavemetrics).

2.5 Accompanying Videos

2.5.1 Video 1

Video 1: Example of runs and turns taken from a typical experiment on a checkerboard lightscape (experiments depicted in Figure 2.1 and Figure 2.2). Video shows in succession the projected checkerboard pattern (tinted cyan), infrared image of all larvae being observed, then magnified view of a single larva. Track shown is center of mass position of larva over time period shown. Runs are noted with orange arrows parallel to run direction; turns are indicated with green arrows. Checkers are 3 cm on a side. Scale bar in last portion of movie is 5 mm. At 25 frames-per-second (fps) default playback speed, video is 5x real time.

2.5.2 Video 2

Video 2: Video description of heading relative to boundary, turn direction, and accepted and rejected head sweeps on a checkerboard lightscape (experiments depicted in Figure 2.1 and Figure 2.2). Video shows in succession the projected checkerboard pattern (tinted cyan), infrared image of all larvae being observed, then magnified view of a single larva. Track shown is center of mass position of

larva over time period shown. The border region between two checkers is indicated in white; the corner region is indicated in red (Figure 2.2 show the analysis of turns on the border but not on the corner). Each turn on the border is annotated in sequence with previous heading relative to the boundary normal (orange θ), whether each head sweep is accepted or rejected, and the heading change achieved by the turn (green $\Delta\theta$). Checkers are 3 cm on a side. Scale bar in last portion of movie is 5mm. At 15 fps default playback speed, video is 3x real time. Video pauses briefly with each annotation.

2.5.3 Video 3

Video 3: Examples of light-on induced turns. Left side shows section of larval track (white dots) and video of larva. Yellow dots indicate midline of larva, red arrow is line from midpoint to head, and blue line runs from tail to midpoint. Text in upper left corner indicates time since beginning of experiment, light status, current behavioral state (run, turn, head sweep), and metrics (run duration and distance, turn angle, head sweep acceptance) of behavioral state. Cyan background indicates light is on. Scale bar is 1 mm. Right side shows metrics of navigation. All plots: shading indicates behavioral state: blue = run, white = turn or pause, red = rejected head sweep, green = accepted head sweep. Upper plot: center of mass speed; red and green lines indicate thresholds to end and begin a run, respectively. Center plot: dot product between mid-head vector and velocity vector (1 = head is aligned with direction of motion; -1 = larva is backing up); pink line indicates threshold to begin or end a run. Bottom plot: body bend angle; red and green lines indicate thresholds to end and begin a head sweep, respectively. At 15 fps default playback speed, video is 3x real time.

2.5.4 Video 4

Video 4: Examples of light-off induced pauses. Left side shows section of larval track (white dots) and video of larva. Yellow dots indicate midline of larva, red arrow is line from midpoint to head, and blue line runs from tail to midpoint. Text in upper left corner indicates time since beginning of experiment, light status, current behavioral state (run, turn, head sweep), and metrics (run duration and distance, turn angle, head sweep acceptance) of behavioral state. Cyan background

indicates light is on. Scale bar is 1 mm. Right side shows metrics of navigation. All plots: shading indicates behavioral state: blue = run, white = turn or pause, red = rejected head sweep, green = accepted head sweep. Upper plot: center of mass speed; red and green lines indicate thresholds to end and begin a run, respectively. Center plot: dot product between mid-head vector and velocity vector (1 = head is aligned with direction of motion; -1 = larva is backing up); pink line indicates threshold to begin or end a run. Bottom plot: body bend angle; red and green lines indicate thresholds to end and begin a head sweep, respectively. At 15 fps default playback speed, video is 5x real time.

2.5.5 Video 5

Video 5: Video description of directional lightscape experiment and analysis (experiments depicted in Figure 2.6 and Figure 2.7). Video shows in sequence an animation describing light orientation, an image of metal posts casting shadows under directional illumination with directional compass, video of all larvae being observed, then magnified video of a single larva. Track shown is center of mass position of larva over time period shown. Runs are noted with orange arrows parallel to run direction; turns are indicated with green arrows. Turns are annotated in sequence with previous heading (orange θ, 0° is directly into the light), whether each head sweep is accepted or rejected, and the heading change achieved by the turn (green $\Delta\theta$). Scale bar is 5 mm. At 15 fps default playback speed, video is 5x real time. Video pauses briefly with each annotation.

2.5.6 Video 6

Video 6: 3D reconstruction of Bolwig's Organ. A 3D spinning-disk confocal reconstruction of Bolwig's Organ in a 2nd-instar *longGMR* $>$ *CD8* :: *GFP* larva rotating about the *y*-axis defined in Figure 2.6C.

2.6 Acknowledgements

We thank S. Whitmore and K. Hunter for help with experiments; C. Desplan for transgenic flies; E. Soucy and J. Greenwood for engineering advice and assistance; P. Garrity and S. Kunes for critical reading of the manuscript.

2.7 Author contributions

Elizabeth A. Kane and Aravinthan D. T. Samuel conceived of the project. Elizabeth A. Kane, Marc Gershow, and Ashley R. Carter designed the phototaxis experimental apparatus. Elizabeth A. Kane, Marc Gershow and Aravinthan D. T. Samuel designed experiments. Elizabeth A. Kane, Marc Gershow and Mason Klein carried out experiments. Marc Gershow wrote the MAGAT analyzer software that takes videos of larvae and converts them into segmented behavioral tracks [19]. Elizabeth A. Kane, Marc Gershow and Mason Klein analyzed data and assembled figures. Elizabeth A. Kane and Ashley R. Carter designed and carried out preliminary experiments. Elizabeth A. Kane, Marc Gershow and Aravinthan D. T. Samuel wrote the paper. Aravinthan D. T. Samuel, Simon Sprecher, and Benjamin L. de Bivort supervised the project.

2.8 Manuscript information

A previous version of this chapter was prepared for submission as a publication with the following author list and title: Elizabeth A. Kane*, Marc Gershow*, Mason Klein, Ashley R. Carter, Benjamin L. de Bivort, Simon G. Sprecher, Aravinthan D. T. Samuel. The physical and behavioral basis of Drosophila larval phototaxis.*, these authors contributed equally.

3

A screen to identify phototaxis circuit components

3.1 Introduction

Elucidating the underlying navigational strategy *Drosophila* larvae use to find low luminosity regions is a foundational step in establishing the larva as a model system to explore circuit- and gene-level generation of behavior. Not unlike *E.coli* or *C.elegans*, larval locomotion is an alternating sequence of two stereotyped motor patterns: runs (straight forward movement) and turns (an abrupt change in the direction of forward movement). Unlike smaller organisms, however, the larva uses individual turns to make navigational decisions, pausing and sweeping its head from side to side, thereby sampling the local environment before selecting the direction of its next run. In Chapter 2, I outline the three sensorimotor rules that govern phototaxis navigational strategy: (1) turn more frequently when light intensity is increasing, (2) make larger turns when light intensity is increasing, and (3) bias the direction of turns toward darkness after

sampling the environment with temporal comparisons during head-sweeping. These discoveries provide the intellectual framework to dissect specific sensorimotor transformations in a comparatively simple nervous system.

3.2 Strategy for identifying phototaxis circuit neurons

3.2.1 Janelia Farm GAL4 collection

We have embarked on a large behavioral screen in collaboration with Simon Sprecher's lab to identify neurons involved in photosensory processing and decision-making as a subproject of the larger Larval Olympiad at Janelia Farm. We are silencing subsets of larval central brain neurons, utilizing the powerful GAL4/UAS system [9, 33], with inducible or constituent manipulators of neural activity and observing the resulting effects on phototaxis behavior using the phototaxis assays I developed in my graduate work.

I will briefly summarize how the GAL4/UAS system works: a tissue specific promoter of interest is chosen to drive expression of GAL4 (shorthand is promoter-GAL4), a yeast transcription factor that binds to Upstream Activation Sequences (UAS). Upon binding, GAL4 activates transcription of the gene or genes that are under UAS promoter regulation (shorthand is UAS-responder). The real power of the GAL4/UAS system comes from its modularity; one can have a collection of flies that contain distinct promoter sequences specifying unique expression patterns and simply cross them to any UAS-responder line and obtain progeny that contain all of the necessary genetic elements to tissue-specifically express the responder in the cells specified by the GAL4 promoter, thus eliminating the need to make separate transgenic flies for every desired experiment. Colloquially, the GAL4 line is known as the "driver" since it specifies where a protein will be expressed, while the UAS line is known as the "responder" since it responds to the driver line by specifying what will be expressed.

Gerry Rubin's lab at Janelia Farm has made a large collection of GAL4 lines (approximately 7000) that drive expression in distinct but overlapping subsets of central brain neurons in adult flies. A subset of the original collection have been examined for expression patterns in the 3rd-instar larva by the Truman lab and approximately 700 lines were selected for their relatively sparse expression

patterns to constitute a larval central brain GAL4 driver collection.

3.2.2 Design of primary and secondary screens

Tetanus toxin (TeT) is a clostridial neurotoxin composed of two polypeptide chains: a heavy chain which mediates selective binding to neural tissue and its translocation into the cytosol, and a light chain which catalytically inhibits synaptic transmission by cleaving the essential synaptic vesicle release protein synaptobrevin [64]. Expression of only the TeT light chain (TeTxLC) is sufficient to inhibit or abolish synaptic transmission [28, 55].

For the primary screen, the 700 larval GAL4 lines will be crossed to UAS-TeTxLC flies to constitutively abolish synaptic signaling in specific subsets of larval central brain neurons. The behavior of the resulting F1 progeny will be determined in two phototaxis assays outlined in Section 3.2.3. It is expected that constitutive silencing of synaptic function will result in developmental nervous system defects that may cause non-specific decrements in phototaxis behavior. Therefore, as a secondary screen, we will use the inducible temperature-sensitive silencer of synaptic transmission, *shibire*^{ts} (*shi*^{ts}), to inhibit neuron function [38, 41, 42, 53]. The *shibire* gene encodes a dynamin-like protein required for vesicle trafficking and recycling [66]. At the restrictive temperature (30°C) *shi*^{ts} protein no longer functions to cleave endocytic vesicles containing recycled neurotransmitters, resulting in synaptic vesicle depletion. This phenomenon is reversible, as the protein can function normally if the temperature is brought down to the permissive temperature (20°C). Thus, we can observe the effect of removing circuit components inducibly during testing to determine if phototaxis phenotypes resulting from inactivation of candidate circuit neurons are due to confounding developmental defects or a bona fide removal of circuit components.

3.2.3 Behavioral assays to determine defects in phototaxis circuit function

In order to identify circuit components of Bolwig's Organ mediated phototaxis and to ascribe defects to specific components of navigational strategy, we selected two phototaxis behavioral assays based on our work on phototaxis navigational strategy, outlined in Chapter 2: the square-wave temporal lightscape (Section 2.2.2)

and the directional lightscape (Section 2.2.5). Examining the behavior of each line in both assays will allow us to parse circuit component defects into the following categories:

1. *Bolwig's Organ v. non-Bolwig's Organ mediated phototaxis.*

In Chapter 2, Section 2.2.2, we determined that both Bolwig's Organ and the class IV multidendritic neurons can mediate the non-directional components of navigational strategy evoked by temporal changes in light intensity. They were (1) turn more frequently when light intensity is increasing, and (2) make larger turns when light intensity is increasing. Although the relative contribution of Bolwig's Organ mediating photosensory information to turning frequency is much greater than the class IV multidendritic neurons, it would be difficult to parse circuit processing components to a particular sensory structure from this assay alone. In Chapter 2, Section 2.2.5, we determined that only Bolwig's Organ is capable of relaying the directional light-ray information. Therefore, by examining the behavior of the same line on the temporal square-wave and the directional lightscapes we will be able to determine if defects in phototaxis behavior are due to inactivation of processing components for Bolwig's Organ mediated photosensory information (observe class IV multidendritic neuron mediated level of turning on temporal square-wave lightscape, but observe defect in navigation on directional lightscape), processing for class IV multidendritic neuron mediated photosensory information (small reduction in turning on temporal-square wave lightscape consistent with contribution from class IV multidendritic neurons, but no defects observed on directional lightscape), or a defect in both (defect observed on temporal square-wave lightscape and on directional lightscape).

2. *Defects in specific components of navigational strategy*

In Chapter 2, Section 2.2.5, we determined that the larva can sense and navigate away from directional light rays using its Bolwig's Organ. The larva is able to extract directional light information via the coupling of the differential shading of the Bolwig's Organ by the cephalopharyngeal skeleton and the rotation of its head. Thus, as the larva sweeps its head in a uniform intensity directional lightscape, it "sees" temporal changes in light intensity, experiencing the brightest light when its anterior end is pointed directly into the light rays (Figure 2.6C, D). To effectively navigate away from light rays, larvae utilize two components of a biased random walk navigational strategy, (1) make larger turns when the apparent light inten-

sity is increasing during head sweeping and (2) bias the direction of accepted head sweeps toward lower apparent light intensities, which is when the larva's head is pointed in the same direction as the light rays, away from its source. By examining the behavior of screen lines on the temporal square-wave lightscape and the directional lightscape, we can determine if a line has a specific defect in any of the 3 components of navigational strategy (Figure 2.9A, B, C).

3. *Defects in central navigational decision-making*

As part of the Janelia Farm Larval Olympiad, screens for thermotaxis and chemotaxis defects are being conducted on the same 700 larval central brain GAL4 driver collection. The Samuel lab has previously published that navigational strategies underlying thermotaxis [48] and chemotaxis [19] are the same as phototaxis. This raises the possibility that all sensory information may be integrated into a master navigational decision-making circuit. If this were the case, then one would expect to find lines that display defects in navigational strategy components across all tested sensory modalities. We will be able to determine this by comparing the navigation of a particular line across all three behavioral assays.

3.3 Progress

The screen at Janelia Farm is currently underway. As part of Janelia Farm's research agreement, data from the screen cannot be included in any published format prior to an official publication by the Larval Olympiad team.

3.4 Contribution notes

Elizabeth A. Kane, in collaboration with Marc Gershow, designed the phototaxis screen currently underway as part of the Janelia Farm Larval Olympiad. Bruno Afonso and members of Simon Sprecher's lab are running the phototaxis experiments. Elizabeth A. Kane, Marc Gershow and Bruno Afonso assisted with data analysis.

Bibliography

[1] M.C. Anderson. Studies of the woodland light climate: II. Seasonal variation in the light climate. *The Journal of Ecology*, pages 643–663, 1964.

[2] M.C. Anderson. Studies of the woodland light climate: I. The photographic computation of light conditions. *The Journal of Ecology*, pages 27–41, 1964.

[3] Detlev Arendt, Kristin Tessmar, Maria-Ines Medeiros de Campos-Baptista, Adriaan Dorresteijn, and Joachim Wittbrodt. Development of pigment-cup eyes in the polychaete Platynereis dumerilii and evolutionary conservation of larval eyes in Bilateria. *Development (Cambridge, England)*, 129(5):1143–1154, March 2002.

[4] Kenta Asahina, Matthieu Louis, Silvia Piccinotti, and Leslie B Vosshall. A circuit supporting concentration-invariant odor perception in Drosophila. *Journal of biology*, 8(1):9, 2009.

[5] DG Ballinger and S Benzer. Photophobe (Ppb), a Drosophila mutant with a reversed sign of phototaxis; the mutation shows an allele-specific interaction with sevenless. In *Proceedings of the National ...*, 1988.

[6] H C Berg and D A Brown. Chemotaxis in Escherichia coli analysed by three-dimensional tracking. *Nature*, 239(5374):500–504, October 1972.

[7] Howard C Berg. *Random Walks in Biology*. Princeton University Press, revised edition, September 1993.

[8] Neils Bolwig. *Senses and sense organs of the anterior end of the house fly larvae*. København, C.A. Reitzel, 1946.

[9] A H Brand and N Perrimon. Targeted gene expression as a means of altering cell fates and generating dominant phenotypes. *Development (Cambridge, England)*, 118(2):401–415, June 1993.

[10] M Busto, B Iyengar, and A R Campos. Genetic dissection of behavior: modulation of locomotion by light in the Drosophila melanogaster larva requires genetically distinct visual system functions. *The Journal of neuroscience : the official journal of the Society for Neuroscience*, 19(9):3337–3344, May 1999.

[11] S Chung, D Clark, C Gabel, and E Mazur. BMC Neuroscience | Full text | The role of the AFD neuron in C. elegansthermotaxis analyzed using femtosecond laser ablation. *Bmc ...*, 2006.

[12] Ben Collins, Elizabeth A Kane, David C Reeves, Myles H Akabas, and Justin Blau. Balance of activity between LN(v)s and glutamatergic dorsal clock neurons promotes robust circadian rhythms in Drosophila. *Neuron*, 74(4):706–718, May 2012.

[13] Peter Coveney and Roger Highfield. *Frontiers of complexity*. the search for order in a chaotic world. Ballantine Books, August 1996.

[14] Begona De Velasco, Jennifer Shen, Sheryllene Go, and Volker Hartenstein. Embryonic development of the Drosophila corpus cardiacum, a neuroendocrine gland with similarity to the vertebrate pituitary, is controlled by sine oculis and glass. *Developmental biology*, 274(2):280–294, October 2004.

[15] M C Ellis, E M O'Neill, and G M Rubin. Expression of Drosophila glass protein and evidence for negative regulation of its activity in non-neuronal cells by another DNA-binding protein. *Development (Cambridge, England)*, 119(3): 855–865, November 1993.

[16] Joe Kobele Ellsworth. The photorecepetive organs of the fleshfly larva, Lucilia sericata (Meigen): An experimental and anatomical study. *Annals of the Entomological Society of America*, 26:200–215, 1933.

[17] Gottfried Samuel Fraenkel. *The orientation of animals, kineses, taxes and compass reactions,*. kineses, taxes and compass reactions, by Gottfried S. Fraenkel,... and Donald L. Gunn,... Dover Publications, 1961.

[18] Gottfried Samuel Fraenkel and Donald Livingston Gunn. The Orientation of Animals. Oxford University Press, USA, 1940.

[19] Marc Gershow, Matthew Berck, Dennis Mathew, Linjiao Luo, Elizabeth A Kane, John R Carlson, and Aravinthan D T Samuel. Controlling airborne cues to study small animal navigation. *Nature methods*, January 2012.

[20] Alex Gomez-Marin and Matthieu Louis. Active sensation during orientation behavior in the Drosophila larva: more sense than luck. *Current opinion in neurobiology*, December 2011.

[21] Alex Gomez-Marin, Greg J Stephens, and Matthieu Louis. Active sampling and decision making in Drosophila chemotaxis. *Nature communications*, 2: 441, 2011.

[22] Zhefeng Gong. Behavioral dissection of Drosophila larval phototaxis. *Biochemical and biophysical research communications*, 382(2):395–399, May 2009.

[23] Zhefeng Gong, Jiangqu Liu, Chao Guo, Yanqiong Zhou, Yan Teng, and Li Liu. Two Pairs of Neurons in the Central Brain Control Drosophila Innate Light Preference. *Science (New York, N.Y.)*, 330(6003):499–502, October 2010.

[24] Wesley B Grueber, Lily Y Jan, and Yuh Nung Jan. Tiling of the Drosophila epidermis by multidendritic sensory neurons. *Development (Cambridge, England)*, 129(12):2867–2878, June 2002.

[25] Donald L Gunn. The humidity reactions of the woodlouse, Porcellio scaber (Latreille) . *Journal of Experimental Biology*, 1937.

[26] J Hassan, M Busto, B Iyengar, and A R Campos. Behavioral characterization and genetic analysis of the Drosophila melanogaster larval response to light as revealed by a novel individual assay. *Behavior genetics*, 30(1):59–69, January 2000.

[27] Jana Hassan, Balaji Iyengar, Nadia Scantlebury, Veronica Rodriguez Moncalvo, and Ana Regina Campos. Photic input pathways that mediate the-Drosophila larval response to light and circadian rhythmicity are developmentally related but functionally distinct. *The Journal of Comparative Neurology*, 481(3):266–275, 2004.

[28] G Heimbeck, V Bugnon, N Gendre, C Häberlin, and R F Stocker. Smell and taste perception in Drosophila melanogaster larva: toxin expression studies in chemosensory neurons. *The Journal of neuroscience : the official journal of the Society for Neuroscience*, 19(15):6599–6609, August 1999.

[29] C Helfrich-Förster. Neurobiology of the fruit fly's circadian clock. *Genes, brain, and behavior*, 4(2):65–76, March 2005.

[30] William Brodbeck Herms. Ecological and Experimental Study of Sarcophagidae. *Jornal of Experimental Zoology*, 4:45–83, 1907.

[31] William Brodbeck Herms. The photic reactions of sarcophagid flies, especially Lucilia caesar Linn. and Calliphora vomitoria Linn. *Journal of Experimental Zoology*, 10(2):167–226, February 1911.

[32] Axel Hinnemann, Senta Niederegger, Ulrike Hanslik, H-G Heinzel, and Roland Spiess. See the light: electrophysiological characterization of the Bolwig organ's light response of Calliphora vicina 3rd instar larvae. *Journal of insect physiology*, 56(11):1651–1658, November 2010.

[33] James J L Hodge. Ion channels to inactivate neurons in Drosophila. *Frontiers in molecular neuroscience*, 2:13, 2009.

[34] Samuel Jackson Holmes. The selection of random movements as a factor in phototaxis. *Journal of Comparative Neurology and Psychology*, 15:98–112, 1905.

[35] Samuel Jackson Holmes. Studies in animal behavior, 1916.

[36] Cynthia L Hughes and John B Thomas. A sensory feedback circuit coordinates muscle activity in Drosophila. *Molecular and cellular neurosciences*, 35 (2):383–396, June 2007.

[37] Richard Y Hwang, Lixian Zhong, Yifan Xu, Trevor Johnson, Feng Zhang, Karl Deisseroth, and W Daniel Tracey. Nociceptive neurons protect Drosophila larvae from parasitoid wasps. *Current biology : CB*, 17(24):2105–2116, December 2007.

[38] Junko Kasuya, Hiroshi Ishimoto, and Toshihiro Kitamoto. Neuronal mechanisms of learning and memory revealed by spatial and temporal suppression of neurotransmission using shibire, a temperature-sensitive dynamin mutant gene in Drosophila melanogaster. *Frontiers in molecular neuroscience*, 2: 11, 2009.

[39] Alex C Keene and Simon G Sprecher. Seeing the light: photobehavior in fruit fly larvae. *Trends in Neurosciences*, 35(2):104–110, February 2012.

[40] Alex C Keene, Esteban O Mazzoni, Jamie Zhen, Meg A Younger, Satoko Yamaguchi, Justin Blau, Claude Desplan, and Simon G Sprecher. Distinct visual pathways mediate Drosophila larval light avoidance and circadian clock entrainment. *The Journal of neuroscience : the official journal of the Society for Neuroscience*, 31(17):6527–6534, April 2011.

[41] J H Koenig. Reversible control of synaptic transmission in a single gene mutant of Drosophila melanogaster. *The Journal of Cell Biology*, 96(6):1517–1522, June 1983.

[42] Toshio Kosaka and Kazuo Ikeda. Reversible blockage of membrane retrieval and endocytosis in the garland cell of the temperature-sensitive mutant of Drosophila melanogaster, shibirets1. *The Journal of Cell Biology*, 97(2):499–507, August 1983.

[43] Subhaneil Lahiri, Konlin Shen, Mason Klein, Anji Tang, Elizabeth Kane, Marc Gershow, Paul Garrity, and Aravinthan D T Samuel. Two alternating motor programs drive navigation in Drosophila larva. *PloS one*, 6(8):e23180, 2011.

[44] M Lilly and J Carlson. smellblind: a gene required for Drosophila olfaction. *Genetics*, 124(2):293–302, February 1990.

[45] Jacques Loeb. *Studies in general physiology, vol. 1*. The Decennial Publications of the University of Chicago, Chicago, 1905.

[46] Jacques Loeb. The Mechanistic conception of life. University of Chicago Press, Chicago, 1912.

[47] Jacques Loeb. Forced movements, tropisms, and animal conduct. Lippincott, Philadelphia, 1918.

[48] Linjiao Luo, Marc Gershow, Mark Rosenzweig, Kyeongjin Kang, Christopher Fang-Yen, Paul A Garrity, and Aravinthan D T Samuel. Navigational decision making in Drosophila thermotaxis. *The Journal of neuroscience : the official journal of the Society for Neuroscience*, 30(12):4261–4272, March 2010.

[49] Samuel Ottmar Mast. *Light and the behavior of organisms*. New York. J. Wiley & Sons, 1911., 1st ed., 1st thousand. edition, 1911.

[50] Esteban O Mazzoni, Claude Desplan, and Justin Blau. Circadian pacemaker neurons transmit and modulate visual information to control a rapid behavioral response. *Neuron*, 45(2):293–300, January 2005.

[51] MJ McHenry and JA Strother. The kinematics of phototaxis in larvae of the ascidian Aplidium constellatum. *Marine Biology*, 142(1):173–184, 2003.

[52] Bradley M Patten. A quantitative determination of the orienting reaction of the blowfly larva (Calliphora erythrocephala Meigen). *Journal of Experimental Zoology*, 17:213–280, 1914.

[53] Barret D Pfeiffer, Arnim Jenett, Ann S Hammonds, Teri-T B Ngo, Sima Misra, Christine Murphy, Audra Scully, Joseph W Carlson, Kenneth H Wan, Todd R Laverty, Chris Mungall, Rob Svirskas, James T Kadonaga, Chris Q Doe, Michael B Eisen, Susan E Celniker, and Gerald M Rubin. Tools for neuroanatomy and neurogenetics in Drosophila. *Proceedings of the National Academy of Sciences of the United States of America*, 105(28):9715–9720, July 2008.

[54] Georges Pouchet. De l'influence de la lumiere sur les larves de dipthres privikes d'organes exterieurs de la vision. *Revue et Magasin de Zoologie*, 23: 110–17; 129–38; 183–86; 225–31; 261–4; 312–16, 1872.

[55] S Reddy, P Jin, J Trimarchi, P Caruccio, R Phillis, and R K Murphey. Mutant molecular motors disrupt neural circuits in Drosophila. *Journal of Neurobiology*, 33(6):711–723, November 1997.

[56] Verónica G Rodriguez Moncalvo and Ana Regina Campos. Genetic dissection of trophic interactions in the larval optic neuropil of Drosophila melanogaster. *Developmental biology*, 286(2):549–558, October 2005.

[57] FP Sawin, LR Harris, AR Campos, and MB Sokolowski. Sensorimotor Transformation From Light Reception to Phototactic Behavior in Drosophila Larvae (Diptera, Drosophilidae). *Journal of Insect Behavior*, 7(4):553–567, 1994.

[58] E P Sawin-McCormack, M B Sokolowski, and A R Campos. Characterization and genetic analysis of Drosophila melanogaster photobehavior during larval development. *Journal of neurogenetics*, 10(2):119–135, November 1995.

[59] Nadia Scantlebury, Rade Sajic, and Ana Regina Campos. Kinematic analysis of Drosophila larval locomotion in response to intermittent light pulses. *Behavior genetics*, 37(3):513–524, May 2007.

[60] K Scott, R Brady, A Cravchik, P Morozov, A Rzhetsky, C Zuker, and R Axel. A chemosensory gene family encoding candidate gustatory and olfactory receptors in Drosophila. *Cell*, 104(5):661–673, March 2001.

[61] M A Serikaku and J E O'Tousa. sine oculis is a homeobox gene required for Drosophila visual system development. *Genetics*, 138(4):1137–1150, December 1994.

[62] Simon G Sprecher and Claude Desplan. Switch of rhodopsin expression in terminally differentiated Drosophila sensory neurons. *Nature*, 454(7203): 533–537, July 2008.

[63] Simon G Sprecher, Albert Cardona, and Volker Hartenstein. The Drosophila larval visual system: high-resolution analysis of a simple visual neuropil. *Developmental biology*, 358(1):33–43, October 2011.

[64] S T Sweeney, K Broadie, J Keane, and H Niemann. ScienceDirect.com - Neuron - Targeted expression of tetanus toxin light chain in Drosophila specifically eliminates synaptic transmission and causes behavioral defects. *Neuron*, 1995.

[65] MP Thekaekara. Solar radiation measurement: techniques and instrumentation. *Solar Energy*, 18(4):309–325, 1976.

[66] Alexander M van der Bliek and Elliot M Meyerowrtz. Dynamin-like protein encoded by the Drosophila shibire gene associated with vesicular traffic. *Nature*, 351(6325):411–414, May 1991.

[67] Yang Xiang, Quan Yuan, Nina Vogt, Loren L Looger, Lily Yeh Jan, and Yuh Nung Jan. Light-avoidance-mediating photoreceptors tile the Drosophila larval body wall. *Nature*, 468(7326):921–926, December 2010.

[68] Lixian Zhong, Richard Y Hwang, and W Daniel Tracey. Pickpocket is a DEG/ENaC protein required for mechanical nociception in Drosophila larvae. *Current biology : CB*, 20(5):429–434, March 2010.

4

Appendix1: Rictor/TORC2 regulates fat metabolism, feeding, growth and life span in *Caneorhabditis elegans*

4.1 Authors

Alexander A. Soukas, Elizabeth A. Kane, Christopher E. Carr, Justine A. Melo, and Gary Ruvkun

4.2 Publication note

A version of this appendix was published as the following article: Soukas AA, Kane EA, Carr CE, Melo JA, Ruvkun G. Rictor/TORC2 regulates fat metabolism, feeding, growth, and life span in Caenorhabditis elegans. *Genes Dev.* 2009 Feb 15;23(4):496-511.

4.3 Abstract

Rictor is a component of the target of rapamycin complex 2 (TORC2). While TORC2 has been implicated in insulin and other growth factor signaling pathways, the key inputs and outputs of this kinase complex remain unknown. We identified mutations in the *Caneorhabditis elegans* homolog of *rictor* in a forward genetic screen for increased body fat. Despite high body fat, *rictor* mutants are developmentally delayed, small in body size, lay an attenuated brood, and are short-lived, indicating that Rictor plays a critical role in appropriately partitioning calories between long-term energy stores and vital organismal processes. Rictor is also necessary to maintain normal feeding on nutrient-rich food sources. In contrast to wild-type animals, which grow more rapidly on nutrient-rich bacterial strains, *rictor* mutants display even slower growth, a further reduced body size, decreased energy expenditure, and a dramatically extended life span, apparently through inappropriate, decreased consumption of nutrient-rich food. Rictor acts directly in the intestine to regulate fat mass and whole-animal growth. Further, the high-fat phenotype of *rictor* mutants is genetically dependent on *akt-1*, *akt-2*, and serum and glucocorticoid-induced kinase-1 (*sgk-1*). Alternatively, the life span, growth, and reproductive phenotypes of *rictor* mutants are mediated predominantly by *sgk-1*. These data indicate that Rictor/TORC2 is a nutrient-sensitive complex with outputs to AKT and SGK to modulate the assessment of food quality and signal to fat metabolism, growth, feeding behavior, reproduction, and life span.

4.4 Introduction

The target of rapamycin (tor) gene is conserved from slime molds to mammals. TOR exists in two structurally and functionally distinct multi-protein complexes whose components are highly conserved across phylogeny, TOR complex 1 (TORC1) and TORC2 (Sarbassov et al. 2005a; Bhaskar and Hay 2007). TORC1 regulates cell growth, protein synthesis, and autophagy, whereas TORC2 has been implicated in cytoskeletal reorganization in cell lines (Sarbassov et al. 2005b). Because of the embryonic lethality of TORC2 component knockout mice (Guertin et al. 2006; Shiota et al. 2006; Yang et al. 2006), its in vivo role can only be assessed using tissue-specific inactivation in mammals (Bhaskar and Hay

2007).

In multicellular eukaryotes, TORC2 is composed of TOR, mLST8 Rictor, Sin-1, and Protor (Sarbassov et al. 2004; Frias et al. 2006; Yang et al. 2006; Pearce et al. 2007). TORC2 was recently identified as the hydrophobic motif (HM) kinase of AKT and may also regulate PDK1-mediated phosphorylation of AKT (Hresko and Mueckler 2005; Sarbassov et al. 2005b). Phosphorylation of the HM is important for AKT to phosphorylate downstream targets, such as mFOXO3, in an insulin-dependent manner (Guertin et al. 2006). However, TORC2 may also phosphorylate other AGC family kinases, such as protein kinase C (PKC) and SGK (Sarbassov et al. 2004; Guertin et al. 2006; Garcia-Martinez and Alessi 2008).

In *Saccharomyces cerevisiae*, *Schizosaccharomyces pombe*, and mammals, genetic inactivation of TORC2 is lethal (Schmidt et al. 1996; Kamada et al. 2005). The lethality in yeast is due to defects in cytoskeletal arrangement and ceramide synthesis (Schmidt et al. 1996; Tabuchi et al. 2006; Aronova et al. 2008). Genetic screens identified gain-of-function alleles of a yeast homolog of SGK, Ypk2, as suppressors of the lethality of TORC2 mutations (Kamada et al. 2005). Furthermore, Ypk2 gainof-function mutations fully rescue the ceramide synthesis defects of TORC2 mutants (Aronova et al. 2008), identifying the SGK homolog as a critical downstream effector of TORC2 in yeast.

In mammals, TOR, Rictor, Sin-1, and mLST8 are all necessary for the assembly, full activity, and substrate specificity of the TORC2 complex. Activation of TORC2 kinase activity by growth factors or insulin is abrogated by elimination of any component in mouse embryonic fibroblasts (MEFs) (Frias et al. 2006; Guertin et al. 2006; Shiota et al. 2006; Yang et al. 2006). Studies of TORC2 component knockout mice have been limited due to defects in placentogenesis and embryogenesis that result in lethality by embryonic day 10.5 (E10.5) to E11.5 (Guertin et al. 2006; Shiota et al. 2006), although muscle-specific inactivation of *rictor* produces glucose intolerance and increased basal glycogen synthesis (Bentzinger et al. 2008; Kumar et al. 2008), presumably via decreased AKT HM phosphorylation.

In *Caneorhabditis elegans*, as in mammals, insulin-like signaling through PI3 Kinase regulates fat mass, life span, and whole-organism metabolism (Morris et al. 1996; Ogg et al. 1997; Ogg and Ruvkun 1998; Paradis and Ruvkun 1998; Paradis et al. 1999; Wolkow et al. 2000; Porte et al. 2005). While TORC2 has been firmly implicated in insulin signaling (Bhaskar and Hay 2007), its role in whole-organism

fat mass and life-span regulation has yet to be determined. Here we present evidence that TORC2 functions in vivo to regulate the metabolic state of *C. elegans*. Mutations in *C. elegans rictor* show elevated body fat content, defective feeding behavior on different bacterial diets, and shortened life span. Furthermore, for all phenotypes except for triglyceride accumulation, *sgk-1* phenocopies *rictor*, implicating SGK-1 as the critical downstream kinase of TORC2 for these phenotypes. For the full high-fat phenotype of *rictor* mutants, the AKT homologs *akt-1* and *akt-2* are necessary in addition to *sgk-1*.

4.5 Results

4.5.1 Identification and expression of the *C. elegans* homolog of Rictor, RICT-1

We identified two mutantions in the *C. elegans* homolog of *rictor* (F29C12.3, subsequently referred to as *rict-1*) based on a classical, forward genetic screen for substantially increased fat mass in animals fed the standard laboratory bacteria, *Escherichia coli* OP50. While *C. elegans* was not initially predicted to contain a homolog of Rictor, this was likely due to misannotation of the gene to two separate mRNAs, F29C12.2 and F29C12.3, separated by an intronic gene in the antisense direction, *pqn32* (F29C12.1), and that *rictor* is divergent among eukaryotes, sharing only 44% similarity in a conserved region of 200 amino acids (Sarbassov et al. 2004). *C. elegans* RICT-1 is approximately as similar to mammalian Rictor as Drosophila Rictor (16% identity and 50% similarity and 22% identity and 57% similarity, respectively, over the entire coding region). In addition, BLASTP comparison of *C. elegans* RICT-1 versus the human genome database detects Rictor as the top hit with an e value of e-33, and and the converse search detects *C. elegans* RICT-1 as the only homolog, with an e value of e-35.

The two alleles of *rict-1* that emerged from the high-fat genetic screen contain early stop mutations in the coding region of *rict-1*, removing 97 (allele *mg450*) or 211 (allele *mg451*) of the 1580 amino acids encoded by the major mRNA species (Supplemental Figure 4.8). *mg450* and *mg451* are predicted to be loss-of-function mutations based on the removal of a highly conserved C-terminal region (Supplemental Figure 4.8), recessive inheritance, and non-complementation of *mg450*

and *mg451*. Furthermore, the high-fat phenotype is phenocopied by RNAi of *rict-1* (Supplemental Figure 4.9), and a *rict-1* promoter-driven *rict-1* cDNA transgene rescues the high-fat, small body size, and life span phenotypes (Supplemental Figure 4.10A). RNAi of *rict-1* does not further enhance the high-fat phenotype of *rict-1* mutants, supporting the probable null nonsense mutations (Supplemental Figure 4.9B). *rict-1* is expressed in the nervous system (head neurons, ventral nerve cord), intestine, body wall muscle, pharynx, and spermatheca as assessed by a promoter-driven RFP reporter (Supplemental Figure 4.10B). In adult animals, the most prominent sites of expression are head neurons and the intestine (Supplemental Figure 4.10B). In support of *rict-1* mutations acting to increase fat mass through TORC2 and not through associations with other cellular signaling components, RNAi of *sinh-1*, the *C. elegans* homolog of the TORC2 complex component *mSin1*, also produces a high-fat phenotype (Supplemental Figure 4.9)

4.5.2 RICT-1 REGULATES FAT MASS AND THE RESPONSE TO DIFFERENT DIETS

While wild-type animals increase fat mass, as assessed by labeling with the fluorescent fatty acid analog C1C12BODIPY, when fed the nutrient-rich bacterial strain E. coli HB101 as compared with the relatively nutrient-poor OP50 (Figure 4.3A). HB101 is considered to be nutrient-rich based on its superior ability to support wild-type *C. elegans* growth when compared with an OP50-derived strain (Avery and Shtonda 2003; Shtonda and Avery 2006). Compared with OP50, wild-type *C. elegans* fed HB101 develop from egg to reproductive adult >10 h faster (Figure 4.1G; Avery and Shtonda 2003), demonstrate increased intestinal BODIPY fat staining, and increase oxygen consumption (Figure 4.1A,B,D).

When fed OP50, *rict-1* mutants display a 200%-300% increase in BODIPY fat content as day 3 adults (Figure 4.1A,B). A 30%-50% increase is seen in *rict-1* mutants as day 1 adults (Figure 4.3A, below), indicating that BODIPY accumulation is preferentially activated post-developmentally during the reproductive period. Despite having dramatically high lipid levels, *rict-1* mutants are delayed 16 h in reaching reproductive maturity (Figure 4.1G), and mature adults matched for developmental stage are smaller (Figure 4.1C). This highlights a conserved role for TORC2 in growth as *rictor* also regulates body size in *Drosophila* (Lee and Chung 2007),

Figure 4.1 *(following page)*: The metabolic defects of *rict-1* mutants. (A,B) BODIPY-labeled fatty acid vital dye revealed a threefold to fourfold increase in fat content in both *rict-1* alleles (mg450 and mg451) relative to wild type (N2) as day 3 adults when fed E. coli OP50 bacteria. This phenotype was not evident when *rict-1* mutant animals were fed E. coli HB101. (C) Body size is 24%-38% reduced in *rict-1* mutants and further reduced by feeding HB101. (D) Energy expenditure is reduced slightly in *rict-1* mutants, increased in wild type by feeding HB101versus OP50, and decreased by HB101 versus OP50 in *rict-1* (*mg451*). (E) Food intake as measured by pharyngeal pumping rate when animals are on food is equivalent in wild-type and *rict-1* mutant worms on OP50. On HB101, wild-type worms decrease pumping rate as day 1 adults, but *rict-1* mutants maintain a higher pumping rate on HB101. However, *rict-1* mutants spend less time on HB101 and therefore consume less of this bacteria. (F) Brood size is reduced 45%-67% in *rict-1* mutants and in the mg451 allele is reduced further by HB101 feeding. (G) Egg-to-egg time is delayed 16 h in *rict-1* mutants. Feeding HB101 accelerates egg-to-egg time by 10 h in wild-type worms and paradoxically slows this interval by 2.5 h in *rict-1* mutants. (y) $P < 0.05$ versus wild-type; (*) $P < 0.05$ versus same strain on OP50 by two-tailed, equal variance t-test. Error bars indicate +/- SD, except for G, where they indicate +/- SEM.

Figure 4.1: (continued)

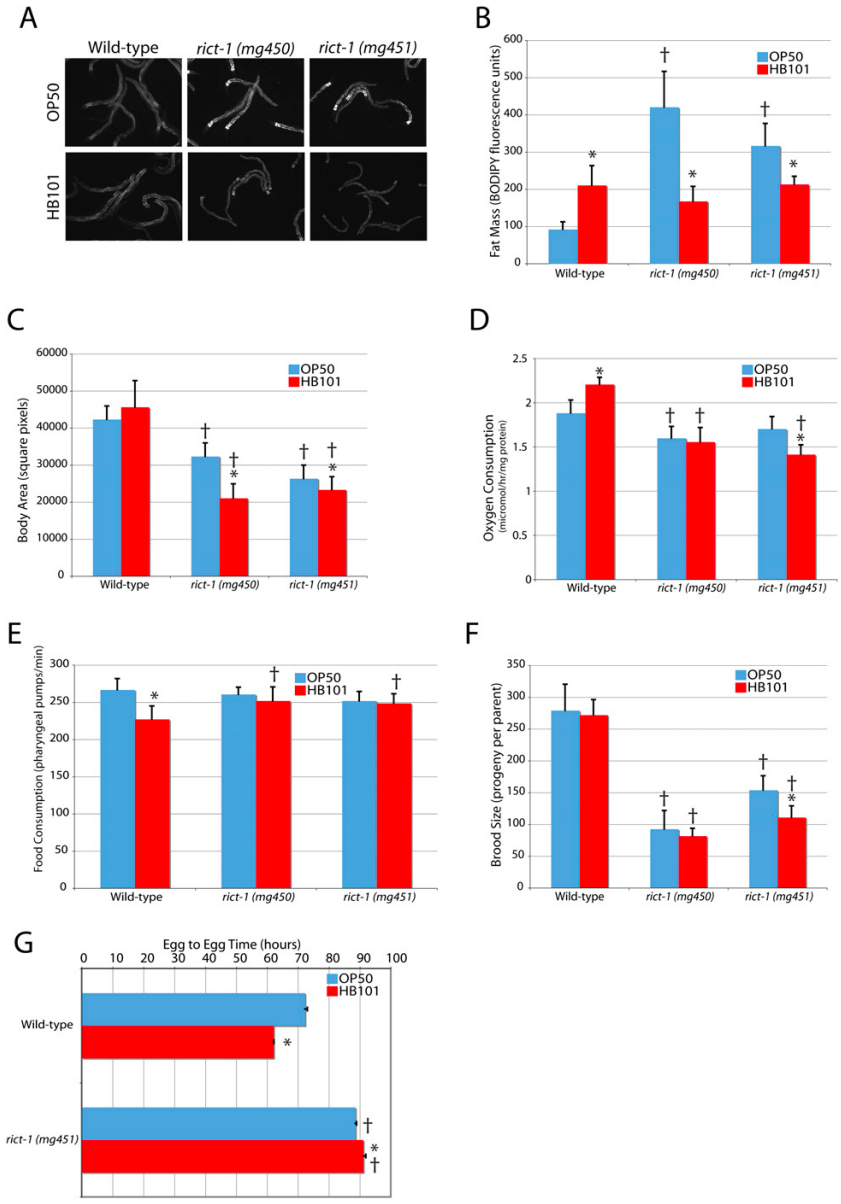

and the murine embryos of TORC2 knockout components are small (Guertin et al. 2006).

Increased food consumption is not responsible for the observed fat-level differences in high-fat *rict-1* animals (Figure 4.1E). A nonsignificant trend toward decreased oxygen consumption was seen in *rict-1*(*mg451*) animals [significant in *rict-1*(*mg450*) animals], and thus decreased energy expenditure may play some role in the development of the high-fat phenotype of *rict-1* mutants. *rict-1* mutants display an attenuated brood size of 30%-50% as compared with wild type (Figure 4.1F). Therefore, shunting of calories away from reproduction or growth or inadequate utilization of stored fat could also provide an explanation for the elevated fat content of *rict-1* mutants.

Surprisingly, *rict-1* mutants displayed a paradoxical, detrimental response to HB101 feeding in all metabolic phenotypes examined: The BODIPY high-fat phenotype of the *rict-1* animals fed OP50 was not evident when feeding HB101 bacteria (Figure 4.1A,B), body size decreased (Figure 4.1C), oxygen consumption did not increase (Figure 4.1D), total brood size decreased (in the stronger *mg451* allele) (Figure 4.1F), and time to reproductive maturity was further delayed by >2.5 h (Figure 4.1G). This suggests either that *rict-1* animals eat less when fed HB101 or that *rict-1* mutations prevent utilization of nutrients particular to the HB101 strain. A decreased pumping rate was not evident in *rict-1* animals found on the lawn of bacteria (Figure 4.1E). However, when put on a plate with HB101, *rict-1* mutant animals displayed decreased residence time on the lawn of food (day 1 adult wild-type worms off HB101 lawn 3.1% 6 0.9% vs. *rict-1* mutants off HB101 lawn 10.8% 6 1.5%; $P < 0.01$), suggesting that over time they may consume less HB101. We also observed decreased lawn residence when RNAi was used to knock down *rict-1*, leading to 26.7% 6 7.3% and 36.9% 6 2.1% of animals being off the lawn for two different RNAi clones targeting *rict-1* (vs. 0% 6 0% for vector RNAi control). This indicates that Rictor/TORC2 is necessary for proper feeding behavior as wild-type worms normally do not decrease residence on the lawn of food when fed HB101 or the E. coli strain HT115 used to conduct RNAi. Of note, both HB101 and HT115 are closely related to each other and to the E. coli strain K12, versus OP50, which is much more closely related to the E. coli B strain (B. Samuel and G. Ruvkin, unpubl.). In insulin/IGF signaling pathway mutants, BODIPY and

Nile red do not accurately indicate body fat mass.

Insulin-like signaling in many animals, including *C. elegans*, is a major endocrine signal of nutrients and fat (Porte et al. 2005). Since TORC2 had been reported to activate AKT via HM phosphorylation, we examined the relationship between the BODIPY high-fat phenotype of *rict-1* mutants and the insulin/IGF/AKT signaling pathway (Supplementary Figure 4.11). When assessed by BODIPY-labeled fatty acids, inactivation of *daf-2*/ insulin-like signaling or *akt-1* loss-of-function mutations (lf) in combination with *rict-1* reduced fat mass to wild-type or lower levels, suggesting that insulin-like signaling through *akt-1* is required for the development of the high-fat phenotype of *rict-1* mutants (Figure 4.2A). Additionally, *daf-16* animals accumulated more BODIPY, and *rict-1*;*daf-16* double mutants showed an even greater increase than either single mutant (Figure 4.2B). However, the BODIPY phenotype of *daf-2* mutant animals was puzzlingly contradictory to the previously reported high-fat phenotypes determined by Sudan black fixative-based staining (Kimura et al. 1997; Ogg et al. 1997) and biochemical fat quantitation using solid-phase chromatography or thin-layer chromatography followed by gas chromatography/mass spectroscopy (Ashrafi et al. 2003; Perez and Van Gilst 2008). As BODIPY fat mass assessment requires normal feeding, uptake, and accumulation, this raises the possibility that BODIPY fat mass assessment may not be accurate when mutants consume more or less food or uptake and accumulate the dye with different efficiency.

4.5.3 RICT-1 PARTIALLY REGULATES FAT VIA INSULIN-LIKE SIGNALING THROUGH AKT

To more accurately assess fat storage using histochemistry, we fixed adult animals of various genotypes and assayed stored neutral lipid using the standard assay for adipocyte fat storage, the dye Oil-Red-O (Soukas et al. 2001). Oil-Red-O staining of *rict-1* mutants recapitulated the high-fat phenotype of *rict-1* mutants fed BODIPY labeled fatty acids (Figure 4.3A). Oil-Red-O, unlike Sudan black staining, is much more consistent across animals of a given genotype and correlated well with biochemical measurements of triglyceride mass (see below), and was thus used preferentially to assess fat mass. The *rict-1* allele *mg451* demonstrated

Figure 4.2 *(following page)*: BODIPY-labeled fatty acid assessed fat mass interaction of *rict-1* with insulin/IGF signaling components. (A) *rict-1* BODIPY fat mass accumulation is reduced by combination with the insulin/IGF-1 receptor hypomorphic mutation *daf-2* (e1370) or *akt-1 (mg306)*-null mutation. *rict-1* fat accumulation is not affected by the *akt-2 (*ok393*)*-null mutation. BODIPY measurements were inconsistent with previous examinations of *daf-2* mutant worms demonstrating increased fat mass by fixative-based lipid staining with Sudan black or biochemical measurement of triglyceride content. Mean of two experiments ± SEM. (*) $p < 0.01$versus wild type; (**)$p< 0.001$ versus wild type; †† $p< 10^{-}6$ versus *rict-1* single mutant. (B) Fat mass of *rict-1*; *daf-16/FOXO(mgDf47)* double mutants is significantly elevated above *rict-1* single mutants on OP50. A small but significant elevation was also seen in *daf-16/FOXO* single mutants that did not phenocopy the magnitude of fat elevation in *rict-1* mutants. Mean ± SEM. (**) $p < 10^{-6}$ versus wild type; (††) $p < 10^{-6}$ versus *rict-1* single mutant.

Figure 4.2: (continued)

A

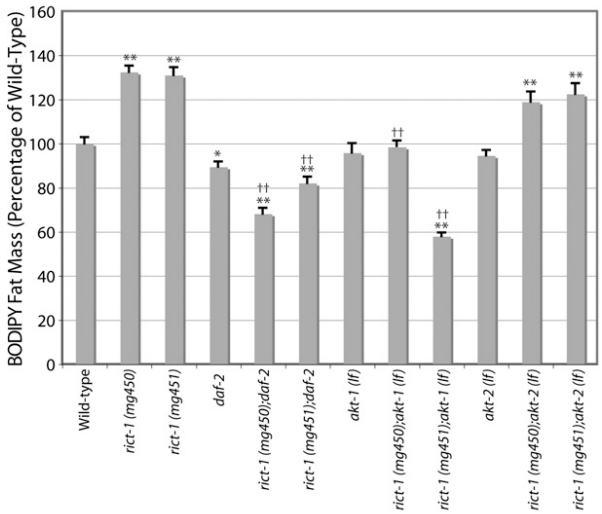

B

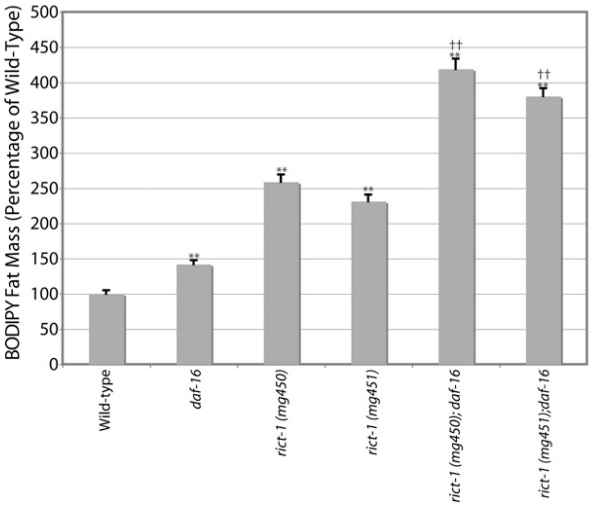

stronger staining with OilRed-O than the *mg450* allele and was used for all subsequent analyses. Biochemical assessment of triglyceride mass using solid-phase chromatography followed by gas chromatography/mass spectroscopy (Perez and Van Gilst 2008) in day 1 adult *rict-1* mutants was ;30% elevated (**??**B), confirming the results obtained with neutral lipid staining with Oil-Red-O. However, the increase in BODIPY fat mass in wild-type worms fed HB101 when compared with OP50 was no longer evident when worms were stained with Oil-Red-O; in fact, HB101 feeding led to decreases in fat mass in both wild-type worms and in *rict-1* mutants as assessed by Oil-Red-O and by biochemical quantitation of triglyceride content (Figure 4.3A,B). *rict-1* mutants, despite having lower fat mass on HB101 than on OP50, still demonstrated elevated triglyceride accumulation above wild-type HB101 levels (Figure 4.3A,B). This indicates that despite decreased lawn residence time on HB101, *rict-1* animals still accumulate greater amounts of triglyceride.

Oil-Red-O staining of *daf-2* mutants showed elevated fat mass (Figure 4.3C), as previously observed with other fixative stains (Kimura et al. 1997; Ogg et al. 1997). Additionally, *akt-1* mutants demonstrated an increase in Oil-Red-O staining, consistent with AKT-1 participating in metabolic signaling (Figure 4.3C). These results were confirmed by quantitative biochemical analysis of triglycerides and phospholipids in *daf-2* and *akt-1* mutants (Figure 4.3D). Interestingly, we found *rict-1*;*daf-2* and *rict-1*;*akt-1* double mutants to have fat mass above either single mutant, indicating that it is unlikely that *rict-1* regulates fat mass exclusively through insulinlike signaling via *akt-1*. The increase in fat mass evident in *rict-1* mutants was partially blunted in the *rict-1*;*akt-2* double mutant (Figure 4.3C,D), suggesting that *akt-2* plays a positive role in the generation of the highfat phenotype of *rict-1* mutants, or that increased *akt-1* signaling in an *akt-2* mutant may partially suppress the *rict-1* phenotype.

To explore interactions with insulin-like signaling further, we examined interactions of *rict-1* with the single *C. elegans* FOXO homolog *daf-16*. *daf-16* is epistatic to the long-lived, dauer, and high-fat phenotypes of insulin-signaling mutant inactivations (e.g., insulin/IGF receptor mutant *daf-2*, PI3K homolog mutants age-1, or *akt-1*;*akt-2* double mutants) (Kimura et al. 1997; Ogg et al. 1997; Finch and

Figure 4.3 ***(following page)*****:** Oil-Red-O staining and quantitative lipid biochemistry in *rict-1*) mutants. (A) Oil-Red-O staining confirms elevated fat mass in *rict-1*) mutants fed E. coli OP50. Lipid is evident in red droplets. Fat mass in worms fed *E. coli* HB101, unlike in BODIPY fatty acid labeling, is lower in wild-type worms and *rict-1*) mutants, but *rict-1*) mutants have relatively elevated fat mass on either diet. (B) Quantitation of lipid species by solidphase extraction followed by gas chromatography and mass spectroscopy in day 1 adult *rict-1*) mutants revealed a 30% increase in triglyceride mass when normalized to total phospholipid content. In both wild-type and *rict-1*) mutants, lipid mass is lower when animals are fed HB101, supporting the Oil- Red-O staining observations, in contrast to what is seen with BODIPY staining. (†) $p < 0.05$ versus wild type; (*) $p < 0.05$ versus same strain on OP50 by two-tailed, equal variance t-test. Mean $\pm$ SEM for four biological replicates. (C,D) Oil-Red-O staining and quantitative lipid biochemistry of *rict-1*) double mutants with *daf-2/InsulinR*, *akt-1, akt-2*, and *daf-16/FOXO*. Fat mass of *rict-1*) mutants is additive with *daf-2*, partially additive with *akt-1*, partially blunted by *akt-2*, and unaffected by *daf-16*. These methods confirm the previous observations of *daf-2* mutants having elevated triglyceride mass. Mean $\pm$ SEM for paired biological replicates.

Figure 4.3: (continued)

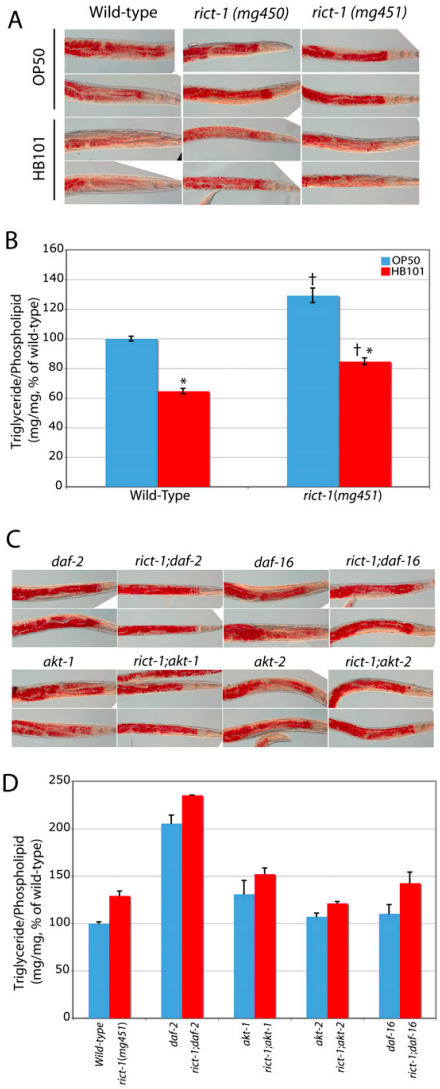

Ruvkun 2001). If mutations in *rict-1* increase fat by loss of AKT-mediated phosphorylation and inhibition of FOXO, FOXO loss of function should be epistatic to *rict-1* (i.e., the high-fat phenotype should be mitigated). This was not the case, as *rict-1*;*daf-16* double mutants fed OP50 show an identical increase in fat mass when compared with *rict-1* single mutants when assessed by Oil-Red-O and quantitative lipid biochemistry (Figure 4.3C,D). This supports the conclusion that *rict-1* also regulates fat in parallel to insulin-like signaling through *daf-2*, *akt-1*, and *daf-16*.

4.5.4 RICT-1 REGULATES LIFE SPAN IN A DIET-DEPENDENT MANNER

Because nutrient availability is a critical determinant of life span and TORC1 component mutants CeTor(let-363) and CeRaptor(daf-15) have been reported to be long-lived on OP50 (Vellai et al. 2003; Jia et al. 2004; Long et al. 2004; Meissner et al. 2004), we assayed the longevity of *rict-1* mutant animals. Unlike tor and CeRaptor mutants, *rict-1* mutants display an increased rate of aging and were short-lived on OP50 (Figs. Figure 4.2, 4A; Supplemental Figure 4.17). This was unexpected, given that TORC2 has been reported to activate the insulin/IGF pathway signaling component AKT and reduction of insulin/IGF signaling in *C. elegans* and higher organisms increases life span (Finch and Ruvkun 2001; Wolff and Dillin 2006). This suggests that TORC2 is unlikely to regulate life span by activating AKT in worms fed OP50. Unlike wild-type animals, which do not appreciably change (Figure 4.4B,C) or slightly decrease life span (Supplemental Figure 4.12A,B) in response to nutrient-rich food (HB101), *rict-1* mutants feeding on HB101 have a profoundly extended life span (Figs. Figure 4.2, Figure 4.4B,C; Supplemental Figure 4.13; Supplemental Figure 4.17). A similar observation was made when mutants were fed the E. coli strain HT115 (Figure 4.4D,E). This is consistent with decreased consumption of nutrient-rich food by *rict-1* mutants, as decreased caloric intake is well known to prolong life span in *C. elegans* and other organisms (Wolff and Dillin 2006).

To formally test the possibility that *rict-1* mutants have life-span extension on HB101 due to decreased caloric intake, life span was studied in *rict-1*;*skn-1* double mutants fed HB101, since *skn-1* is required for dietary restriction-induced

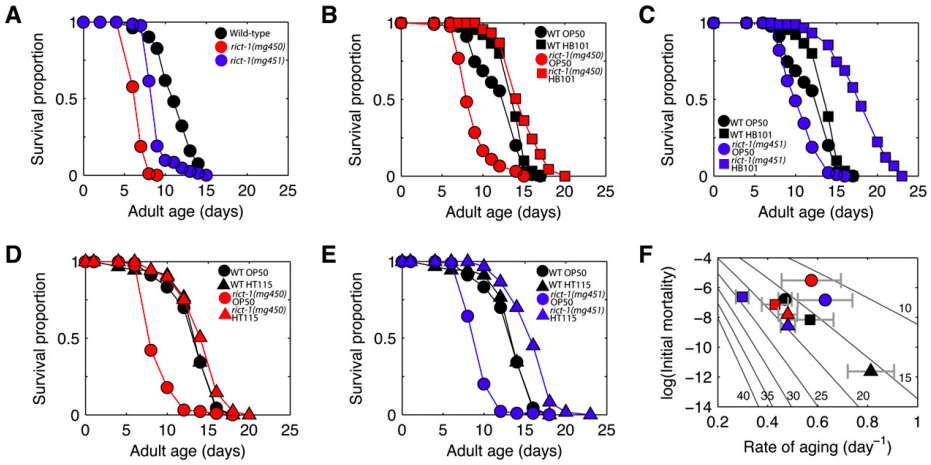

Figure 4.4: The life span of *rict-1* mutants is highly responsive to diet, unlike wild type. (A) Median life span of *rict-1* mutants is reduced 24%-43% on OP50 relative to wild type (N2). (B) While HB101 versus OP50 had marginal (13%) impact on wild-type life span, HB101 extended *rict-1 (mg450)* life span by 75%. In a repeat experiment (Supplemental Figure 4.12A), life span impacts were 13% and 54%, respectively. (C) HB101 versus OP50 diet had a similar impact on *rict-1(mg451)*, increasing life span by 75%, and in a repeat experiment (Supplemental Figure 4.12B) by 74%. (D,E) Similar to HB101, feeding the K12 derived strain E. coli HT115 had insignificant (2%) impact on wild-type life span versus OP50, whereas for *rict-1 (mg450)* (D) and *rict-1 (mg451)* (E), life span increased by 71% and 76%, respectively. (F) Changes in diet affect Gompertz parameters for wild type but not life span, because a higher rate of aging is coupled with lower initial mortality; in contrast, *rict-1* mutants have higher rates of aging at comparable initial mortality on OP50 versus HB101 and HT115. Error bars $\pm$ SD. (Gray diagonals) Lines of constant life span calculated assuming zero accident rate. Legend for F as in B-E.

longevity (Bishop and Guarente 2007). No life-span extension was seen in *rict-1*;*skn-1* double mutants fed HB101, supporting the conclusion that decreased consumption of HB101 is responsible for life-span extension in *rict-1* worms (Supplemental Figure 4.12C). In contrast, tor and raptor *C. elegans* mutants show increased fat content but arrest before adulthood in an incomplete dauer-like state (Long et al. 2002; Jia et al. 2004) and are thus fundamentally different from *rict-1*.

4.5.5 Insulin-like signaling through AKT is necessary but not sufficient for the short life span of *rict-1* mutants

The short-life-span phenotype of *rict-1* mutants requires *daf-2* and *akt-1* signaling as *rict-1*;*akt-1* double mutants shift to being long-lived, rather than short-lived, and rict1;*daf-2* double mutants show a life span nearly identical to *daf-2* mutants (Figure 4.5A-D). *rict-1*;*akt-2* double mutants have life spans similar to *rict-1* single mutants (Figure 4.5E,F). These data suggest that a high level of insulin-like signaling via the *daf-2* and *akt-1* pathway is necessary for the short life span of the *rict-1* mutant. However, *rict1*;*daf-16* double mutants demonstrate shorter life span than either single mutant, indicating that *rict-1* does not shorten life span only via regulation of the DAF-16/FOXO transcriptional outputs of insulin signaling (Figure 4.5G,H; Supplemental Figure 4.18). Furthermore, *rict-1*;*akt-1*(gf) double mutants also demonstrate a significantly shorter life span than either single mutant (Figure 4.5I,J). Thus, *rict-1* generates these phenotypes by also signaling in parallel to *akt-1* and FOXO.

4.5.6 Mutations in *sgk-1* phenocopy and do not enhance *rict-1* growth, reproductive, and life-span defects

Because *akt-1* and *akt-2* signaling do not explain the growth, high-fat, reproductive, life-span, and feeding defects in *rict-1* mutants, we returned to the mutant collection generated in the forward genetic screen for elevated fat mass. Examining these mutants for high fat and small body size indicated an additional complementation group defined by two mutants that mapped to a region on the long arm of chromosome X containing the AGC family kinase *sgk-1*. The Ashrafi laboratory had informed us previously that *sgk-1* acts in the same genetic pathway as

Figure 4.5 *(following page)*: Life-span regulation by insulin/IGF signaling in *rict-1* mutants. (A-D) Life span is extended in *rict-1;daf-2* and *rict-1;akt-1(lf)* double mutants. This is in contrast to the normal short life span of *rict-1* mutants, which requires intact insulin-like signaling through *akt-1* to shorten life span. (E,F) *rict-1;akt-2(lf)* double mutants do not show alteration in life span, indicating that the primary interaction is between *rict-1* and *akt-1*. (G-J) Life span of *rict-1;daf-16/FOXO (mgDf47)* and *rict-1;akt-1(gain of function*) on OP50 is shortened significantly relative to single mutants, indicating that insulin signaling regulates life span in parallel to TORC2, and that lack of *akt-1* activation, leading to decreased inhibitory phosphorylation (thus, activation) of *daf-16/FOXO*, is not responsible for life-span shortening in *rict-1* mutants. (Tabular data is available in Supplemental Figure **??**

Figure 4.5: (continued)

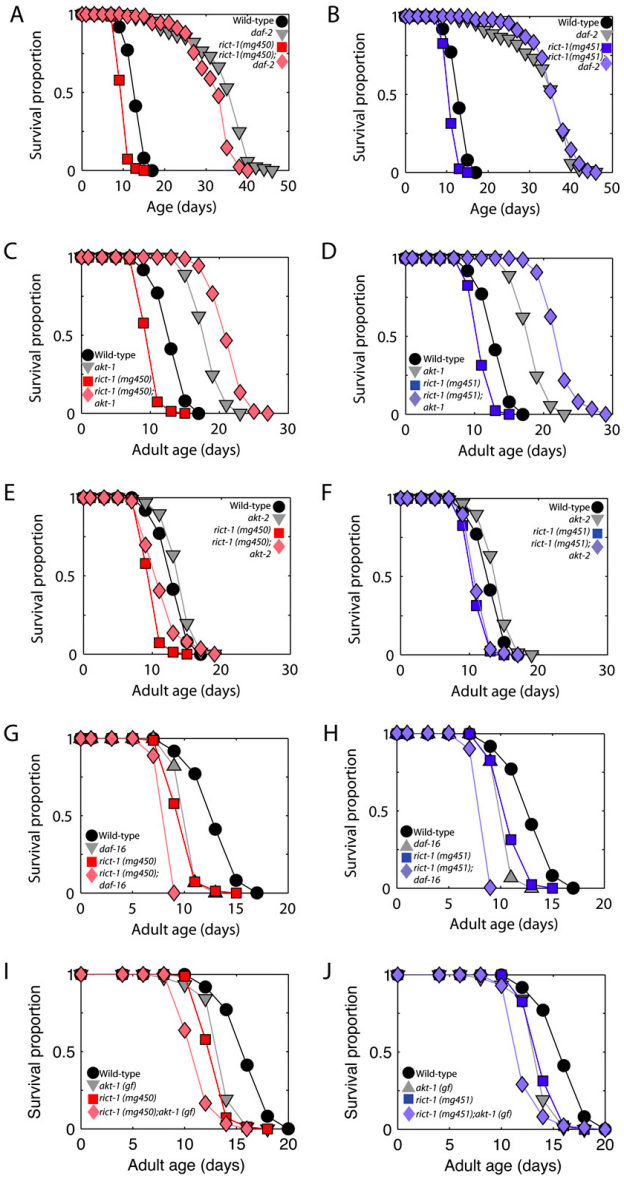

rict-1 by their analyses using the vital dye Nile red (K. Jones and K. Ashrafi, pers. comm.) and it had been shown previously that the *sgk-1(ok538)* allele also affects body size (Hertweck et al. 2004), as did our two mutants mapping to this 1.0-cM genetic region, so this gene was likely to be affected in these two alleles. Sequencing of *sgk-1* exons in these two mutants identified two mutations: a nonsense mutation that removes 178 residues including critical components of the kinase domain and the HM phosphorylation site (mg455), and a missense mutation that changed a non-conserved proline residue to serine (mg456) (Supplemental Figure 4.14).

Examination of *sgk-1* mutants indicated an identical BODIPY phenotype to *rict-1* when fed OP50 and HB101 (Figure 4.6A); i.e., elevated BODIPY staining on OP50 and normal staining when fed HB101. Additionally, *sgk-1* mutants have decreased body size, are slow growing, and have decreased brood size (Figure 4.6C-E). These phenotypes were nearly identical when examined in a rict1;*sgk-1* double mutant, indicating that these genes are likely to be in the same genetic pathway (Figure 4.6C-E). The *rict-1*;*sgk-1* double mutant was slightly slower in reaching reproductive maturity (Figure 4.6D), which could indicate divergence of action of *rict-1* and *sgk-1* in regulating developmental rate. However, the fat mass as assessed by Oil-Red-O staining in *sgk-1*(mg455), which encodes a predicted null allele, was not increased as greatly as in *rict-1* mutants (Figure 4.6F). Quantitative biochemical analysis confirmed this observation and indicated greater fat mass in the *rict-1*;*sgk-1* double mutant than the *sgk-1* single mutant (Figure 4.6G). This suggests that outputs of TORC2 other than *sgk-1* may be necessary for the full extent of the high-fat phenotype. In contrast, *sgk-1* mutants fed OP50 display an identically shortened life span when compared with *rict-1* and *rict-1*;*sgk-1* double mutants (Figure 4.6H), indicating that these genes are likely in the same genetic pathway regulating life span. Thus, the life span, growth, reproductive, and BODIPY or Nile red increase phenotypes of *rict-1* may be explained by *sgk-1*, but not the full extent of triglyceride accumulation assessed biochemically and by Oil-Red-O staining.

Figure 4.6 *(following page)*: sgk-1 and *rict-1*;*sgk-1* double-mutant analysis. (A) BODIPY-labeled fatty acid fat mass imaging of two alleles of *sgk-1* that have elevated fat mass indicate a similar phenotype to *rict-1* mutants: high BODIPY signal when fed OP50 and blunting of BODIPY staining and smaller body size when fed HB101. (B-E) Analysis of *rict-1*;*sgk-1* double mutants indicates that *sgk-1* phenocopies *rict-1* for BODIPY fat mass, body size, and egg-to-egg time, and that none of these phenotypes is enhanced in the *rict-1*;*sgk-1* double mutant. Mean ± SEM. (*) $p < 0.05$ versus wild type; † $p < 0.05$ versus same strain on OP50. (F,G) Oil-Red-O staining and quantitative lipid biochemistry of *rict-1*, *sgk-1*, and *rict-1*;*sgk-1* show that *rict-1* produces a higher-fat phenotype than is explained by *sgk-1* alone, indicating that TORC2 has additional outputs other than *sgk-1* to regulate fat mass. Mean ± SEM. (H) Unlike fat mass, *sgk-1* completely phenocopies *rict-1* for life span and the short life span of *sgk-1* mutants is not enhanced in the *rict-1*;*sgk-1* double mutant.*rict-1* and *sgk-1* are thus in the same genetic pathway shortening life span when animals are fed OP50.

Figure 4.6: (continued)

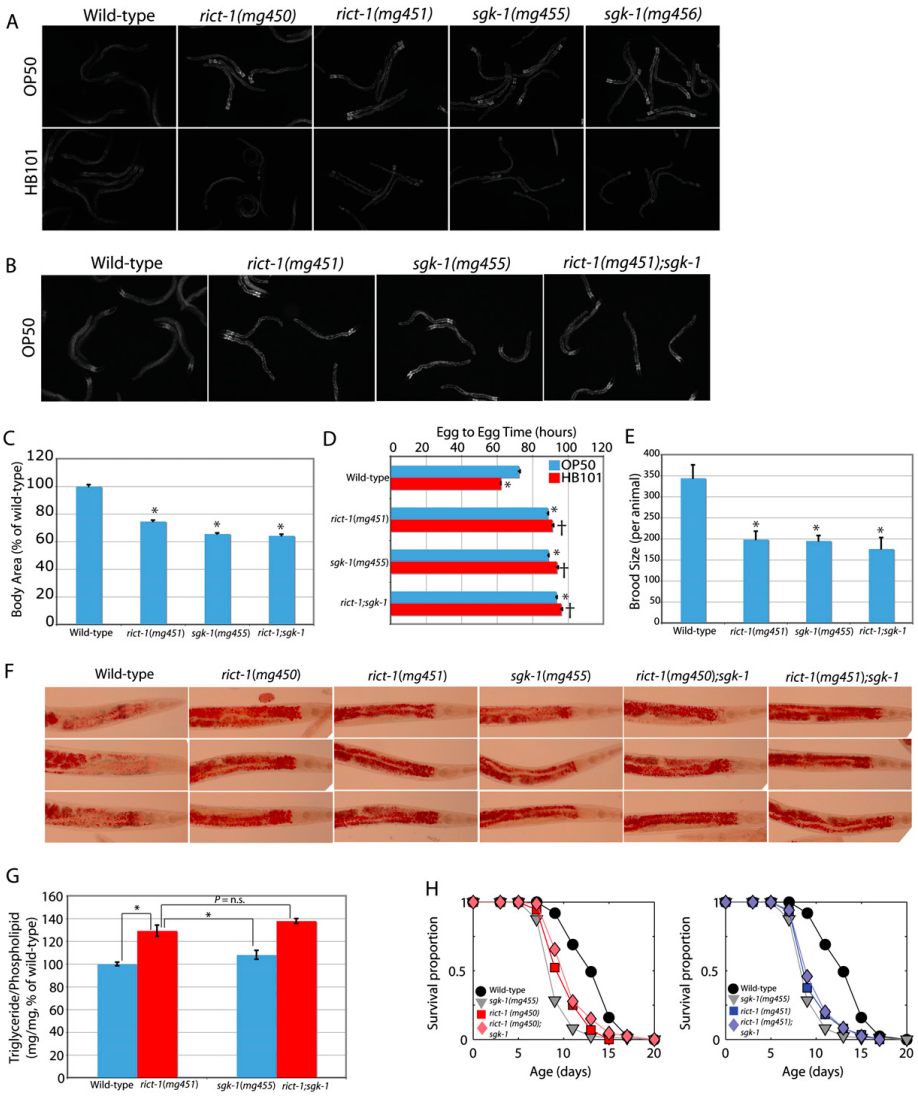

4.5.7 RICT-1/TORC2 regulates fat mass through AKT and SGK

To further examine the mechanism by which *rict-1* produces an increase in fat mass, we looked at fat mass in *akt-1* gain-of-function genetic mutants, in transgenic animals over-expressing wild-type *sgk-1* under its own promoter, and in transgenic animals expressing activated *sgk-1* [*sgk-1*(gf)] under the control of the *rict-1* promoter. For the latter, the same *rict-1* promoter was used that was able to rescue *rict-1* mutant life span and fat mass by driving *rict-1* cDNA because *sgk-1* would be predicted to act in the same cells as *rict-1* for the phenotype observed since TORC2 is an upstream kinase of *sgk-1* in cell lines (Garcia-Martinez and Alessi 2008). We found that rict1;*akt-1*(gf) double mutants partially suppressed the *rict-1*elevated fat mass as assessed by Oil-Red-O and quantitative lipid biochemistry (Figure 4.7A,B). Expression of activated *sgk-1*(gf) under the *rict-1* promoter only partially suppressed the high-fat phenotype of *rict-1*, as assessed with Nile red (Figure 4.7C). *rict-1*;*sgk-1*(gf) transgenic animals did not rescue body size (Figure 4.7D). Failure to rescue could be due to lack of appropriate expression of the transgene in necessary tissues, lack of sufficient expression level, or ailure of gain-of-function mutation of the HM threonine to aspartate to activate SGK-1 as has been demonstrated previously (Park et al. 1999). Surprisingly, however, high gene dosage of wild-type *sgk-1* under its own promoter was able to completely suppress Nile red fat mass of *rict-1* mutants, demonstrating that *sgk-1* can act downstream from *rict-1* to regulate fat (Figure 4.7C). This same rescuing transgene also completely rescued the high-fat phenotype of *sgk-1* mutants (Figure 4.7D). However, high gene dosage of wild-type *sgk-1* did not rescue the small body size of *rict-1* animals (but did rescue the small body size of *sgk-1* mutants), suggesting that functional TORC2 is necessary for growth regulation (Figure 4.7D) or that there are additional outputs of TORC2 that regulate body size. Finally, activation of the PI3 kinase cascade by a *daf-18* (PTEN homolog)-null mutation reduced fat mass in a wild-type background, but *rict-1*;*daf-18* double mutants still increased fat mass above *daf-18* single mutants by 33%, indicating regulation of fat mass in *rict-1* in parallel to PI3K (Figure 4.7A,B).

Figure 4.7 *(following page)*: Rescue of the *rict-1* mutant high-fat and growth phenotypes. (A,B) Oil-Red-O staining and quantitative lipid biochemistry indicate that *rict-1* high fat is partially suppressed by a chromosomally located akt-1 gain-of-function (gf) mutation. In contrast, while wild-type fat mass is decreased by a *daf-18*/PTEN inactivating mutation, *rict-1* still increases fat in a *daf-18* background, indicating that *rict-1* increases fat mass in parallel to PI3K signaling. (C,D) Neuron-specific transgene rescue of *rict-1* under the unc-119 promoter (*rict-1;Ex[unc-119pTRICT-1]*) fails to rescue the small body size or high-fat phenotype of *rict-1* mutants as assessed by Nile red. Transgenic expression of an activated *sgk-1* under the *rict-1* promoter partially rescues the small body size and high-fat phenotypes of *rict-1{rict-1;Ex[rict-1pTsgk-1(gf)]}*. In contrast, high gene dosage of wild-type *sgk-1* in *rict-1* mutants fully suppresses the high-fat phenotype but does not rescue the small body size (*rict-1;Ex[sgk-1TGFP]*). However, since this is very high copy overexpression, it does not mimic physiologic regulation of *sgk-1* or rule out that other genes play a role in the high-fat phenotype of *rict-1*. (*) $p < 10^{(} - 6)$ versus wild type; (†) $p < 10^{(} - 5)$ versus nonrescued mutant. (E,F) Intestine-specific transgene rescue of RICT-1 under either the *ifb-2* and *ges-1* promoters (*rict-1;Ex[ifb-2pTRICT-1*] and *rict-1;Ex[ges-1pTRICT-1*], respectively) fully rescues the small-body-size phenotype. The *ifb-2* promoter rescuing transgene completely rescues the high-fat phenotype of *rict-1*, whereas a partial rescue is seen in the case of the *ges*-1promoter-rescuing transgene. (*) $p < 10^{-6}$ versus wild type; (†) $P < 10^{-6}$ versus non-rescued mutant. (G) Mosaic analysis of a SGK-1 translational fusion with GFP, which allows expression to be followed visually, indicates that in intestinal cells expressing the SGK-1T GFP transgene, Nile red fat mass is reduced substantially, whereas in those cells lacking the transgene, Nile red fat mass is substantially higher. This suppression is seen in wild-type, *sgk-1*, and *rict-1* animals.

Figure 4.7: (continued)

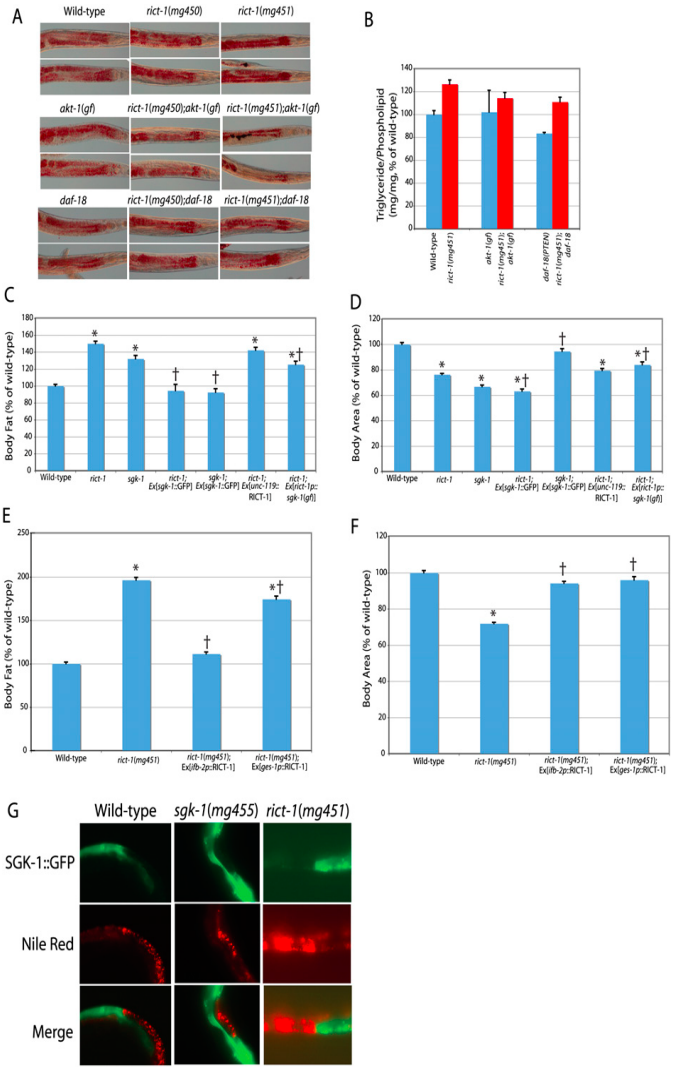

4.5.8 RICT-1 REGULATES FAT MASS AND WHOLE ORGANISM GROWTH VIA THE INTESTINE

The mechanism of action of *rict-1* was further dissected by tissue-specific rescue experiments in the two main sites of expression (Supplemental Figure 4.10B), the nervous system and the intestine, which are also known to play a key role in fat storage and life span (Wolkow et al. 2000; Ashrafi et al. 2003; Libina et al. 2003). Transgenic expression of *rict-1* in neurons did not rescue the high fat or growth defects of *rict-1* mutants (Figure 4.7C,D). Additionally, neuron-specific rescue failed to rescue normal life span in *rict-1* mutants (Supplemental Figure 4.15). Expression of *rict-1* in the intestine of *rict-1* mutants under two different intestine-specific promoters, the ges-1 promoter and the ifb-2 promoter, rescues the small-body size phenotype in transgenic progeny in the F1 generation (Figure 4.7F). Examination of *rict-1*;Ex[ifb-2pTRICT-1] F1 animals rescued for *rict-1* in the intestine also revealed normalization of Nile red fat mass (Figure 4.7E). Examination of the Nile red phenotype of transgenic *rict-1*;Ex[ges1pTRICT-1] rescued for body size indicated on average a 12%, significant reduction in fat mass for the whole population (Figure 4.7E). This was an incomplete rescue because only ;20% of size-rescued mutants showed wild-type Nile red fat levels. We were unable to obtain a sufficient number of transmitting lines of *rict-1* mutants expressing *rict-1* in the intestine; this may be due to *rict-1* gene dosage or to imbalances between tissues in *rict-1* signaling. (In the single transgenic line obtained carrying an intestine-specific rescue construct, neither body size, nor Nile red fat mass, nor life span was rescued [Supplemental Figure 4.15], perhaps due to insufficient *rict-1* gene dosage to rescue.)

We also examined animals mosaic for *sgk-1* over-expression in the intestine. These studies indicated that *sgk-1* suppresses Nile red fat mass in the intestine in a cellautonomous manner (Figure 4.7G). In wild-type, *sgk-1*(mg455), and *rict-1*(*mg451*) mutants, an extrachromosomal transgene over-expressing an SGK-1TGFP translational fusion suppressed Nile red fat mass in the intestine (Figure 4.7G). In the surrounding intestinal cells lacking the SGK-1TGFP fusion protein, Nile red fat mass was higher than in transgene-containing intestinal cells. Since

fat mass is also suppressed in wild-type worms by over-expression of SGK-1, these data do not allow the conclusion that *sgk-1* is the sole output of TORC2-regulating fat mass. These data in aggregate suggest that *sgk-1* acts directly within intestinal cells, the same site of *rict-1* action, likely downstream from TORC2 to regulate fat mass.

4.6 Discussion

The data presented here highlight a new role for Rictor/ TORC2 in energy metabolism, feeding behavior, life-span modulation, growth, and reproduction. We suggest that *rict-1* acts as a critical sensor of organismal energetic status and is a master regulator of metabolic processes such as growth, energy storage, reproduction, and maintenance of life span. When this process is disabled, the organism is no longer able to appropriately channel calories into essential metabolic processes and inappropriately activates long-term energy storage in the form of triglycerides. These data also show that the site of action of *rict-1* in regulating growth and fat mass is the intestine, which is the key site of fat storage in *C. elegans* (Ashrafi et al. 2003; Mak et al. 2006). Given the evolutionary conservation of Rictor, components of the TORC2 complex, AKT and SGK, these results suggest that these genes may be involved in fat storage and life span across phylogeny.

4.6.1 RICT-1 acts through SGK-1 to regulate life span, growth, reproduction, and both SGK-1 and AKT to regulate fat mass

Many phenotypes in *rict-1* mutants are shared by the AGC kinase *sgk-1*, the sole *C. elegans* homolog of the serum and glucocorticoid-induced kinase gene family. While the life-span, growth, and reproductive phenotypes of *rict-1* mutants can be explained by *sgk-1*, the full extent of excess triglyceride accumulation is dependent on the akt kinases in addition to *sgk-1*. Even though fat mass in *rict-1* mutants as assessed by Nile red can be suppressed by over-expression of wild-type SGK-1, based on loss-of-function data, it is unlikely that *sgk-1* is the only output of TORC2 affecting fat mass. Furthermore, it is difficult to say whether SGK-1 is the only downstream effector of TORC2 for fat mass because over-expression of SGK-1 suppresses fat mass in wild-type worms. Additionally, a chromosomally located gain-of-function mutation in *akt-1* (Paradis and Ruvkun 1998) partially

suppresses *rict-1* fat mass as assessed biochemically and by Oil-RedO, implying that TORC2 signals to regulate fat both through SGK and AKT. Thus, a model is proposed whereby RICT-1/TORC2 modulates fat mass, aging, brood delivery, and growth through both SGK and AKT (Supplemental Figure 4.16).

There are emerging data to suggest that SGK is an important, downstream effector of TORC2 in yeast and in mammals (Kamada et al. 2005; Aronova et al. 2008; Garcia-Martinez and Alessi 2008). The SGK family has been extensively implicated in sodium and potassium homeostasis in mammals (Lang and Cohen 2001; Lang et al. 2006). In mice and in humans, SGK1 and SGK3 have been linked to glucose homeostasis, salt balance, and blood pressure, and the SGK3 knockout mouse has a subtle, transient growth defect (Busjahn et al. 2002; McCormick et al. 2004). The SGK1 knockout mouse has no life-span phenotype (Lang et al. 2006). Our data show that SGK is a critical metabolic output of TORC2 in regulating growth and metabolism. It remains to be shown whether mammalian SGK1, SGK2, or SGK3 share these roles. It is possible that SGK2 plays this role, the knockout for which has not yet been reported, or that functional redundancy in the SGK isoforms in mammals prevents development of growth phenotypes in SGK1 and SGK3 knockouts and SGK1 and SGK3 double knockout mice.

4.6.2 RICT-1 and SGK-1 modulate life span in a nutrient-dependent manner

Based on the results we present here in *rict-1* mutants and in *rict-1*;*sgk-1* double mutants, we conclude that the defects evident in *sgk-1* mutants are due to failure to activate the HM by TORC2 phosphorylation. Null, deletion mutations in *C. elegans sgk-1(ok538)* had beeok583n previously reported to show defects in growth, reproduction, and life span (Hertweck et al. 2004). Our loss-offunction allele *sgk-1*(mg455) shares all the defects in brood size, growth rate, and body size evident in the deletion allele. However, we observed a shortened life span in *sgk-1* mutants that was identical to and not enhanced by *rict-1* loss of function when animals were fed OP50. This is in contrast to previously published lifespan analysis demonstrating dramatic life-span extension in *sgk-1* knockdown by RNAi (Hertweck et al. 2004). In contrast to our studies, these previous studies were done without fluorodeoxyuridine (to inhibit progeny production) and by RNAi against

sgk-1 (not the genetic mutant) using the E. coli strain HT115. These studies used RNAi because the genetic mutant life-span analysis was not possible without fluorodeoxyuridine due to an egg-laying defect and causing progeny to hatch within the parent (bag of worms phenotype). We also could not assess the life span of *sgk-1*(mg455) or *rict-1* mutants without FUDR due to a highly penetrant bag of worms phenotype. Here, using genetic mutants and fluorodeoxyuridine, we demonstrate that *rict-1* animals and *sgk-1* animals are short-lived when fed the standard laboratory diet, E. coli OP50. We also showed that when *rict-1* animals are fed either E. coli HB101 or HT115, they shift from being short-lived to being long-lived and consume less bacteria than wild type. Finally, RNAi of *rict-1* in our hands under the conditions reported previously (i.e. without FUDR on HT115) also leads to life-span extension (data not shown). Thus, we conclude that rather than strictly extending or shortening life span, *rict-1* and likely also *sgk-1* modulate life span by affecting feeding and metabolism on different diets.

Feeding behavior is modulated by *rict-1* such that mutants feed paradoxically on diets of different nutritional value. Our observations suggest that *rict-1* mutants feed more robustly on E. coli OP50 and consume less E. coli HB101 by residing less on the lawn of bacteria. This behavior is not observed for wild-type worms, which rarely leave a lawn of HB101. Thus, *rict-1* participates in the genetic pathway that regulates feeding behavior in response to foods of different quality. It remains to be shown what signal from the diet is sensed either directly or indirectly by RICT-1/TORC2 and how this modulates feeding behavior. There is a strong precedent for TOR complex 1 to be nutrientand growth factor-regulated (Sarbassov et al. 2005a; Bhaskar and Hay 2007; Sancak et al. 2008). In cell lines and MEFs, TORC2-mediated phosphorylation of the HM of AKT is insulin-sensitive (Hresko and Mueckler 2005; Guertin et al. 2006), but TORC2 itself is not known to directly sense nutrients. It remains to be seen whether the normal response of *C. elegans* to different diets depends on direct nutrient-dependent Rictor/TORC2 modulation versus descending input to Rictor/TORC2 from other signaling pathways. However, our data indicate that *rict-1* and *sgk-1* are critical links between food and metabolic outputs, including feeding behavior, fat mass, growth, reproduction, and life span.

4.6.3 Fixative-based fat staining differs from labeling with BODIPY-labeled fatty acids in the case of the insulin-like signaling pathway mutants

A protocol to stain neutral lipid using the dye Oil-Red-O was developed in order to bypass the need for animals to uptake or accumulate vital dyes or fluorescently labeled fatty acids to indicate fat mass. While for the case of the *rict-1* mutant, an increase in BODIPY and Nile red agreed with the increase in Oil-Red-O staining, in the case of insulin-like signaling mutants, particularly *daf-2* and *akt-1*, BODIPY staining was not representative of triglyceride mass as assessed by Oil-Red-O or quantitative lipid biochemistry. This indicates, in some (and likely the minority of) cases, that Nile red or BODIPY fat mass may not be indicative of the true lipid stores within the animal. We do not yet know why the vital dyes or BODIPY behave differently in insulin-like signaling mutants than they do in most other animals, but one possible explanation is that there is decreased dye absorption via the hypodermis or the intestine, as insulin signaling pathway mutants have a decreased gut surface area (Albert and Riddle 1988; Hu 2007).

4.6.4 Genetic pathways upstream of and downstream from RICT-1/TORC2

Our results indicate that RICT-1 and the AGC kinases AKT-1, AKT-2, and SGK-1 participate in a pathway regulating fat metabolism, feeding, growth, reproduction, and life span. However, based on the data, the upstream inputs and downstream effectors of *rict-1*, akt, and *sgk-1* are not known. In mammals and in *C. elegans*, it has been shown previously that SGK-1 could be activated by PI3K signaling through the upstream kinase PDK-1, much like AKT (Park et al. 1999; Lang and Cohen 2001; Hertweck et al. 2004). It is likely that PI3K/PDK-mediated activation of AKT and SGK regulate fat differently from proposed HM phosphorylation of these kinases by TORC2. Furthermore, here we demonstrate that activation of canonical PI3K signaling by genetic inactivation of *daf-18* (PTEN) regulates fat mass in parallel to *rict-1*/TORC2. Thus, rict1 does not appear to be downstream from *daf-18* (PTEN) or the sole insulin-like receptor *daf-2* in its regulation of fat mass. Thus, we suggest that pathways other than insulin-like or PIP3 signaling are upstream of *rict-1* for fat regulation. For *rict-1* life-span regulation, insulin-like

signaling through *akt-1* is required for the short life span. However, *rict-1* short life span is modulated by *akt-1* and not strictly caused by alterations in insulin-like or akt signaling (Supplemental Figure 4.16). Thus, for *rict-1* modulation of life span, the upstream signals also remain unclear.

In *C. elegans*, the only genetically and biochemically defined target of the AKT and SGK kinases had been the FOXO transcription factor DAF-16 (Hertweck et al. 2004). More recently, AKT-1, AKT-2, and SGK-1 have been shown to phosphorylate the transcription factor SKN-1 (Tullet et al. 2008). From our analysis of life span and of fat mass, the phenotypes of *rict-1* animals are not mediated by *daf-16*, while interactions of *rict-1* with *skn-1* have yet to be explored in more detail. Thus, other than *daf-16*, additional downstream targets of AKT and SGK must be responsible for mediating *rict-1* phenotypes. Along these lines, in mammals, AKT and SGK phosphorylate several targets in addition to the *daf-16* homolog FOXO3a (Brunet et al. 2001; Lang et al. 2006). Finally, TORC2 also phosphorylates the protein kinase C family (Sarbassov et al. 2004; Guertin et al. 2006; Facchinetti et al. 2008). We have just begun to understand the role of *rict-1* and *sgk-1* in metabolic regulation in *C. elegans*, and further work is needed to elucidate the upstream and downstream signaling molecules. Overall, these observations indicate that TORC2 regulates metabolism, feeding, growth, and reproduction, and modulates life span in *C. elegans*. The dominant site of TORC2 and *sgk-1* action is the intestine, and the role of these kinases in other tissues remains to be more fully explored. Since the intestine is the major site of fat storage and is an endocrine organ regulating life span (Libina et al. 2003), it is not surprising that signals generated within the intestine could have such pleiotropic effects in *C. elegans*. Given the evolutionary conservation of Rictor, the components of TORC2, and the SGK family of kinases, it will be interesting to see if conditional, tissue-specific inactivation of *rictor*, sgk isoforms, or other TORC2 components in mice produces alterations in body fat, growth, and life span, or protects them from obesity induced

by nutrient-rich food, as do *rict-1* mutations in *C. elegans*.

4.7 Materials and Methods, Supplemental Figures

4.7.1 Strains used

N2 Bristol was used as the wild-type strain. The following mutant strains were used: *daf-2*(e1370), *daf-16*(mgDf47), *akt-1*(mg306), *akt-2*(*ok393*), *daf-18*(*mg198*), *skn-1*(zu169). For tissue distribution of *rict-1*, *mgEx744*, *mg744*: *Ex[F29C12.3pTmRFP;myo2pTGFP]*, 1.4 kb of upstream *rict-1* promoter sequence was used. For rescue experiments, *mgEx747*: *Ex[F29C12.3pTRICT-1 cDNATSL2TGFP; myo-2pTmCherry]*. For neuronal rescue, *mgEx754: Ex[unc119pTRICT-1 cDNATSL2TGFP; myo-2pTGFP]*, 2.2 kb of upstream promoter was used. For intestinal rescue, *Ex[ges1pTRICT-1TSL2TGFP;myo-2pTGFP]*, 2.1 kb of upstream promoter was used. For *Ex[ifb-2pTRICT-1TSL2TGFP;myo-2pTGFP]*, 3 kb of upstream promoter was used. For *sgk-1* gain of function, *mgEx757[rict-1pTSGK-1(D453TK) cDNATSL2TGFP;myo-2pTGFP]*. For *sgk-1* rescue, BR2773(byEx[*sgk-1*TGFP]) (Hertweck et al. 2004) was crossed into *rict-1*(*mg451*) and *sgk-1*(mg455). *rict-1* cDNA was amplified obtaining a dominant PCR product from wildtype worms and cloned, and several clones were sequenced to confirm the intact reading frame (Supplemental Figure 4.8). Isolation of *rict-1*(F29C12.3) and *sgk-1* mutants *C. elegans* N2 Bristol strain was mutagenized with EMS, and the resultant F2 generation was screened for increased staining with the vital dye Nile red (Ashrafi et al. 2003; Mak et al. 2006). Individual isolates were back-crossed to N2 Bristol and positionally cloned based on polymorphisms between N2 and the multiply polymorphic *C. elegans* strain CB4586.

4.7.2 Body fat assessment

Body fat analysis was conducted as described previously (Mak et al. 2006). Briefly, wild-type or mutant *C. elegans* was seeded on NGM plates containing either E. coli OP50 or HB101 supplemented with 1 mM the fluorescent fatty acid analog C1-BODIPY 500/510-C12 (Invitrogen) or Nile red (Invitrogen) from a 2-h synchronous egg lay or as L1 following overnight hatching and synchronization at 20¡C in minimal media. Imaging and quantitation was conducted after growth at 20¡C as day 3 adults (Figs. 1, 3B) or day 1-2 adults (Figure 4.3A) using an Axioplan microscope and Axiovision software (Zeiss). At least 30 animals were imaged on at least three separate occasions, and results were consistent between experiments. The vital dye Nile red (Invitrogen) was used to confirm phenotypes of *rict-1*(*mg450*) and *rict-1*(*mg451*) observed by BODIPY staining, as described (Mak et al. 2006). All body fat analyses were carried out on animals grown at 20¡C. Oil-Red-O staining was conducted by washing 200-300 day 1 adult animals from plates synchronized at the time of the first progeny hatching (12 h after the first egg is laid). The worms were resuspended and washed twice with PBS and then suspended in 120 mL of PBS to which an equal volume of 23 MRWB buffer containing 2% paraformaldehyde was added (composition: 160 mM KCl, 40 mM NaCl, 14 mM Na2EGTA, 1 mM Spermidine HCl, 0.4 mM Spermine, 30 mM Na PIPES at pH 7.4, 0.2% BME). The worms were taken through three freeze-thaw cycles between dry-ice/ethanol and warm running tap water, followed by spinning at 14,000g, washing once in PBS to remove PFA, resuspension in 60% isopropanol to dehydrate, and addition of 60% Oil-Red-O stain (prepared as follows: from 0.5 g/100 mL isopropanol stock solution equilibrated for several days, freshly dilute with 40% water, 60% stock, and allow to sit 10 min and filter 0.2 to 0.4 mm). Oil-Red-O analysis in mosaic animals could not be completed due to the disappearance of GFP with the fixation necessary to complete Oil-Red-O staining. Although it is possible to quantitate the amount of Oil-Red-O staining in individual animals, for the purposes of this study we relied on quantitative lipid biochemistry and not Oil-Red-O quantitation to determine the amount of stored triglyceride in a given genotype. When quantitated, Oil-Red-O correlated well with triglyceride mass determined by quantitative lipid biochemistry (data not shown). Quantitative lipid biochemistry was conducted as published previously (Perez and Van Gilst 2008) with the

following modifications: Briefly, 7500 worms at day 1 of adulthood were washed from three 10-cm plates containing the indicated food, and washed over a 20-mm mesh (Small Parts, Inc.) with an excess of S-Basal medium to remove progeny, eggs, and bacteria. These were allowed to sit on an empty plate for 20 min to empty bacteria from the gut. Afterward, worms were re-harvested and frozen on liquid nitrogen. The total worm pellet was sonicated in 0.25 mL of PBS, after which we added 50 mL of triglyceride and phospholipids standards dissolved in chloroform:methanol 2:1 (16.7 nmol of tritridecanoin, Nu-Chek Prep, and 25 nmol of 1,2diheptadecanoyl-sn-glycero-3-phosphocholine, Matreya, respectively), and immediately added to 1.5 mL of 2:1 chloroform:methanol to extract lipids. This mixture was spun down (1000g for 1 min), and the lower organic phase was recovered without debris. This was washed with 3 mL of 0.9% NaCl and spun at 1000g to separate phases. The lower organic phase was evaporated under nitrogen, and lipids were resuspended in 100% chloroform to conduct solid-phase chromatography using prepacked silica gel columns (Thermo Scientific) followed by GCMS as reported previously (Perez and Van Gilst 2008). For all measurements, at least two biological replicates were performed, with data shown as mean 6 SEM. Where a minimum of four measurements were conducted, statistical analysis was carried out using pairwise Student's t-tests.

4.7.3 Pharyngeal pumping rates

Pumping rate was determined using a Sony camera attached to a Zeiss microscope for between 10 and 12 synchronized, well-fed day 1 adult animals per genotype grown on the same food that pumping assays were determined on. Pharyngeal contractions in 20to 30-sec time periods were counted using iMovie (Apple), and pumping rates per minute were calculated.

4.7.4 Oxygen consumption

Synchronized, day 1 adult worms grown on either OP50 or HB101 were washed repeatedly over a 35-mm nylon mesh (Small Parts, Inc., for wild type) or a 20-mm nylon mesh (for *rict-1* mutants) to remove bacteria, eggs, and larvae. Oxygen consumption of 2500 worms was then measured immediately in 1.5 mL of S-basal medium without cholesterol using a Strathkelvin 928 6-channel Clark electrode

respirometer. Six to 10 independent measurements were conducted and averaged per strain, per food source and normalized to total protein content, determined using a BCA assay (Pierce).

4.7.5 Brood size determination

Ten to 12 synchronized animals per strain, per food source were transferred daily to fresh NGM plates containing OP50 or HB101, and hatched progeny were counted 3 d later. Total brood size was determined by adding progeny produced across all days.

4.7.6 Body size determination

Maximal, longitudinal cross-sectional area was obtained by quantitative microscopy using Zeiss axiovision software at identical time points that images were taken for fat mass determination.

4.7.7 Egg-to-egg time

Eggs were synchronized by 2 h synchronous egg lay. At the L4 stage, 20 animals per strain per food source were placed on an individual plate and monitored every 1-2 h until the first egg was laid. The data were expressed as the mean time until first egg laid 6SEM.

4.7.8 Feeding RNAi

RNAi clones were isolated from a genome-wide E. coli feeding RNAi library and fed to *C. elegans* as described previously (Kamath and Ahringer 2003; Kamath et al. 2003). *E. coli* clones expressing dsRNA corresponding to control vector L4440, *rict-1*, or *sinh-1* were supplemented with C1-BODIPY 500/510 C12 or Nile red, to determine fat content as above, or put on un-supplemented plates for Oil-Red-O staining. Synchronous populations of worms were obtained by bleach treatment of gravid adults, and after one generation of RNAi feeding, animals were examined and imaged as 2-d adults for fat content.

4.7.9 Longevity assay

Animals from the parental generation were grown on the same food source that life span was conducted on. Synchronous animals were obtained by bleach treatment of gravid adults and seeded onto NGM OP50 or HB101 plates. As day 1 adults, 30 animals per genotype were transferred in triplicate (90 total) to fresh NGM OP50 or HB101 plates supplemented with 100 mM 5-fluorodeoxyuridine (FUDR) solution to suppress progeny production. Three independent assays were carried out using strains on different diets: (1) OP50 diet only, (2) OP50 or HB101, and (3) OP50, HB101, or HT115 diets. *daf-2*(e1370), *daf-16* (mgDf47), *akt-1* (mg306), *akt-1*(mg144gf), *akt-2* (*ok393*), and *sgk-1*(mg455) epistasis analysis was carried out in triplicate using strains grown on OP50. *skn-1*(zu169) epistasis was carried out in triplicate on OP50 and HB101. All life-span analyses reported were conducted at 25¡C.

4.7.10 Gompertz-Makeham survival analysis

Prior to analysis, data were pooled across independent experiments to give unbiased estimates of survival at each assayed age. The Gompertz-Makeham model for age-specific mortality $M = M_0 exp(Gx) + M_\infty$, with initial mortality M_0, rate of aging G, age x, and age-independent mortality M_∞, can be shown to give the survival proportion $S(x) = exp[(M_0/G)(1 - exp(Gx) - M_\infty x)]$. We performed population-weighted nonlinear least-squares Gompertz model fits using a Trust-Region Reflective Newton algorithm implemented by the MATLAB *fit()* function (The MathWorks). Median and maximum life span were calculated from each fit as the age of 50% and 25% estimated survival, respectively.

4.8 Acknowledgements

We thank Sean Curran, Eyleen O'Rourke, Susana Garcia, Meng Wang, Chi Zhang, and Buck Samuel for creative input, sharing materials, and reading of the manuscript. Thanks to Eyleen O'Rourke for help in developing Oil-Red-O staining and methods for quantitative lipid biochemistry. Thanks to Joseph Avruch for critical reading of the manuscript and help with interpretation of the data. We are indebted to Mason Freeman for the use of his GCMS for lipid anal-

ysis. We also thank members of the Kaplan and Ausubel laboratories for creative exchanges, and Diane Sacchetti for administrative assistance. Thank you to Kaveh Ashrafi and Kevin Jones for sharing their findings on Rictor with us. Thanks to the Caenorhabditis Genome Center and Ralf Baumeister for providing strains, and the *C. elegans* Knockout Consortium for generating ok alleles. This work was supported by Award numbers R01DK070147 (to G.R.) and F32DK080607 (to A.S.) from the National Institute of Diabetes and Digestive and Kidney Diseases.

4.9 Author contributions

AS and EK designed experiments, conducted experiments, analyzed data, assembled figures and wrote the paper. CC analyzed data. JM conducted experiments. GR supervised the project.

4.10 References

1. Albert, P.S. and Riddle, D.L. 1988. Mutants of *Caneorhabditis elegans* that form dauer-like larvae. Dev. Biol. 126: 270-293.

2. Aronova, S., Wedaman, K., Aronov, P.A., Fontes, K., Ramos, K., Hammock, B.D., and Powers, T. 2008. Regulation of ceramide biosynthesis by TOR complex 2. Cell Metab. 7: 148-158.

3. Ashrafi, K., Chang, F.Y., Watts, J.L., Fraser, A.G., Kamath, R.S., Ahringer, J., and Ruvkun, G. 2003. Genome-wide RNAi analysis of *Caneorhabditis elegans* fat regulatory genes. Nature 421: 268-272.

4. Avery, L. and Shtonda, B.B. 2003. Food transport in the *C. elegans* pharynx. J. Exp. Biol. 206: 2441-2457.

5. Bentzinger, C.F., Romanino, K., Cloetta, D., Lin, S., Mascarenhas, J.B., Oliveri, F., Xia, J., Casanova, E., Costa, C.F., Brink, M., et al. 2008. Skeletal muscle-specific ablation of raptor, but not of *rictor*, causes metabolic changes and results in muscle dystrophy. Cell Metab. 8: 411-424.

6. Bhaskar, P.T. and Hay, N. 2007. The two TORCs and Akt. Dev. Cell 12: 487-502.

7. Bishop, N.A. and Guarente, L. 2007. Two neurons mediate diet-restriction-induced longevity in *C. elegans*. Nature 447: 545-549.

8. Brunet, A., Park, J., Tran, H., Hu, L.S., Hemmings, B.A., and Greenberg, M.E. 2001. Protein kinase SGK mediates survival signals by phosphorylating the forkhead transcription factor FKHRL1 (FOXO3a). Mol. Cell. Biol. 21: 952-965.

9. Busjahn, A., Aydin, A., Uhlmann, R., Krasko, C., Bahring, S., Szelestei, T., Feng, Y., Dahm, S., Sharma, A.M., Luft, F.C., et al. 2002. Serumand glucocorticoid-regulated kinase (SGK1) gene and blood pressure. Hypertension 40: 256-260.

10. Facchinetti, V., Ouyang, W., Wei, H., Soto, N., Lazorchak, A., Gould, C., Lowry, C., Newton, A.C., Mao, Y., Miao, R.Q., et al. 2008. The mammalian target of rapamycin complex 2 controls folding and stability of Akt and protein kinase C. EMBO J. 27: 1932-1943.

11. Finch, C.E. and Ruvkun, G. 2001. The genetics of aging. Annu. Rev. Genomics Hum. Genet. 2: 435-462.

12. Frias, M.A., Thoreen, C.C., Jaffe, J.D., Schroder, W., Sculley, T., Carr, S.A., and Sabatini, D.M. 2006. *mSin1* is necessary for Akt/PKB phosphorylation, and its isoforms define three distinct mTORC2s. Curr. Biol. 16: 1865-1870.

13. Garcia-Martinez, J.M. and Alessi, D.R. 2008. mTOR complex 2 (mTORC2) controls hydrophobic motif phosphorylation and activation of serumand glucocorticoid-induced protein kinase 1 (SGK1). Biochem. J. 416: 375-385.

14. Guertin, D.A., Stevens, D.M., Thoreen, C.C., Burds, A.A., Kalaany, N.Y., Moffat, J., Brown, M., Fitzgerald, K.J., and Sabatini, D.M. 2006. Ablation in mice of the mTORC components raptor, *rictor*, or mLST8 reveals that mTORC2 is required for signaling to Akt-FOXO and PKCa, but not S6K1. Dev. Cell 11: 859-871.

15. Hertweck, M., Gobel, C., and Baumeister, R. 2004. *C. elegans* SGK-1 is the critical component in the Akt/PKB kinase complex to control stress response and life span. Dev. Cell 6: 577-588.

16. Hresko, R.C. and Mueckler, M. 2005. mTOR.RICTOR is the Ser473 kinase for Akt/protein kinase B in 3T3-L1 adipocytes. J. Biol. Chem. 280: 40406-40416.

17. Hu P.J. 2007. Dauer. In WormBook (ed. The *C. elegans* Research Community), WormBook. doi: 10.1895/wormbook.1.144.1 http://www.wormbook.org.

18. Jia, K., Chen, D., and Riddle, D.L. 2004. The TOR pathway interacts with the insulin signaling pathway to regulate C. elegans larval development, metabolism and life span. Development 131: 3897-3906.

19. Kamada, Y., Fujioka, Y., Suzuki, N.N., Inagaki, F., Wullschleger,S., Loewith, R., Hall, M.N., and Ohsumi, Y. 2005. Tor2 directly phosphorylates the AGC kinase Ypk2 to regulate actin polarization. Mol. Cell. Biol. 25: 7239-7248.

20. Kamath, R.S. and Ahringer, J. 2003. Genome-wide RNAi screening in Caenorhabditis elegans. Methods 30: 313-321.

21. Kamath, R.S., Fraser, A.G., Dong, Y., Poulin, G., Durbin, R., Gotta, M., Kanapin, A., Le Bot, N., Moreno, S., Sohrmann, M., et al. 2003. Systematic functional analysis of the Caenorhabditis elegans genome using RNAi. Nature 421: 231-237.

22. Kimura, K.D., Tissenbaum, H.A., Liu, Y., and Ruvkun, G. 1997. daf-2, an insulin receptor-like gene that regulates longevity and diapause in Caenorhabditis elegans. Science 277: 942-946.

23. Kumar, A., Harris, T.E., Keller, S.R., Choi, K.M., Magnuson, M.A., and Lawrence, Jr., J.C. 2008. Muscle-specific deletion of rictor impairs insulin-stimulated glucose transport and enhances basal glycogen synthase activity. Mol. Cell. Biol. 28: 61-70.

24. Lang, F. and Cohen, P. 2001. Regulation and physiological roles of serum- and glucocorticoid-induced protein kinase isoforms. Sci. STKE 2001: RE17. doi:10.1126/stke.2001.108.re17.

25. Lang, F., Bohmer, C., Palmada, M., Seebohm, G., Strutz-Seebohm, N., and Vallon, V. 2006. (Patho)physiological significance of the serum- and glucocorticoid-inducible kinase isoforms. Physiol. Rev. 86: 1151-1178.

26. Lee, G. and Chung, J. 2007. Discrete functions of rictor and raptor in cell growth regulation in Drosophila. Biochem. Biophys. Res. Commun. 357: 1154-1159.

27. Libina, N., Berman, J.R., and Kenyon, C. 2003. Tissue-specific activities of C. elegans DAF-16 in the regulation of lifespan. Cell 115: 489-502.

28. Long, X., Spycher, C., Han, Z.S., Rose, A.M., Muller, F., and Avruch, J. 2002. TOR deficiency in C. elegans causes developmental arrest and intestinal atrophy by inhibition of mRNA translation. Curr. Biol. 12: 1448-1461.

29. Long, X., Muller, F., and Avruch, J. 2004. TOR action in mammalian cells and in Caenorhabditis elegans. Curr. Top. Microbiol. Immunol. 279: 115-138.

30. Mak, H.Y., Nelson, L.S., Basson, M., Johnson, C.D., and Ruvkun, G. 2006. Polygenic control of Caenorhabditis elegans fat storage. Nat. Genet. 38: 363-368.

31. McCormick, J.A., Feng, Y., Dawson, K., Behne, M.J., Yu, B., Wang, J., Wyatt, A.W., Henke, G., Grahammer, F., Mauro, T.M., et al. 2004. Targeted disruption of the protein kinase SGK3/CISK impairs postnatal hair follicle development. Mol. Biol. Cell 15: 4278-4288.

32. Meissner, B., Boll, M., Daniel, H., and Baumeister, R. 2004. Deletion of the intestinal peptide transporter affects insulin and TOR signaling in Caenorhabditis elegans. J. Biol. Chem. 279: 36739-36745.

33. Morris, J.Z., Tissenbaum, H.A., and Ruvkun, G. 1996. A phosphatidylinositol-3-OH kinase family member regulating longevityand diapause in Caenorhabditis elegans. Nature 382: 536-539.

34. Ogg, S. and Ruvkun, G. 1998. The C. elegans PTEN homolog, DAF-18, acts in the insulin receptor-like metabolic signaling pathway. Mol. Cell 2: 887-893.

35. Ogg, S., Paradis, S., Gottlieb, S., Patterson, G.I., Lee, L., Tissenbaum, H.A., and Ruvkun, G. 1997. The Fork head transcription factor DAF-16 trans-

duces insulin-like metabolic and longevity signals in C. elegans. Nature 389: 994-999.

36. Paradis, S. and Ruvkun, G. 1998. Caenorhabditis elegans Akt/PKB transduces insulin receptor-like signals from AGE-1 PI3 kinase to the DAF-16 transcription factor. Genes Dev. 12: 2488-2498.

37. Paradis, S., Ailion, M., Toker, A., Thomas, J.H., and Ruvkun, G. 1999. A PDK1 homolog is necessary and sufficient to transduce AGE-1 PI3 kinase signals that regulate diapause in Caenorhabditis elegans. Genes Dev. 13: 1438-1452.

38. Park, J., Leong, M.L., Buse, P., Maiyar, A.C., Firestone, G.L., and Hemmings, B.A. 1999. Serum and glucocorticoid-inducible kinase (SGK) is a target of the PI 3-kinase-stimulated signaling pathway. EMBO J. 18: 3024-3033.

39. Pearce, L.R., Huang, X., Boudeau, J., Pawlowski, R., Wullschleger, S., Deak, M., Ibrahim, A.F., Gourlay, R., Magnuson, M.A., and Alessi, D.R. 2007. Identification of Protor as a novel Rictorbinding component of mTOR complex-2. Biochem. J. 405: 513-522.

40. Perez, C.L. and Van Gilst, M.R. 2008. A 13C isotope labeling strategy reveals the influence of insulin signaling on lipogenesis in C. elegans. Cell Metab. 8: 266-274.

41. Porte Jr., D. Baskin, D.G., and Schwartz, M.W. 2005. Insulin signaling in the central nervous system: A critical role in metabolic homeostasis and disease from C. elegans to humans. Diabetes 54: 1264-1276.

42. Sancak, Y., Peterson, T.R., Shaul, Y.D., Lindquist, R.A., Thoreen, C.C., Bar-Peled, L., and Sabatini, D.M. 2008. The Rag GTPases bind raptor and mediate amino acid signaling to mTORC1. Science 320: 1496-1501.

43. Sarbassov, D.D., Ali, S.M., Kim, D.H., Guertin, D.A., Latek, R.R., Erdjument-Bromage, H., Tempst, P., and Sabatini, D.M. 2004. Rictor, a novel binding partner of mTOR, defines a rapamycin-insensitive and raptor-independent pathway that regulates the cytoskeleton. Curr. Biol. 14: 1296-1302.

44. Sarbassov, D.D., Ali, S.M., and Sabatini, D.M. 2005a. Growing roles for the mTOR pathway. Curr. Opin. Cell Biol. 17: 596-603.

45. Sarbassov, D.D., Guertin, D.A., Ali, S.M., and Sabatini, D.M. 2005b. Phosphorylation and regulation of Akt/PKB by the rictor-mTOR complex. Science 307: 1098-1101.

46. Schmidt, A., Kunz, J., and Hall, M.N. 1996. TOR2 is required for organization of the actin cytoskeleton in yeast. Proc. Natl. Acad. Sci. 93: 13780-13785.

47. Shiota, C., Woo, J.T., Lindner, J., Shelton, K.D., and Magnuson, M.A. 2006. Multiallelic disruption of the rictor gene in mice reveals that mTOR complex 2 is essential for fetal growth and viability. Dev. Cell 11: 583-589.

48. Shtonda, B.B. and Avery, L. 2006. Dietary choice behavior in Caenorhabditis elegans. J. Exp. Biol. 209: 89-102.

49. Soukas,A., Socci, N.D., Saatkamp, B.D.,Novelli, S., and Friedman, J.M. 2001. Distinct transcriptional profiles of adipogenesis in vivo and in vitro. J. Biol. Chem. 276: 34167-34174.

50. Tabuchi, M., Audhya, A., Parsons, A.B., Boone, C., and Emr, S.D. 2006. The phosphatidylinositol 4,5-biphosphate and TORC2 binding proteins Slm1 and Slm2 function in sphingolipid regulation. Mol. Cell. Biol. 26: 5861-5875.

51. Tullet, J.M., Hertweck, M., An, J.H., Baker, J., Hwang, J.Y., Liu, S., Oliveira, R.P., Baumeister, R., and Blackwell, T.K. 2008. Direct inhibition of the longevity-promoting factor SKN-1 by insulin-like signaling in C. elegans. Cell 132: 1025-1038.

52. Vellai, T., Takacs-Vellai, K., Zhang, Y., Kovacs, A.L., Orosz, L., and Muller, F. 2003. Genetics: Influence of TOR kinase on lifespan in C. elegans. Nature 426: 620. doi: 10.1038/426620a.

53. Wolff, S. and Dillin, A. 2006. The trifecta of aging in Caenorhabditis elegans. Exp. Gerontol. 41: 894-903.

54. Wolkow, C.A., Kimura, K.D., Lee, M.S., and Ruvkun, G. 2000. Regulation of C. elegans life-span by insulinlike signaling in the nervous system. Science 290: 147-150.

55. Yang, Q., Inoki, K., Ikenoue, T., and Guan, K.L. 2006. Identification of Sin1 as an essential TORC2 component required for complex formation and kinase activity. Genes Dev. 20: 2820-2832.

Figure 4.8 *(following page)*: Similarity of RICT-1 and human Rictor. (A) Intron-exon structure of *rict-1* (F29C12.3), with premature stop mutations in mg450 and mg451 shown as asterisks. (B) sequence alignment of Rictor across multiple species indicating sequences of primary conservation. RICT-1 (F29C12.3) amino acid side chains are 50% similar and 16% identical to human Rictor. Red color coding indicates residue identity across species, and blue and green indicate residue similarity. Amino acid substitution with stop codons of *mg450* and *mg451* are shown below the primary sequence. Sequences were aligned using Culstal

Figure 4.8: (continued)

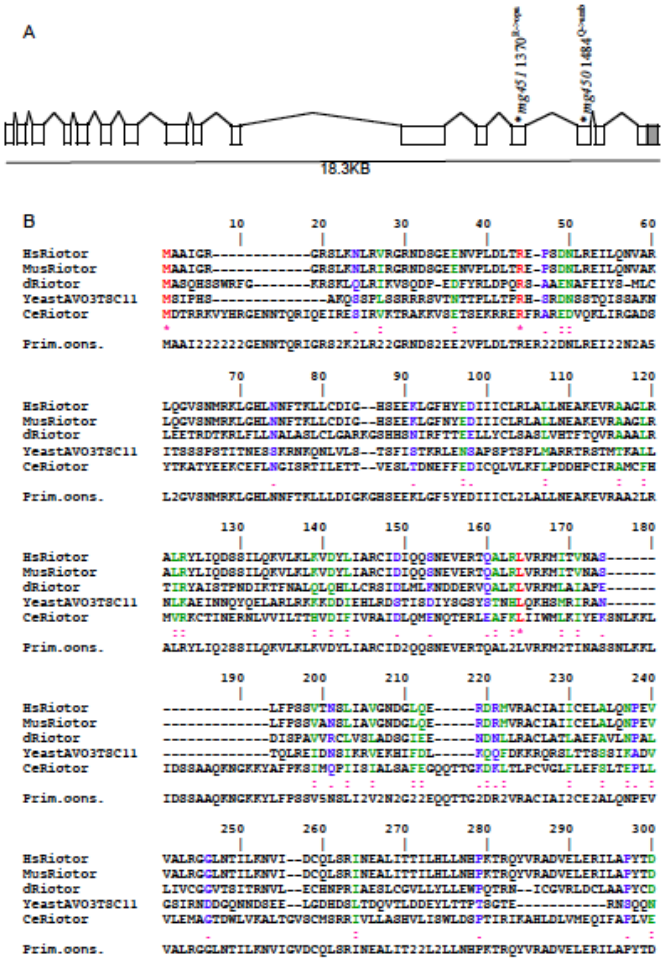

Figure 4.8: (continued)

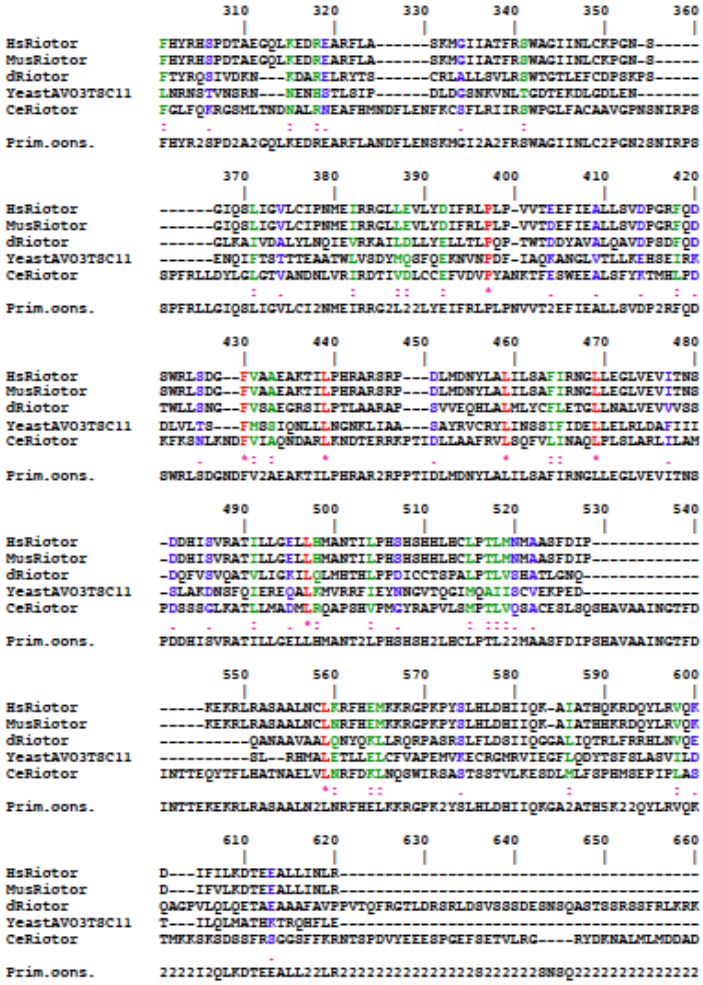

Figure 4.8: (continued)

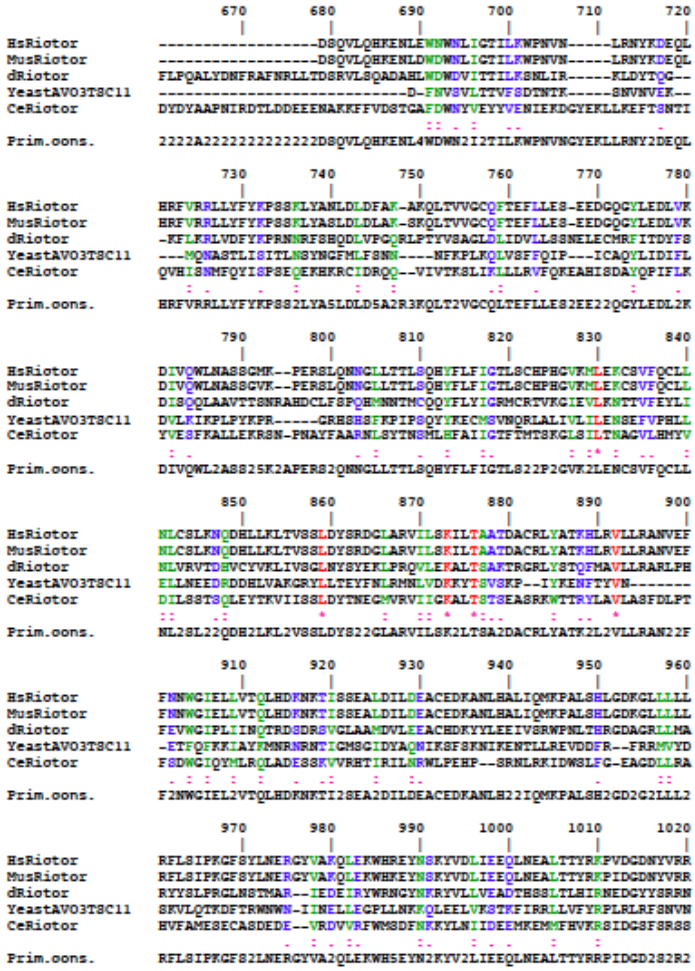

Figure 4.8: (continued)

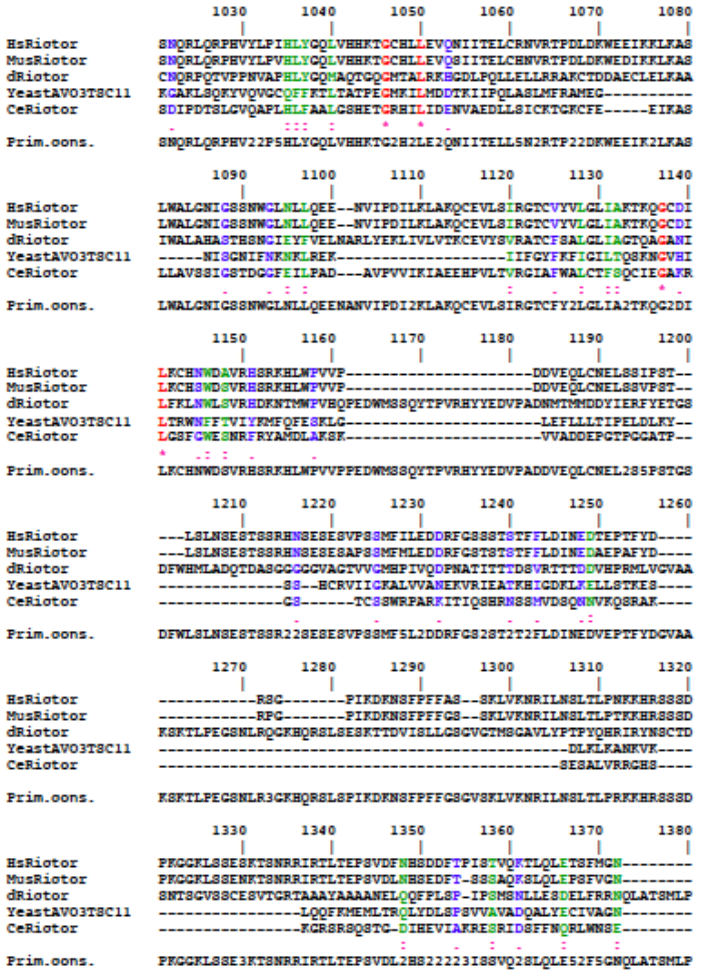

Figure 4.8: (continued)

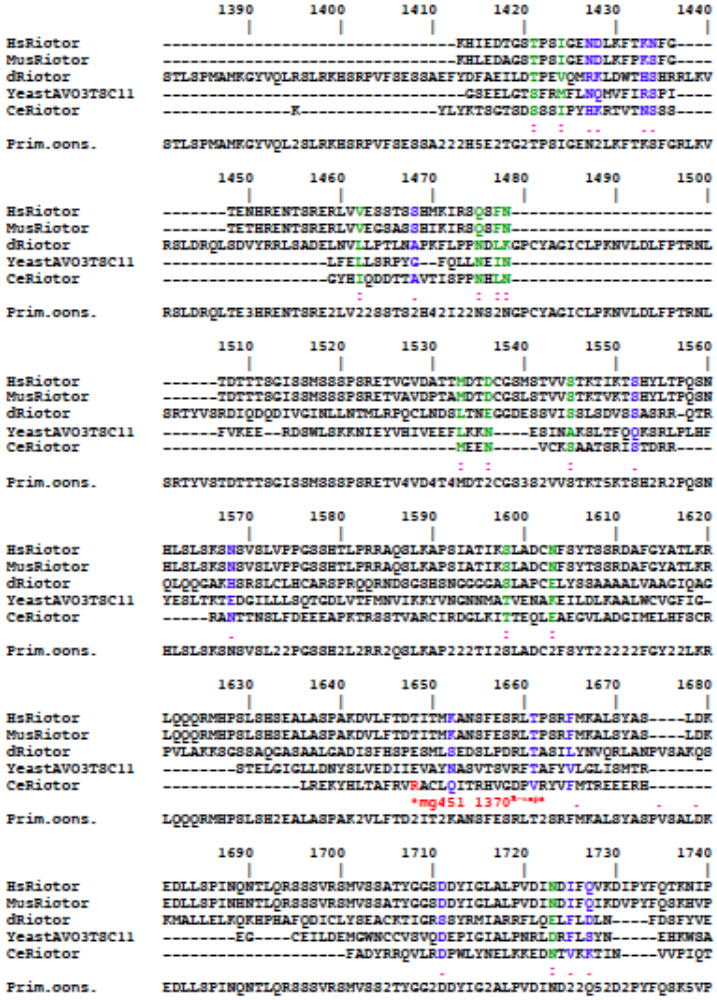

Figure 4.8: (continued)

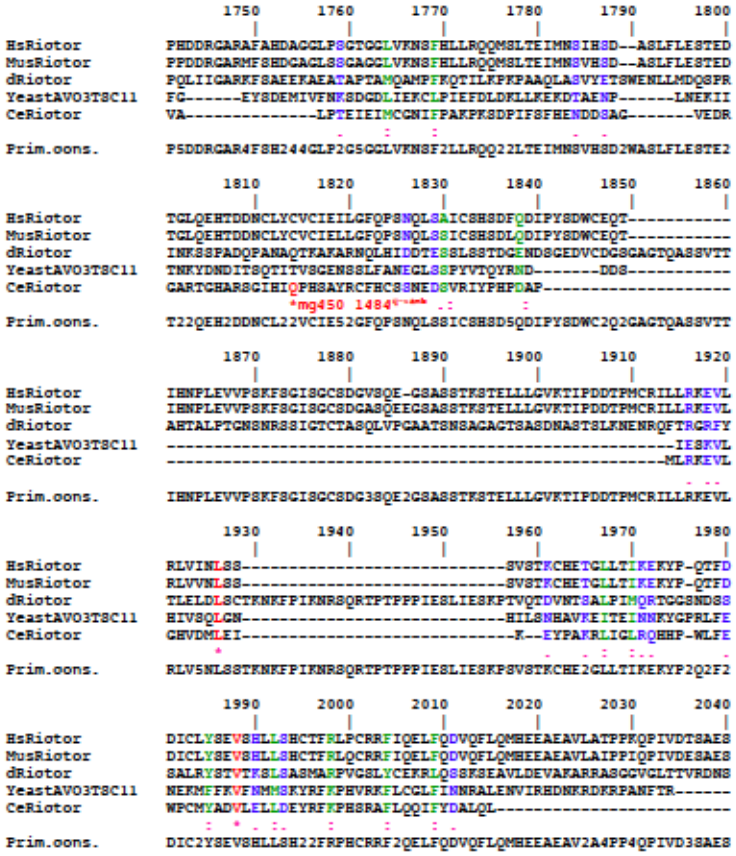

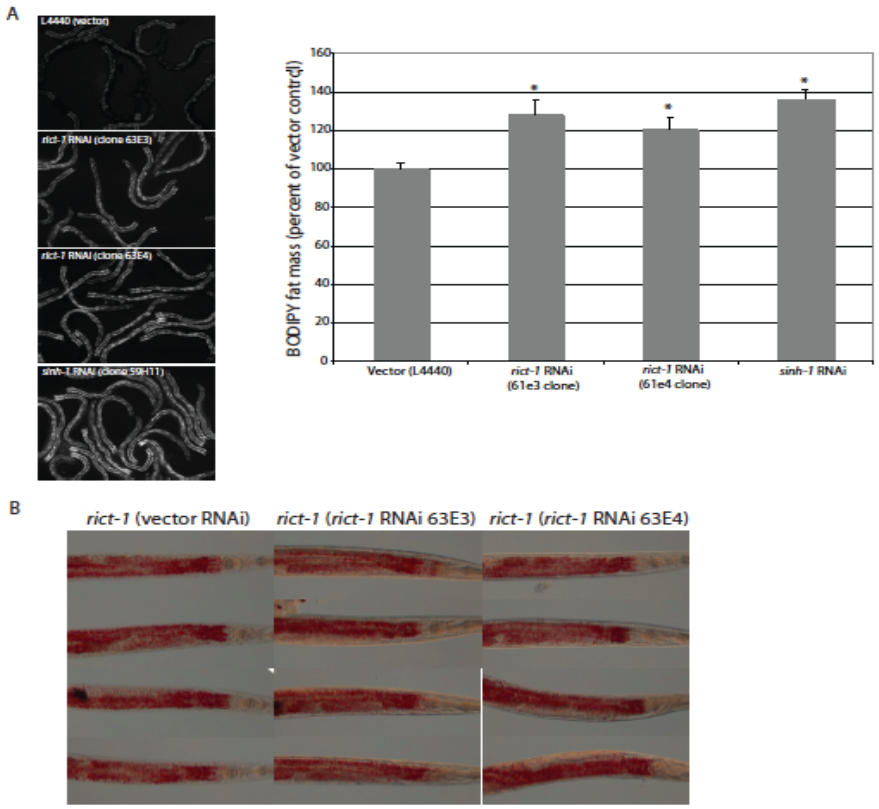

Figure 4.9: RNAi of *rict-1* and *sinh-1*, the *C. elegans* homologue of *mSin1*. (A) RNAi of *rict-1* and *sinh-1* in wild-type animals produces high-fat phenotypes as assessed by BODIPY staining. *, $p < 10^{-10}$ by 2-tailed t-test. (B) RNAi of *rict-1* in *rict-1(mg451)* mutants does not further enhance high fat phenotype as assessed by Oil-Red-O staining.

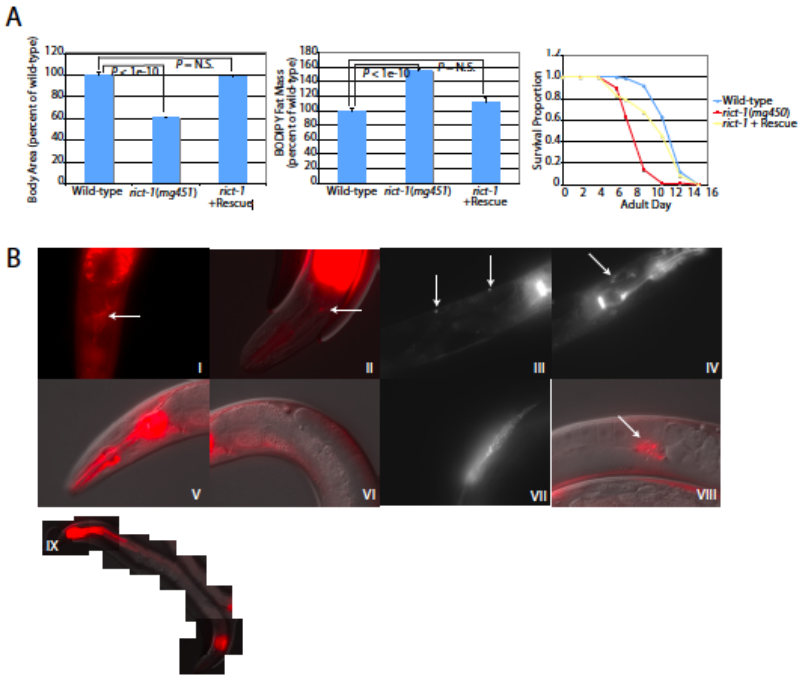

Figure 4.10: Transgenic rescue and tissue distribution of *rict-1*G. (A) *rict-1*G mutant animals carrying a transgene expressing *rict-1*G cDNA under the *rict-1*G promoter (*rict-1G;Ex[rict-1p::RICT-1]*) show rescue of high body fat, small body size, and short lifespan phenotypes. (B) Tissues expressing *rict-1*G were determined by injecting wild-type animals with a transgene expressing RFP under the *rict-1*G promoter. I, II, IV, head neurons; III, ventral cord neurons; V, pharynx; VI, VII, body wall muscle; VIII spermatheca; and IX, intestine.

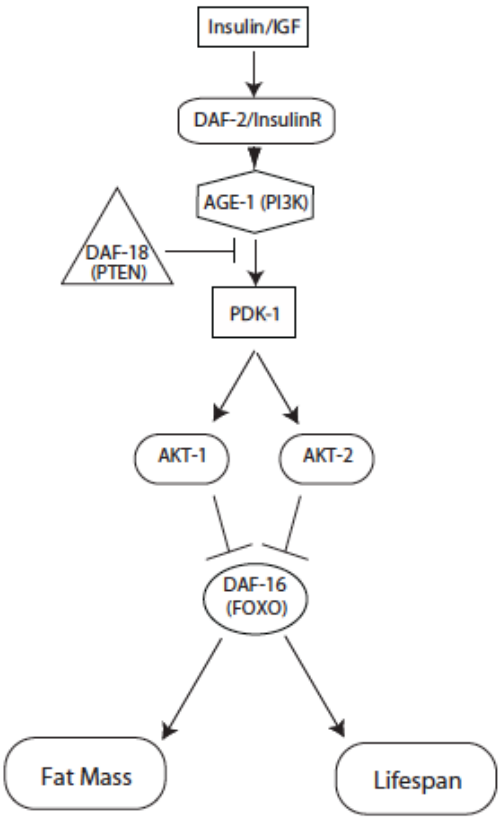

Figure 4.11: Insulin/IGF signaling pathway components known to control fat mass and lifespan in *C. elegans*. Insulin-like signals relay through the single insulin/IGF receptor homologue DAF-2, activating AGE-1, the single PI3 Kinase homologue. This activates the kinase cascade PDK-1 which subsequently phosphorylates and activates AKT-1 and AKT-2. The AKT kinases are responsible for phosphorylating and inhibiting the FOXO transcription factor homologue DAF-16, leading to its exclusion from the nucleus. DAF-18, the single *C. elegans* PTEN homologue, antagonizes insulin-like signaling downstream of AGE-1. Inactivation of insulin signaling at the level of *daf-2* and *age-1* lead to increased fat mass and increased lifespan through decreased inhibition of DAF-16

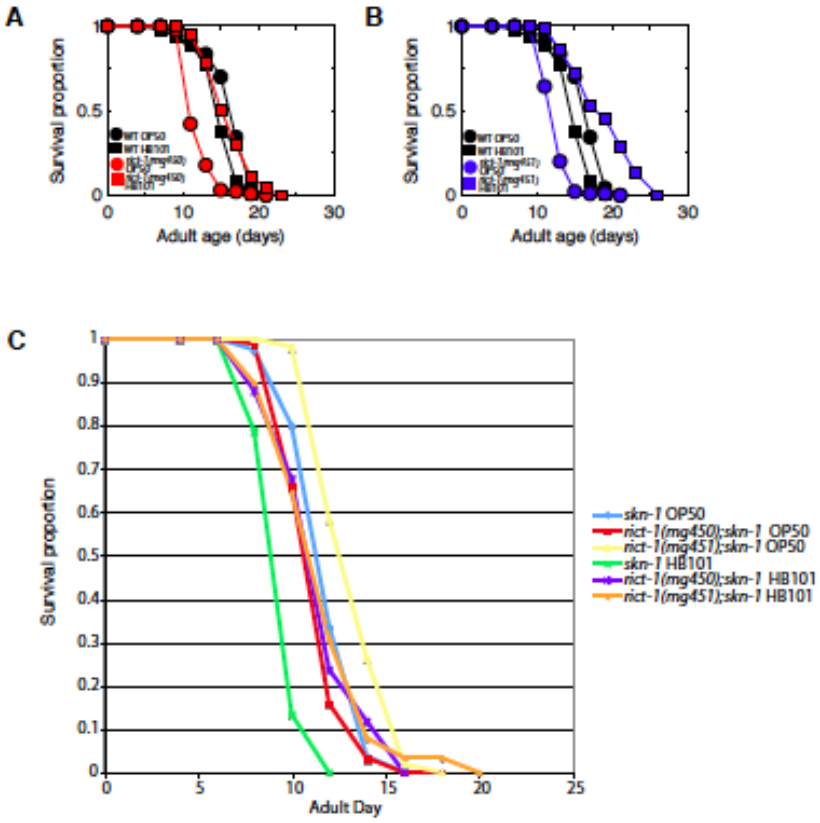

Figure 4.12: Repeat lifespan assay of *rict-1* mutants on HB101 and lifespan epistasis in *rict-1*;*skn-1* double mutants fed HB101. (A) Confirming the results of the first experiment (Figure 4.4), HB101 had marginal (-10%) impact on wild-type (WT) lifespan versus OP50, and HB101 extended *rict-1(mg450)* lifespan by 39%. (B) As before (Figure 4.4), HB101 versus OP50 had a similar impact on *rict-1(mg451)*, increasing lifespan by 56%. (C) The *rict-1*;*skn-1(zu169)* double mutant no longer has lifespan extension when fed HB101 relative to OP50, indicating that the lifespan extension induced by *rict-1* mutants fed HB101 is due to caloric restriction since *skn-1* is necessary for dietary-restriction induced longevity (Bishop and Guarente, 2007).

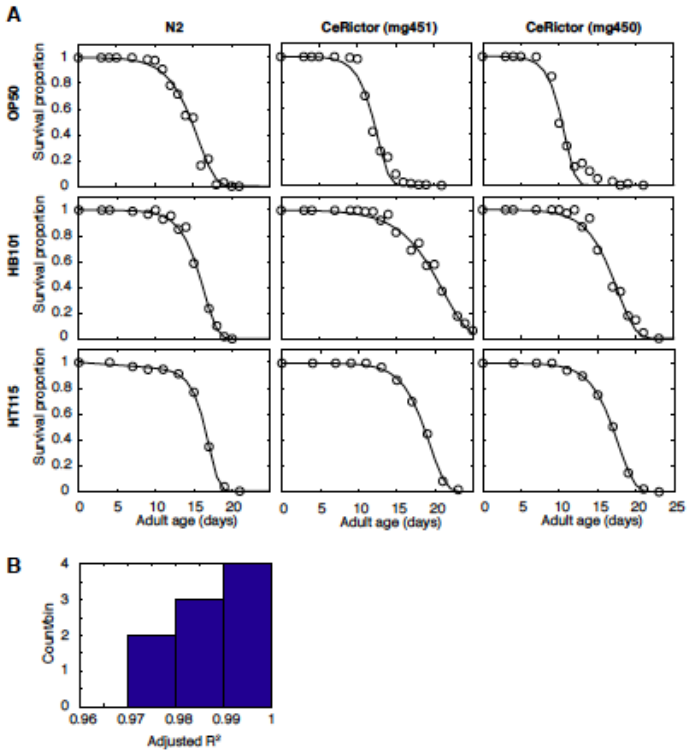

Figure 4.13: Gompertz-Makeham survival analysis. (A) Model fits compared to survival data for each strain (column) and diet (row) combination. (B) Histogram of degree-of-freedom adjusted Pearson correlation coefficients (Adj. R2) for fits in a. See Supplementary Figure 4.17 for best-fit parameters.

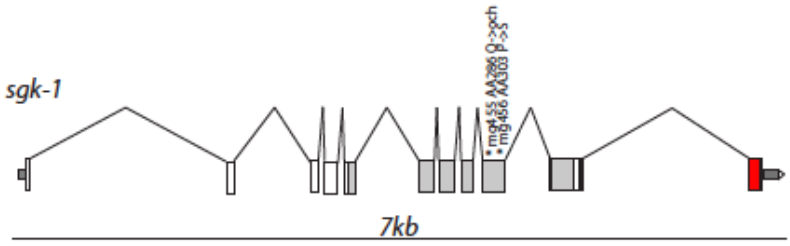

Figure 4.14: Intron-exon structure of *sgk-1* with high fat mutations. (A) *sgk-1* has 11 predicted exons, with the coding region shown in the larger boxes, untranslated regions in small, dark-gray boxes, the kinase region in light-gray, and the C-terminal, conserved, protein kinase C domain containing the TORC2 phosphorylation HM site in red. *sgk-1(mg455)* removes critical sections of the kinase domain and is predicted to lack the PKC domain and HM as it encodes an early stop. *sgk-1(mg456)* is a coding region P to S missense mutation within the kinase domain.

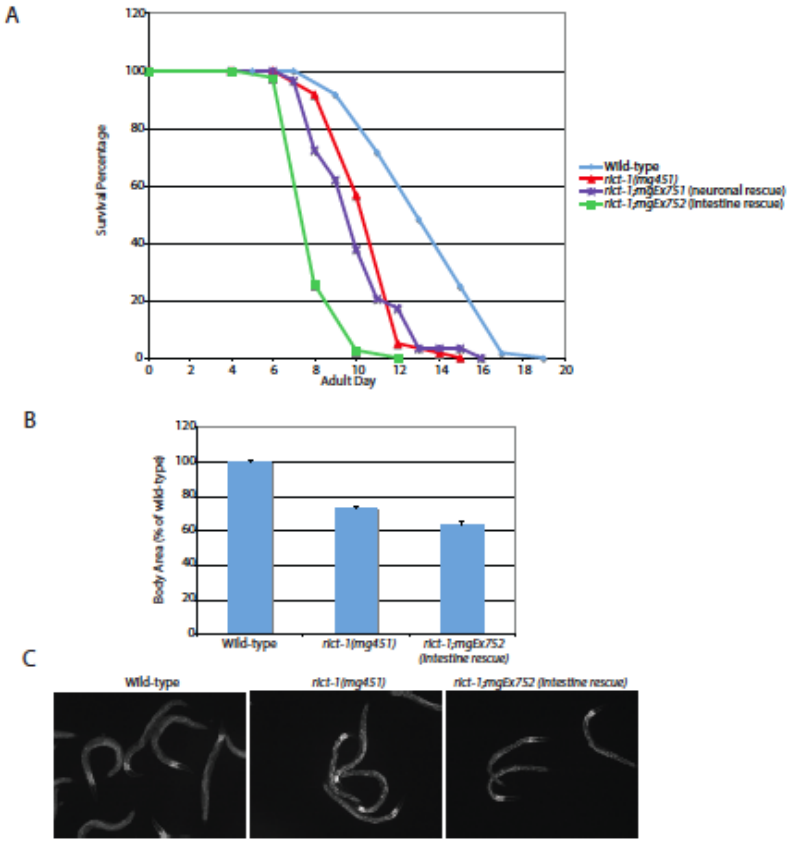

Figure 4.15: Lifespan is not rescued in transmitting neuronal and intestinal rescue *rict-1* transgenic animals. (A) transgenic rescue of *rict-1* in neurons does not rescue the short lifespan of *rict-1* mutants (*rict-1;mgEx751[unc-119p::RICT-1]*). Transgenic rescue of *rict-1* in the intestine (*rict-1;mgEx752[ges-1p::RICT-1]*) in the single, transmitting transgenic line obtained for the intestine did not rescue lifespan, but this line also (B,C) did not rescue small body size or high body fat and was somewhat slow growing and short

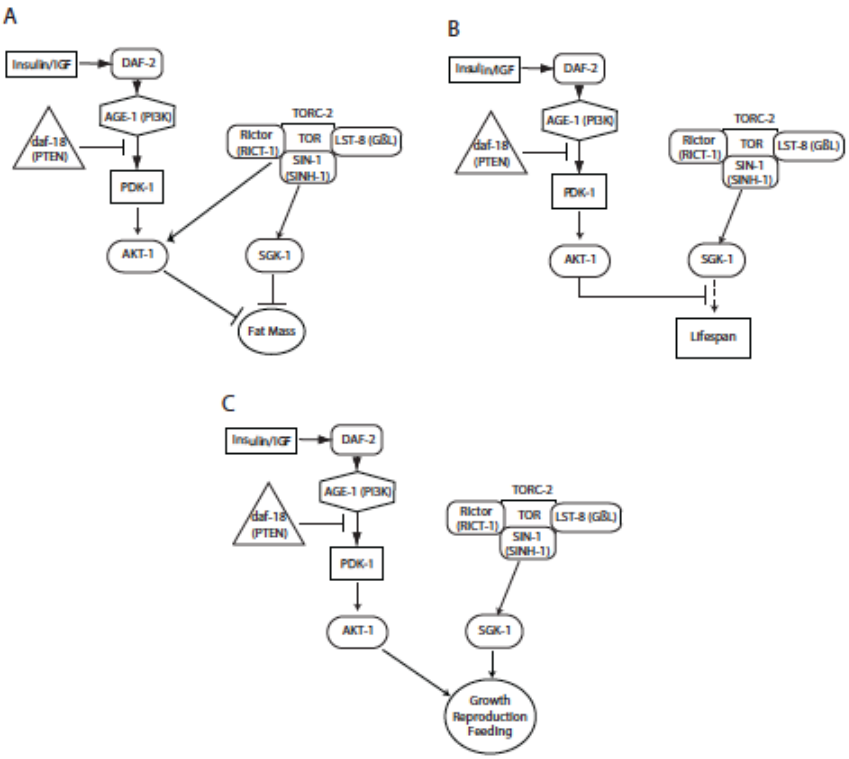

Figure 4.16: Model of RICT-1/TORC2 regulation of fat mass, lifespan, growth, reproduction, and feeding. (A) TORC2 signals through both AKT-1 and SGK-1 to negatively regulate fat mass. In the case of a *rict-1* mutant, loss of HM phosphorylation of AKT-1 and SGK-1 leads to excess fat mass accumulation. (B) TORC2 signals exclusively through SGK-1 to positively regulate lifespan, however, insulin-like signaling through AKT converges on this output downstream of SGK-1 as *rict-1;akt-1* double mutants show reversal of their short lifespan. Thus, AKT-1 is necessary but not sufficient to generate the progeric phenotype of *rict-1* since it itself is not short lived. (C) The RICT-1/TORC2 mutant slow growth, decreased brood size, and feeding behavior defects (on *E. coli* HB101) are mediated by SGK-1. Thus, although insulin-like signaling through AKT is known to regulate these processes, it does so in parallel to TORC2 signaling.

Supplementary Table 1 Gompertz-Makeham survival analysis fits

Diet	Strain	G (day^{-1})	$\ln(M_0)$	$\ln(R_0)$	Adj. R^2	Lifespan (adult days)	
OP50	Wild-type (N2)	0.47±0.03	-6.80	-22.5	0.997	12.1	13.6
OP50	*rict-1* (*mg450*)	0.57±0.12	-5.53	-27.2	0.972	8.0*	9.2
OP50	*rict-1* (*mg451*)	0.63±0.11	-6.85	-24.2	0.980	9.6*	10.7
HB101	Wild-type (N2)	0.57±0.09	-8.17	-7.86	0.993	12.7**	13.9
HB101	*rict-1* (*mg450*)	0.43±0.05	-7.13	-22.3	0.987	13.8*,**	15.4
HB101	*rict-1* (*mg451*)	0.30±0.03	-6.63	-23.6	0.990	17.0*,**	19.3
HT115	Wild-type (N2)	0.81±0.09	-11.6	-5.0	0.999	13.4**	14.4
HT115	*rict-1* (*mg450*)	0.48±0.04	-7.81	-7.86	0.999	14.0*,**	15.4
HT115	*rict-1* (*mg451*)	0.48±0.03	-8.57	-24.5	0.999	15.5*,**	17.0

Fits to pooled data from experiments 1-5. Rate of aging G is estimate ± standard deviation. Median (left) and maximum (right) lifespan are estimated as of 50% and 25% survival in adult days, respectively, based on Gompertz-Makeham fit. Kaplan Meier hypothesis tests based upon experiment 3: (*) $P < 0.0001$ vs. N2 on same food source; (**) $P < 0.0001$ vs. same strain on OP50.

Figure 4.17: Supplementary Table 1: Gompertz-Makeham survival analysis fits

Supplementary Table 2. *Lifespan data for* rict-1;FOXO *and* rict-1;akt *double mutants*

Strain	Mean Lifespan	Median Lifespan	25% Survival
N2	13.37 ± 0.23	13 ± 0.3	15 ±0.17
rict-1 (mg450)	10.3 ± 0.15 **	11 ± 0.11	11 ± 0.11
rict-1 (mg451)	11.24 ± 0.15 **	11 ± 0.19	13 ± 0.19
FOXO	8.78 ± 0.1 **	9 ± 0.07	9 ± 0.07
rict-1 (mg450);FOXO	6.78 ± 0.07 **,††	7 ± 0.00	7 ± 0.00
rict-1 (mg451);FOXO	6.8 ± 0.06 **,††	7 ± 0.00	7 ± 0.00
akt-1 (mg306)	18.62 ± 0.22 **	19 ± 0.24	19 ± 0.32
rict-1 (mg450);akt-1	21.62 ± 0.24 **,††	21 ± 0.33	23 ± 0.21
rict-1 (mg451);akt-1	22.7 ± 0.25 **,††	23 ± 0.21	23 ± 0.32
akt-2 (ok393)	14.38 ± 0.22 *	15 ± 0.19	15 ± 0.19
rict-1 (mg450);akt-2	11.65 ± 0.28 *,††	11 ± 0.36	13 ± 0.27
rict-1 (mg451);akt-2	11.69 ± 0.16 **	11 ± 0.21	13 ± 0.11

Mean, median and 25% survival (maximum) in adult days ± s.e. [Kaplan Meier hypothesis tests: (*) $P < 0.01$ vs. N2 on same food source; (**) $P < 0.0001$ vs. N2 on same food source; (††) $P < 0.0001$ vs. *rict-1* single mutant.

Figure 4.18: Supplementary Table 2. Lifespan data for *rict-1;FOXO* and *rict-1;akt* double mutants

5

Appendix 2: Two alternating motor programs drive navigation in *Drosophila* larva

5.1 Authors

Subhaneil Lahiri, Konlin Shen, Mason Klein, Anji Tang, Elizabeth Kane, Marc Gershow, Paul Garrity, Aravinthan D. T. Samuel

5.2 Publication note

A version of this appendix was published as the following article: Lahiri S, Shen K, Klein M, Tang A, Kane E, Gershow M, Garrity P, Samuel AD. Two alternating motor programs drive navigation in *Drosophila* larva. *PLoS One.* 2011;6(8):e23180. Epub 2011 Aug 15.

5.3 Abstract

When placed on a temperature gradient, a *Drosophila* larva navigates away from excessive cold or heat by regulating the size, frequency, and direction of reorientation maneuvers between successive periods of forward movement. Forward movement is driven by peristalsis waves that travel from tail to head. During each reorientation maneuver, the larva pauses and sweeps its head from side to side until it picks a new direction for forward movement. Here, we characterized the motor programs that underlie the initiation, execution, and completion of reorientation maneuvers by measuring body segment dynamics of freely moving larvae with fluorescent muscle fibers as they were exposed to temporal changes in temperature. We find that reorientation maneuvers are characterized by highly stereotyped spatiotemporal patterns of segment dynamics. Reorientation maneuvers are initiated with head sweeping movement driven by asymmetric contraction of a portion of anterior body segments. The larva attains a new direction for forward movement after head sweeping movement by using peristalsis waves that gradually push posterior body segments out of alignment with the tail (i.e., the previous direction of forward movement) into alignment with the head. Thus, reorientation maneuvers during thermotaxis are carried out by two alternating motor programs: (1) peristalsis for driving forward movement and (2) asymmetric contraction of anterior body segments for driving head sweeping movement.

5.4 Introduction

Systems neuroscience strives to connect animal behavior to the structure and dynamics of the nervous system. By studying brain and behavior in the *Drosophila* larva, a genetically tractable model organism with a small nervous system and simple body plan, it might be possible to characterize the pathways that encode complex behaviors all the way from sensory input to motor output. To reach this goal, we must develop tools to interrogate all layers of neuronal and muscle dynamics that occur during behavior.

Thermotaxis is a particularly sophisticated behavior exhibited by the *Drosophila* larva [1-3]. The navigational strategies of larval thermotaxis were recently analyzed by using a tracking microscope to follow the movements of individual an-

imals responding to defined temperature gradients [4]. In brief, a larva's crawling trajectory can be characterized as a sequence of periods of persistent forward movement (runs) that are interrupted at random by reorientation maneuvers. During a reorientation maneuver, the larva pauses and sweeps its head one or more times until it picks a new direction in which to resume forward movement [5]. Thus, the reorientation maneuvers along an animal's trajectory may be interpreted as a sequence of navigational decisions. In temperature gradients, the larva biases the size, frequency, and direction of these reorientation maneuvers to enhance the likelihood that its overall trajectory trends towards favorable temperatures [4].

Chemotactic and thermotactic navigation in simpler organisms like the bacterium *E. coli* or the nematode *C. elegans* also involves alternating sequences of forward movements and reorientation maneuvers [6-8]. However, bacteria and nematodes only bias the frequency of abrupt reorientations in response to changing conditions, exhibiting longer runs when headed in favorable directions and shorter runs when headed in unfavorable directions. By additionally biasing the size and direction of reorientation maneuvers, larvae are able to exhibit more runs in favorable direction, thereby increasing the rate at which they improve their surroundings [4].

The navigational behaviors of the *Drosophila* larva are encoded in neural circuits that activate appropriate motor programs in response to sensory inputs. It is straightforward to estimate sensory input during larval thermotaxis by measuring the position of the larva's body in ambient spatial or temporal gradients. It is less easy to characterize the motor programs that are used during thermotaxis. Because each body segment of the *Drosophila* larva can contract or expand, it is difficult to infer motor dynamics from the outline of the larva's body. Fluorescence microscopy offers a solution: it is possible to visualize the movements of individual segments within transgenic animals in which GFP is fused to the myosin heavy chain [9,10]. Here, by imaging segment dynamics of freely moving transgenic larvae, we characterize the motor programs that the *Drosophila* larva uses to initiate, execute, and complete reorientation maneuvers during navigation.

5.5 Results

5.5.1 Visualizing motor dynamics in freely moving larvae

Transgenic *Drosophila* larva with GFP fused to the myosin heavy chain (*w;Mhc-GFPc110/CyO*) permit the visualization of thoracic and abdominal body segments in the freely moving animal using fluorescence microscopy [9,10] (Figure 5.1A). To facilitate quantification, we developed semi-automated machine-vision software that analyzes the fluorescent images of these crawling larvae to automatically extract the outer boundary, identifies the head and tail, and measures the curvature of the body centerline that is associated with turning decisions (Figure 5.1B). Within these image frames, the coordinates of the intersections of the boundaries between each segment with the outer boundary of the animal can be precisely located by hand. Once this coordinate system has been imposed on each video frame, it is straightforward to quantify the contractile dynamics of each of three thoracic body segments (T1...T3) and eight abdominal segments (A1...A8). The mouth segment and the terminal/A9 segment cannot be distinguished in this way due to the lack of sharp boundaries in their musculature. Forward movement of the *Drosophila* larva, as in other Diptera species, is driven by waves of peristalsis that travel from tail to head [11]. We began by quantifying body segment dynamics during forward movement, using a tracking microscope that captured high-resolution fluorescence video of freely crawling larvae (Figure 5.2; Video 1). Consistent with previous observations, waves of contraction propagate with nearly constant speed from tail to head during forward movement, starting at the rear-most abdominal segments and ending at the T2 or T1 thoracic segment, each wave producing, 0.13 body lengths of forward displacement (Figure 5.3A) [9,12].

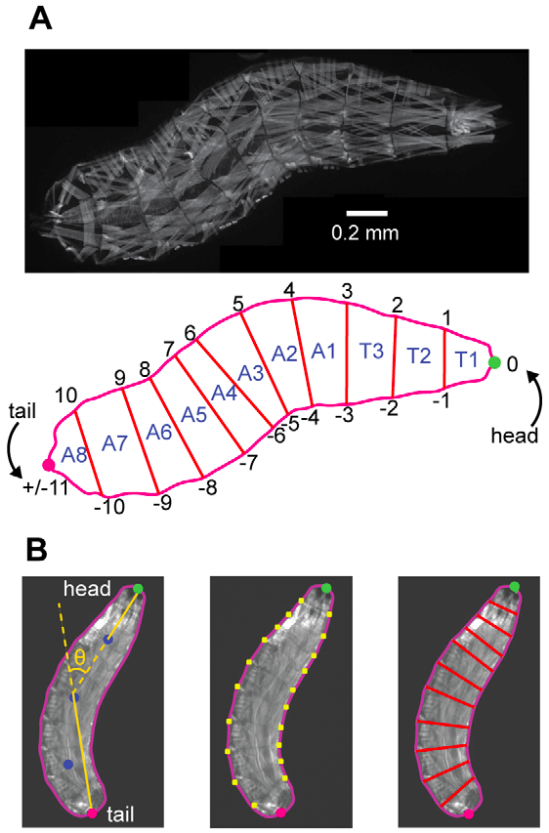

Figure 5.1: Segmentation of *Drosophila* larva. A. (Upper) Fluorescence micrograph of *w;Mhc-GFPc110/CyO* larva (Lower) Coordinate system for delineating the three thoracic (T1...T3) and eight abdominal (A1...A8) segments. The tip of the head and tail are defined as 0 and ± 11, respectively. Boundaries between adjacent segments are numbered from $+1$ to $+10$ along the left side of the animal and from 21 to 210 along the right side, as shown. B. Steps in video analysis. Left The boundary, head (green dot), tail (red dot), points along the centerline (blue dots), and operational definition of bend angle used to flag reorientation maneuvers are calculated using machine-vision algorithms described in Materials and Methods. Center The twenty points ($+1$ to $+10$ and -1 to -10) that define the boundaries between segments are identified by hand (yellow dots). Right The lengths of the boundaries between segments or fluorescence intensity within segments can be used as measures of segment contraction.

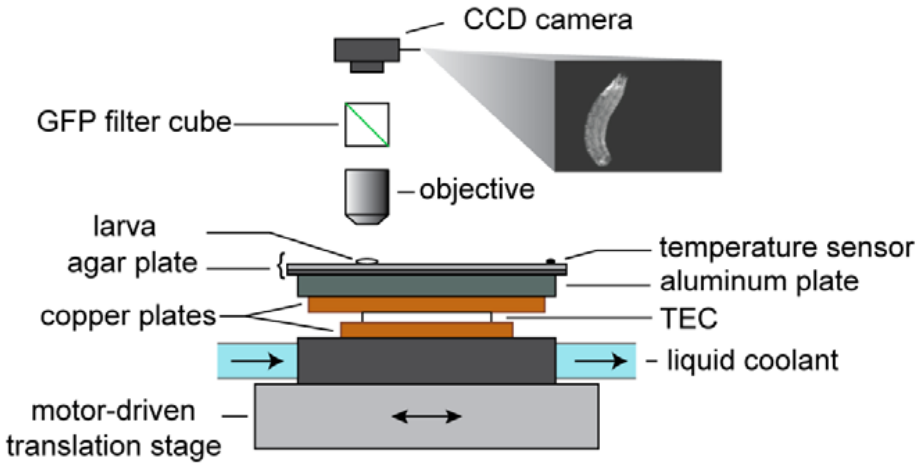

Figure 5.2: Experimental setup. Spatially uniform, temporal variations in temperature were achieved by controlling the temperature of an aluminum slab with a feedback-controlled thermoelectric controller (TEC). The TEC was coupled to the aluminum slab and liquid-cooled heat sink by copper plates. A motor-driven microscope stage kept each larva within the center of the field of view as it was subjected to defined temperature waveforms as high-resolution video of GFP fluorescence was captured by CCD camera.

One measure of segment dynamics during the contraction wave is provided in the lengths of the left and right boundaries of each segment. Another measure is mean fluorescence intensity because muscle contraction increases the local concentration of GFP. Waves of contraction can be graphically represented either with kymographs that show fractional changes in the length of body segment boundaries over time or in the fluorescence intensity of the pixels within each body segment over time (Figure 5.3B).

When each body segment is viewed separately, its fluorescence intensity oscillates in a rhythmic manner with successive peristalsis waves. The slight phase shift in the rhythmic oscillation between adjacent segments is due to the propagation of the wave from tail to head. This rhythmic variation in fluorescence intensity is pronounced in the abdominal segments and the T3 thoracic segment, but becomes less noticeable in the T2 segment and especially the T1 segment (Figure 5.3C). To better understand the two measures of segment contraction, we quantified the

Figure 5.3 ***(following page)*****:** Forward movement. A. Video frames showing four peristalsis waves of a larva during forward movement. The larva is kept in the center of the field of view with an automated tracking stage. Outline and boundaries between segments are shown in red, applied using the steps described in Figure 5.1B. Yellow arrowheads mark the propagation of the first peristalsis wave from tail to head. B. Kymographs showing two measures of body segment contraction. Segment boundaries are used to define the coordinate system along the body as shown in the schematic (also see Figure 5.1B), with integers specifying boundaries between segments from head (0) to tail ($\pm$11) along the larva's left side (0 to $+$11) and right side (0 to -11). (Upper) Fractional changes in the lengths of each segment boundary relative to a reference image between peristalsis waves. (Lower) Fractional changes in the mean fluorescence intensity within body segments relative to a reference image. In both kymographs, yellow arrowheads mark the propagation of a peak of body segment contraction from tail to head during the first peristalsis wave. C. Temporal variations in the mean fluorescence intensity within each body segment taken from the kymograph of B. Vertical scale bar indicates 20% change in fractional fluorescence intensity.

Figure 5.3: (continued)

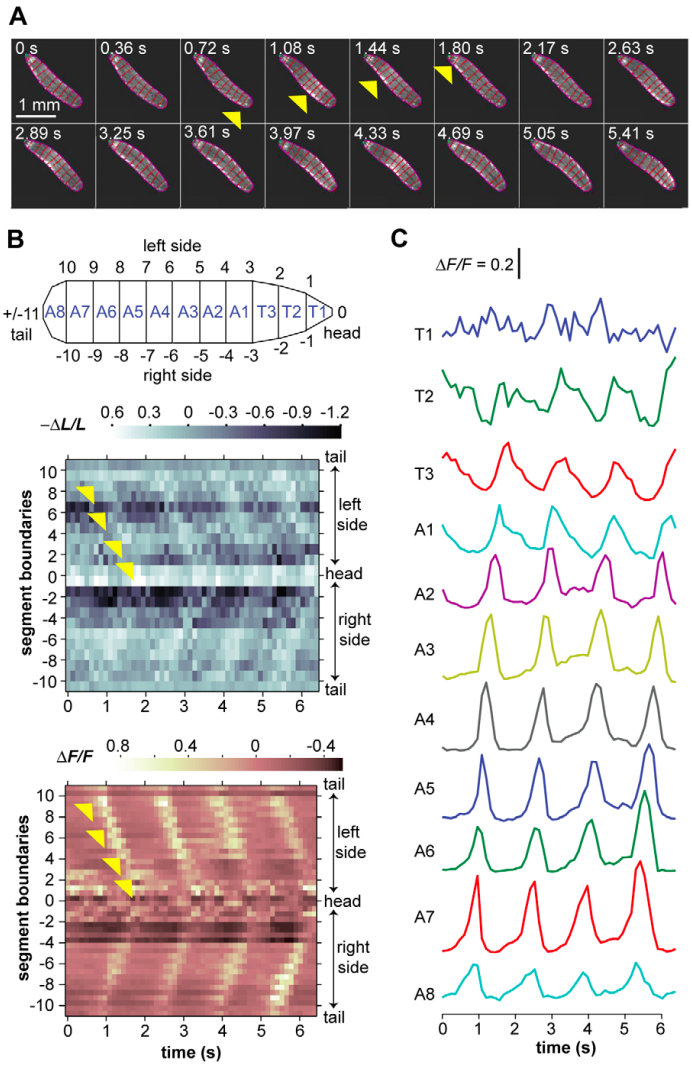

correlation between the two sets of measurements across our data sets (Figure 5.4). For most segments, increases in fluorescent intensity are strongly correlated with decreases in segment length, as expected. However, at the front, the correlation between fluorescence intensity and segment length becomes smaller in T2 and nearly vanishes in T1. At the rear of the animal, the correlation becomes smaller in A7 and increases in fluorescent intensity become weakly correlated with increases in segment length in A8. The detailed motions of the frontmost and rearmost segments could be more complicated than middle segments. For example, the larva's mouth can exhibit foraging movements, rapid, small amplitude side-to-side movements that seem to be driven by T1. However, the loss of correlation in the two measures of segment contraction at the head and tail could also be partly due to measurement artifact, e.g., owing to the triangular shape of the T1 and A8 segments, measuring the lengths of their left and right sides will be strongly affected by errors in locating their tips.

5.5.2 Motor dynamics during navigational decision-making

The navigational strategy for larva thermotaxis is based in the regulation of head sweeping movements during the reorientation maneuvers that separate successive periods of forward movement [4]. First and second instar *Drosophila* larvae avoid temperatures below ,22°*C*. First, we verified that transgenic *Drosophila* larvae (*w;Mhc-GFPc110/CyO*) exhibit cold-avoidance behavior by placing them on spatial temperature gradients. When started at 17°*C* on linear temperature gradients (0.3°*C*/cm), both wild-type (Canton S) and transgenic larvae crawl towards warmer temperatures at comparable rates (Figure 5.6). The instantaneous crawling speeds of both types of larvae during periods of forward movement are also comparable. Moreover, navigational decisions during thermotaxis are informed by temporal comparisons in temperature. Thus, the frequency of turning decisions and size of head sweeps during turning decisions are greater for cooling ramps than for warming ramps at temperatures around 20°*C* (Figure 5.6). We verified that both wild-type and transgenic larva exhibit these biases in behavior (Figure 5.6). Taken together, these results suggest that the transgenic larvae do not suffer severe locomotor or navigational impairments. We note that the white mutation

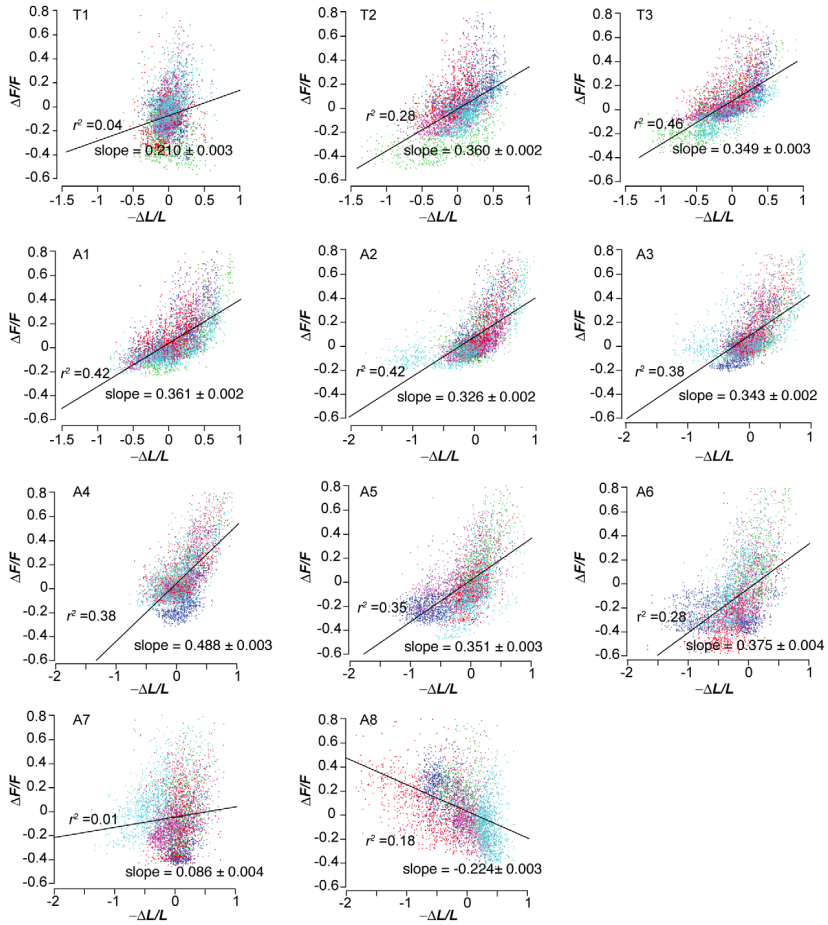

Figure 5.4: Fractional change in fluorescence intensity vs. fractional change in segment length. Scatter plots of each pair of measurements of each segment's dynamics taken from video of 5 larvae. Data points for each animal are shown in a different color, and each data point represents the analysis of one video frame. Correlation coefficients and the slope $\pm$ one standard error for the linear regression (black line) of each scatter plot are shown.

that is carried by the transgenic larvae has been reported to reduce dopamine and serotonin levels in the larval central nervous system, which may account for differences in the magnitude of the thermosensory response (Figure 5.6) [13-15].

To visualize muscle dynamics during navigational decisions, we subjected individual transgenic larvae to sinusoidal variations between $14^{\circ}C$ and $16^{\circ}C$ with 2 min period while tracking their movements using the experimental setup shown in Figure 5.2. Here, we analyzed 46 abrupt turns exhibited by 10 transgenic larvae that were individually tracked in the new setup, 26 that occurred during the cooling phase and 20 that occurred during the warming phase of the sinusoidal stimulus. We designated turns as large (9 of which occurred during warming and 13 during cooling) or small (11 of which occurred during warming and 13 during cooling) when the body bend angles were greater or smaller than 90u, respectively.

Video segments and analysis of four example turning decisions are shown in Figures 5.5, 5.7, 5.8, 5.9. A reorientation maneuver involving one small leftward head sweep during warming is shown in Figure 5.5 (Video 2). A turning decision involving one small leftward head sweep during cooling is shown in Figure 5.7 (Video 3). A reorientation maneuver involving one large rightward head sweep during cooling is shown in Figure 5.8 (Video 4). A reorientation maneuver involving two large head sweeps in rapid succession during cooling, one leftward and one rightward, is shown in Figure 5.9 (Video 5). Below we discuss how comparison of the time-varying posture of each larva with corresponding kymographs of segment contraction were used to reveal the motor sequences that correspond to the initiation, execution, and completion of reorientation maneuvers.

In every case, we found that the onset of head sweeping during reorientation maneuvers (identified as events in which the body centerline bends by more than 40u) occurs after the end of the previous peristalsis cycle (Figure 5.5 and Video 2; Figure 5.7 and Video 3; Figure 5.8 and Video 4; Figure 5.9 and Video 5). This observation suggests a distinct transition from the peristaltic motor program for forward movement to the asymmetric contraction motor program for initiating head sweeping for each reorientation maneuver.

Next, we looked at how body segments are used to actuate head sweeps. To

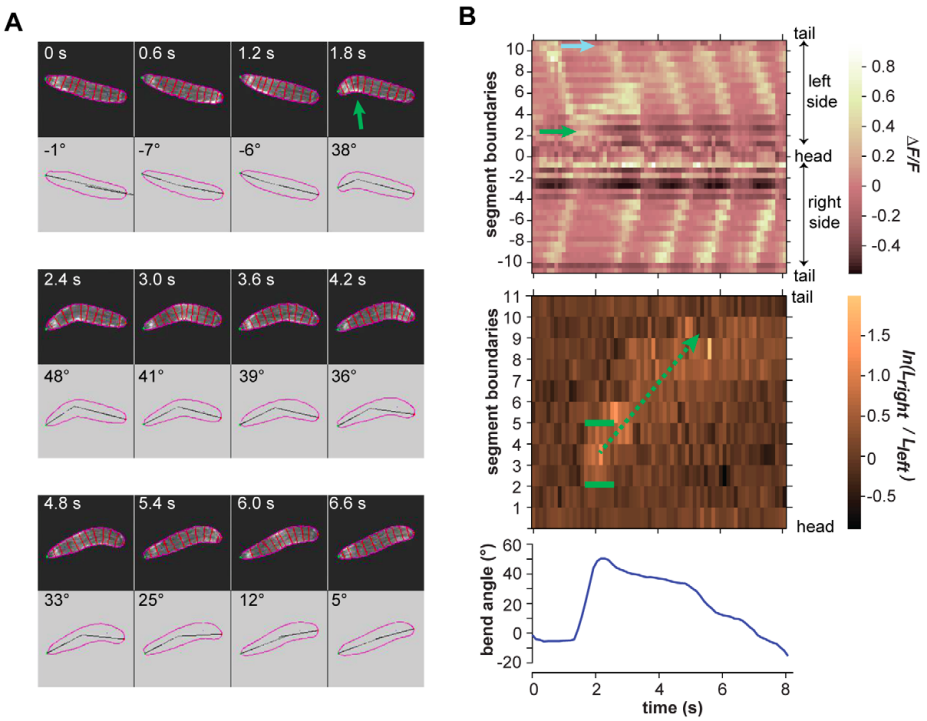

Figure 5.5: Turning decisions with small head sweeps. A. Video frames of an example small head sweep during warming. Upper panel in each video frame shows fluorescence image. Outline and boundaries between segments are shown in red. Lower panel in each video frame shows the perimeter, centerline, and body bend angle as analyzed by machine vision software. Green arrow shows the asymmetric bend that is flagged as a head sweep. B. (Upper panel) Kymograph of fluorescence intensity within body segments for the video segment shown in A. Green arrow shows the increase in fluorescence intensity on the left side of the animal, signifying the leftward head sweep. Blue arrow shows the increase in fluorescence intensity in the A8 segment, signifying the resumption of peristalsis at the tail. (Middle panel) Kymograph of the logarithm of the ratio between the lengths of segment boundaries on the left side and right side of the animal. Green brackets indicate the margins of the region of asymmetric contraction, positive values signifying the leftward bend. Green arrow shows the retrograde progression of the region of asymmetric contraction during the four subsequent peristalsis waves. (Lower panel) Time course of body bend angle, operationally defined to flag reorientation maneuvers as described in Materials and Methods, shows the initial rise that signifies the leftward head sweep and gradual decline as subsequent peristalsis waves straighten the body.

Table 1. Thermotaxis parameters.

	Canton S	*wgMhc-GFP*^{CT10}*/CyO*
On spatial gradients		
Thermotaxis speed (mm/s)	0.075±.002	0.055±.002
Mean forward speed during peristalsis (mm/s)	0.32±.01	0.33±.01
On temporal gradients		
Turn frequency (min^{-1})		
Warming	3.2±0.1**	2.6±0.1 **
Cooling	3.8±0.1**	3.8±0.1 **
Size of first head sweep during turns		
Warming	53°±1° *	53°±2° **
Cooling	57°±1° *	60°±2° **

Figure 5.6: Individual second instar larvae were placed on large Petri plates (20 cm x 20 cm) either with superposed spatial temperature gradient or spatially uniform temporal gradient and tracked using similar methods as described elsewhere [4,24]. At least 20 animals were used for each measurement. Each measurement represents the mean ± one standard error. On spatial gradients (0.3°C/cm), individual larvae were initially placed near 17°C, and their trajectories towards higher temperatures were analyzed. Thermotaxis speed indicates the mean rate of ascent up the temperature gradient towards warmer temperatures. Mean forward speed during periods of persistent forward movement was also measured. On temporal gradients, larvae were subjected to sinusoidal temperature waveforms, 20°C offset, 1°C amplitude, 6 min period. The frequency of turning decisions and the mean size of the first head sweep in each turning decision was quantified during both warming and cooling phases of the temperature stimulus. * and ** indicates case in which each statistic differs between warming and cooling at $P<0.05$ and $P<0.005$, respectively.

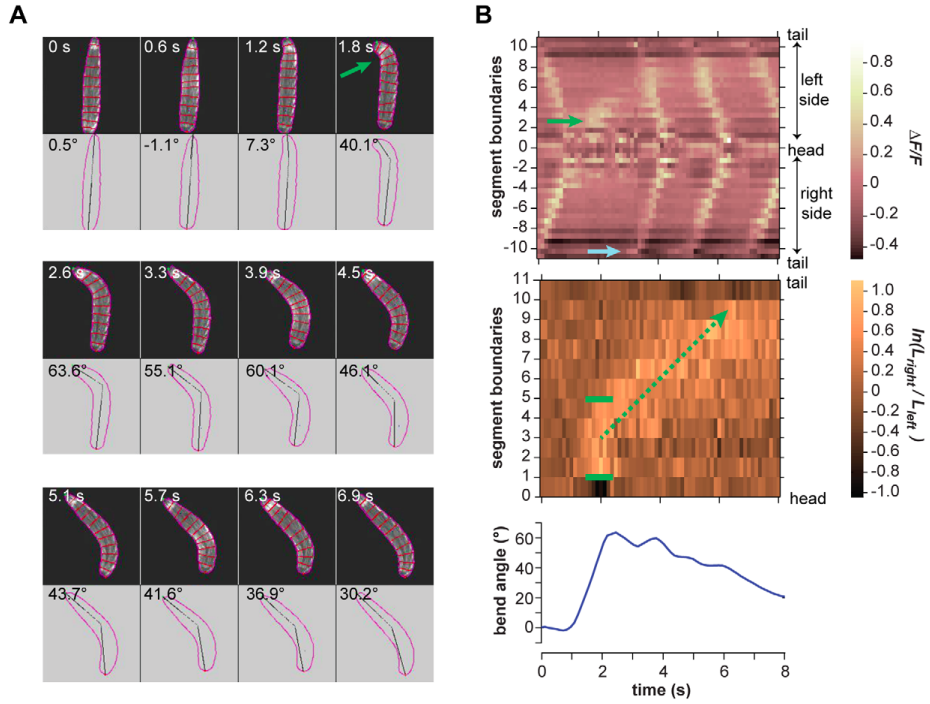

Figure 5.7: Turning decisions with small head sweeps. A. Video frames of an example small head sweep during cooling. Upper panel in each video frame shows fluorescence image. Outline and boundaries between segments are shown in red. Lower panel in each video frame shows the perimeter, centerline, and body bend angle as analyzed by machine vision software. Green arrow shows the asymmetric bend that is flagged as a head sweep. B. (Upper panel) Kymograph of fluorescence intensity within body segments for the video segment shown in A. Green arrow shows the increase in fluorescence intensity on the left side of the animal, signifying the leftward head sweep. Blue arrow shows the increase in fluorescence intensity in the A8 segment, signifying the resumption of peristalsis at the tail. (Middle panel) Kymograph of the logarithm of the ratio between the lengths of segment boundaries on the left side and right side of the animal. Green brackets indicate the margins of the region of asymmetric contraction, positive values signifying the leftward bend. Green arrow shows the retrograde progression of the region of asymmetric contraction during the four subsequent peristalsis waves. (Lower panel) Time course of body bend angle, operationally defined to flag reorientation maneuvers as described in Materials and Methods, shows the initial rise that signifies the leftward head sweep and gradual decline as subsequent peristalsis waves straighten the body.

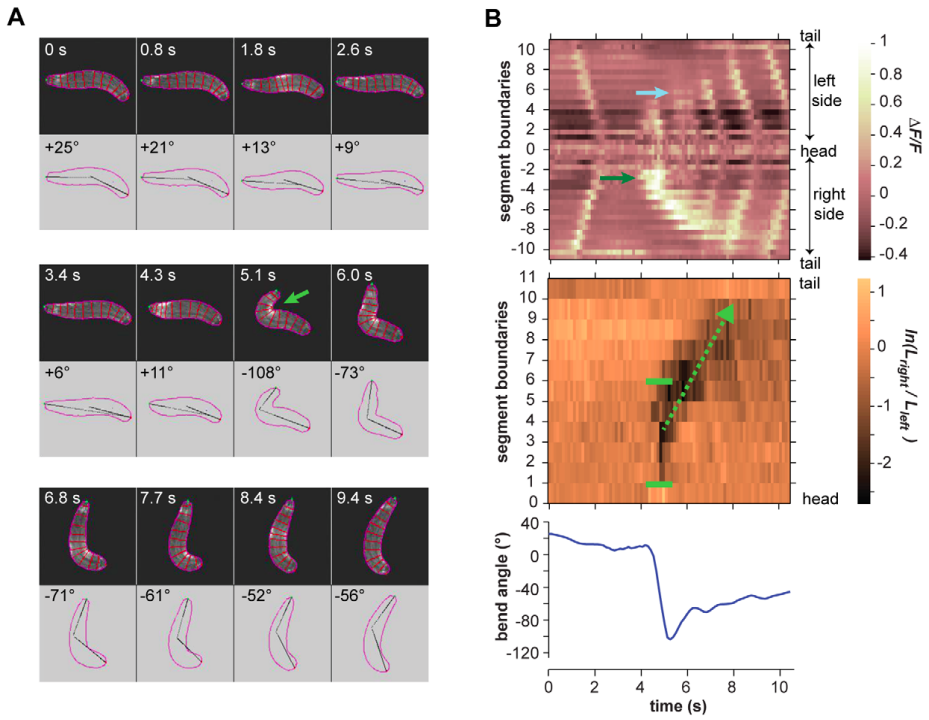

Figure 5.8: Turning decisions with large head sweeps. A. Video frames of an example large rightward head sweep during cooling. Upper panel in each video frame shows fluorescence image. Outline and boundaries between segments are shown in red. Lower panel in each video frame shows the perimeter, centerline, and body bend angle as analyzed by machine vision software. Green arrow shows the asymmetric bend that is flagged as a head sweep. B. (Upper panel) Kymograph of fluorescence intensity within body segments for the video segment shown in A. Green arrow shows the greater increase in fluorescence intensity on the right side of the animal, signifying the rightward head sweep. Blue arrow shows the increase in fluorescence intensity in the A3 segment, signifying the resumption of peristalsis near the bend. (Middle panel) Kymograph of the logarithm of the ratio between the lengths of segment boundaries on the left side and right side of the animal. Green brackets indicate the margins of the region of asymmetric contraction, negative values signifying the rightward bend. Green arrow shows the retrograde progression of the region of asymmetric contraction during subsequent peristalsis waves. (Lower panel) Time course of body bend angle, operationally defined to flag reorientation maneuvers as described in Materials and Methods, shows the initial drop that signifies the rightward head sweep and gradual rise as subsequent peristalsis waves straighten the body.

do this, we quantified asymmetric contraction by measuring the logarithm of the length ratio between the left and right boundaries of the opposing quadrants within each body segment: $\ln(L_{right}/L_{left})$. This logarithm is roughly zero during the peristalsis that accompanies forward movement because the left and right sides of each segment contract and expand simultaneously. During head sweeps, the logarithm of the length ratio of the body segments within the pivot will increase to positive values or decrease to negative values for leftward and rightward sweeps, respectively. We found remarkable consistency in the usage of segments during head sweeps. Neither the anterior and posterior extents of asymmetric contraction, nor the center of the pivot, depended on the size or direction of head sweeps, whether they were initiated during the cooling or warming phases of thermosensory input, or whether one or more head sweeps were involved in each turning decision (Figure 5.5 and Video 2; Figure 5.7 and Video 3; Figure 5.8 and Video 4; Figure 5.9 and Video 5; Figure 5.10A). All head sweeps are centered on the A1 segment, which undergoes the peak asymmetric contraction between the left and right sides. The T3, A2 and A3 segment, although exhibiting smaller amounts of asymmetric contraction than A1, also appear to contribute to the pivot (Figure 5.10A). Taken together, these observations suggest parsimony in the higher-order commands that evoke head sweeps in turning decisions. The brain only needs to tell one group of segments (T3 through A3) how much to bend. We found that larvae complete reorientation maneuvers by using peristalsis, gradually straightening their bodies along the new direction for forward movement. When peristalsis resumes after small head sweeps (body bend angles $< 90^{\circ}$), the first wave of contraction tends to be initiated at the tail (Figure 5.5 and Video 2; Figure 5.7 and Video 3; Figure 5.10B), just as in normal forward movement (Figure 5.2). With each subsequent wave of contraction, all of which continue to be initiated at the tail, ,2 additional body segments make their way around the bend. Thus, the region of asymmetric contraction gradually propagates posteriorly, starting from the initial bend at T3-A3 and moving toward the tail until, after 3-4 peristalsis wave, the entire larva has made its way around the bend (Figure 5.5B; Figure 5.7B). At this point, the straightened larva continues forward movement in its new direction.

When peristalsis resumes after large head sweeps, the first wave of contraction

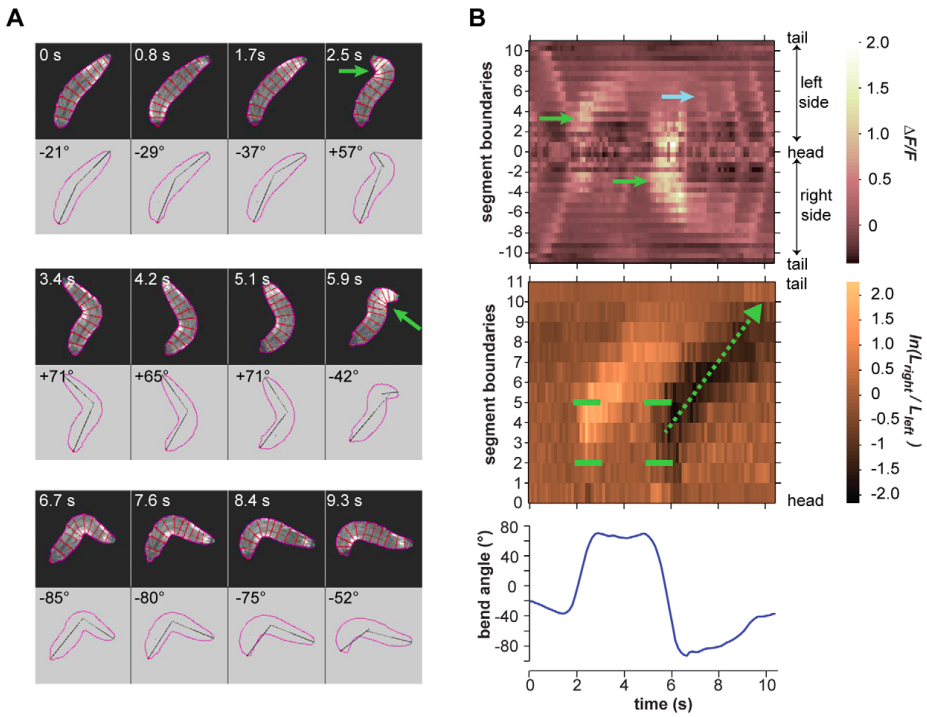

Figure 5.9: Turning decisions with multiple head sweeps. A. Video frames of a turning decision during cooling in which two head sweeps were executed in rapid succession. Upper panel in each video frame shows fluorescence image. Outline and boundaries between segments are shown in red. Lower panel in each video frame shows the perimeter, centerline, and body bend angle as analyzed by machine vision software. Green arrows show the asymmetric bends that are flagged as head sweeps. B. (Upper panel) Kymograph of fluorescence intensity within body segments for the video segment shown in A. Green arrows show the greater increase in fluorescence intensity, first on the left side then the right side of the animal, signifying the leftward and rightward head sweeps. Blue arrow shows the increase in fluorescence intensity in the A3 segment, signifying the resumption of peristalsis near the bend.(Middle panel) Kymograph of the logarithm of the ratio between the lengths of segment boundaries on the left side and right side of the animal. Green brackets indicate the margins of the region of asymmetric contraction, positive values signifying the leftward bend and negative values signifying the rightward bend. One peristalsis wave occurs after the leftward head sweep. Green arrow shows the retrograde progression of the region of asymmetric contraction that straighten the body during three peristalsis waves after the rightward head sweep. (Lower panel) Time course of body bend angle, operationally defined to flag reorientation maneuvers as described in Materials and Methods, shows the initial rise that signifies the leftward head sweep and drop that signifies the subsequent rightward head sweep.

tended to be initiated near the region of asymmetric contraction (Figure 5.8 and Video 4). Thus, the peristalsis of the portion of the larva that is anterior to the pivot appears to pull posterior segments into the region of asymmetric contraction. Each subsequent wave of contraction works the same way, being initiated within the bent portion of the larva, gradually pulling body segments around the original pivot point. After 4-6 peristalsis cycles, the entire larva makes its way around the original pivot point with a new direction for forward movement with straightened body (Figure 5.8 and Video 4).

As shown in Figure 5.9 and Video 5, a reorientation maneuver can be said to involve multiple head sweeps when they are initiated in rapid succession without enough intervening peristalsis waves to straighten the larva body. Thus, in the maneuver shown in Figure 5.9 and Video 5, in which only one peristalsis wave is initiated between the head sweeps, the direction chosen by the first head sweep was "rejected" whereas the direction chosen by the second head sweep was "accepted" and became the direction of the subsequent run. Earlier it was shown that the probability of rejecting a head sweep during larval cold-avoidance behavior was raised (/lowered) if the larva experienced cooling (/warming) during the head sweep [4]. By examining the resumption of peristalsis after head sweeps of different size, we found that the first wave of contraction was always initiated either at the tail (more probable for smaller head sweeps) or within the region of asymmetric contraction (more probable for larger head sweeps) (Figure 5.10B). In addition, more peristalsis cycles are required to straighten the larva after larger head sweeps (Figure 5.10C).

5.6 Discussion

Animals execute complex behaviors by breaking tasks into discrete steps that can be accomplished through the deployment of motor programs. Understanding orientation behavior, how an animal senses and moves with respect to stimulus gradients in its environment, has long been a classic problem in neuroethology [16]. Classic studies in the phototactic behavior of maggot larvae, for example, identified and explored how movement patterns like head sweeping allow these small animals to change their direction of movement with respect to light sources [5].

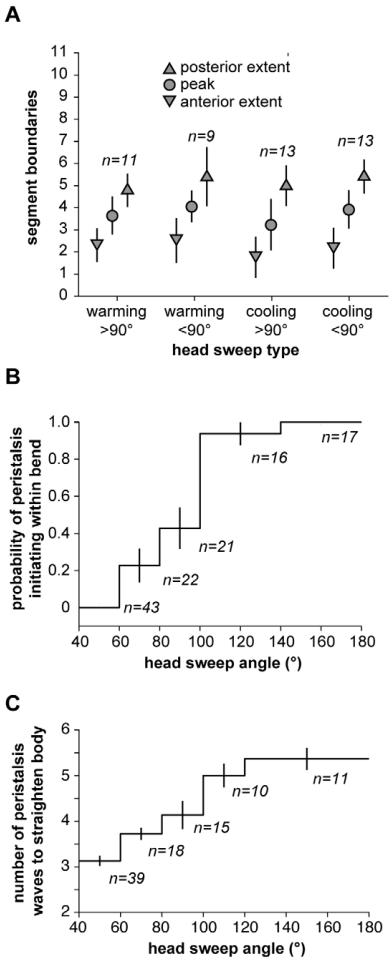

Figure 5.10: Consistency in segment dynamics during turning decisions. A. Region of asymmetric contraction for large ($> 90°$) and small ($< 90°$) head sweeps during warming and cooling. For different classes of head sweeps, the anterior extent (inverted triangle), posterior extent (triangle) and peak position of asymmetric contraction (circle) were flagged in kymographs as shown in Figure 5.5B, 6B, 7B, and 8B. Data points represent the mean $\pm$ s.d. of each set of measurements. B. The probability of initiating peristalsis waves within the bent portion of the larva increases with the size of head sweeps. The number of measurements for each data point is shown in italics. Error bars represent one standard error. C. Larger reorientations require more peristalsis waves to straighten the larva's body. The number of measurements for each data point is shown in italics. Error bars represent one standard error.

However, comprehensive understanding of the neural basis of orientation behavior necessitates using genetically and physiologically tractable model organisms like *Drosophila*.

In an earlier study, we showed that decision-making during larva thermotaxis occurs during the reorientation maneuvers that separate successive periods of forward movement [4]. Here, we used the direct visualization of segment dynamics with high-resolution fluorescence microscopy to characterize the motor programs that drive thermotaxis in transgenic *Drosophila* larvae with fluorescently labeled muscle fibers. We show that the initiation, execution, and completion of these reorientation maneuvers are carried out by alternating deployment of two types of motor programs: one for asymmetric contraction that drives anterior bending (head sweeping) and one for peristalsis that drives forward movement. The high degree of stereotypy in each motor program suggests that navigational strategy can be executed with a relatively small set of commands that emanate from the larval brain. First, the brain uses thermosensory input to trigger the transition from peristaltic forward movement to head sweeping movement that signifies the onset of each reorientation maneuver. During the initial bending movements of a head sweep, the brain specifies the amplitude of each head sweep to be carried out by one group of body segments. Finally, to complete the reorientation maneuver, the larva returns to the motor program for peristalsis to straighten the body along the new direction for forward movement. We have also seen that, to complete a turn, peristalsis can resume from different positions depending on the size of the head sweep. It is unclear why this happens, but our observations do demonstrate that peristalsis can be initiated at different points along the body. One reason might be to avoid disrupting the angle of reorientation defined by the angular size of large head sweeps: if peristalsis were initiated at the tail after a large head sweep, the position of the pivot might be pushed forward when the peristalsis reaches the pivot, perhaps increasing the angle of the reorientation beyond the size of the original head sweep. The ability to initiate peristalsis in different segments depending on the degree of body bend might point to a role for sensory feedback in the motor circuit. Proprioceptive feedback has recently been shown to play an essential role in generating peristalsis in the *Drosophila* larva [10,17,18]. *Drosophila* larvae also exhibit phototaxis and chemotaxis, but the navigational strategies have yet to be defined in the same detail as larval thermotaxis [19-22].

Comparative analysis of navigational strategies and motor programs during different modes of navigation would illuminate whether shared sensorimotor pathways are used during different navigational modes. Here, we focused on the two motor programs that build thermotaxis, but other motor programs appear to be used during other types of behavioral response, such as reverse crawling, hunching, and rolling movements that are used during nociceptive and rapid avoidance responses [21]. Elucidating the complete set of motor programs that can be carried out by the *Drosophila* larva will yield the building-blocks of its total behavioral repertoire. Elucidating the pathways by which these motor programs are triggered by environmental stimuli will yield a complete understanding of brain and behavior in this small animal. We note that the progression of work on thermotactic navigation in the *Drosophila* larva parallels earlier studies of bacterial chemotactic navigation. The biased-random walk strategy of bacterial chemotaxis was originally established by using a tracking microscope to follow the movements of individual bacteria as they navigated chemical gradients: *E. coli* swims by alternating periods of forward movement (runs) with erratic reorientation movements (tumbles), and the bacterium postpones tumbles when it senses increasing amounts of chemoattractant in its surroundings [6]. A tracking microscope was also used to establish that the larva navigates by alternating periods of forward movement with turning decisions [4]. A recent study of bacterial chemotaxis, which parallels this study, used advances in fluorescent labeling and video microscopy to directly visualize how the detailed movements of individual bacterial flagella contribute to the initiation, execution, and conclusion of tumbles [23]. Both bacteria and *Drosophila* larva use essentially two motor programs to navigate. By regulating the transition from forward movement to reorientation movement in response to sensory conditions, both organisms lengthen runs that happen to be pointed in favorable directions. The head sweeping that characterizes navigational decisions during larval thermotaxis allows the animal to explore an additional axis during reorientation, enabling it to point more runs towards favorable directions. The *Drosophila* larva does not improve its navigation beyond bacterial navigation by using a larger repertoire of motor programs, but by using both motor programs to more efficiently assess preferred directions in its environment.

5.7 Materials and Methods

5.7.1 Fly strains

To quantify the parameters of thermotactic strategy as shown in Figure 5.6 we followed methods described in our earlier study [4]. Our wild-type strain was Canton S. To quantify muscle dynamics, we used *w;Mhc-GFPc110/CyO* second instar larvae. Larvae were raised at $25^{\circ}C$ on grape juice plates with yeast paste. Individual larvae were removed from the plates, rinsed in distilled water, and transferred to the agar surface of the tracking and imaging setup shown in Figure 5.2.

5.7.2 Image acquisition and tracking

Individual second instar larvae were placed on flat agar surfaces. The agar (1% agarose in distilled water) had been poured onto thin black anodized aluminum plates (8.3 x 8.3 x 0.16 cm), forming a layer approximately 2 mm thick. The square agar plates were placed under a microscope (Eclipse LV100, Nikon), and blue light (450-490 nm) was shone onto a single larva, with the resulting GFP signal (500-550 nm) from larval muscles imaged onto a CCD camera (CoolSNAP EZ, Photometrics), with images acquired at 8 Hz. Unrestrained larvae were free to crawl and exhibit behavior on the agar surface, and were kept in the field of view of the camera via feedback to a motorized x-y stage (MAC6000, Ludl Electronic Products). Image acquisition, motorized stage feedback, and temperature control (see below) were all integrated into customized software written in LabVIEW (National Instruments). For each acquired image, a binary-thresholded version was generated, with the larval center of mass position relative to the image center used to determine the necessary direction and magnitude of the stage movement. Raw larval images, stage positions, and frame times were all recorded. Temperature control Approximate larval temperature during experiments was measured using a K-type thermocouple embedded just under the agar surface. The temperature was controlled with a custom-built feedback circuit consisting of a PID controller and H-bridge amplifier (FTC200 and FTX700, Ferrotec) driving a TEC device (CP1-12710, Thermal Enterprises). The TEC pumped heat (in either direction) between a copper block with the stage and agar surface atop, and a circulating liquid coolant reservoir. This setup allowed rapid heating and cooling of the larva being tracked,

and its response to temperature changes could be readily discerned. Temperature was sine-wave modulated, with $1^{\circ}C$ amplitude and 2 min period with $15^{\circ}C$ offset. Note that the temporal gradients that we used on the high-resolution imaging setup differed from the temporal gradients described in Figure 5.6, where we used higher absolute temperatures and shallower gradients to compare the cold-avoidance response of the transgenic strain to our wild-type strain.

5.7.3 Image analysis

Image analysis operations illustrated in Figure 5.1B were performed with custom software written in MATLAB. For each video frame, the boundary of the larva and positions of head and tail were located as follows. First, the image was thresholded to produce a binary image. The binary image was smoothed using erosion and dilation, image processing filters available in MATLAB. The largest boundary in the binary image corresponding to the perimeter of the larva body was determined, and further smoothed with a Gaussian filter with width corresponding to 0.5% of boundary length. The curvature of the boundary was computed with a sliding window (20% of the total boundary length), and the head and tail were identified as the two local maxima. The head and tail were distinguished from each other by proximity to their locations in the previous frame. In the first frame of each video, the distinction was made with user input. Next, an operational definition of body bend angle was used to detect the onset of head sweeps. First, we identified the body centerline as the midpoints of the lines joining corresponding points on the left and right of the larva body. Three points were marked along the body centerline at J, K, and L of total length (Figure 5.1B). We quantified body bend as the angle between the line segment joining the tail to the midpoint and the line segment joining the head to the L-point (marked as h in Figure 5.1B). Leftward and rightward head sweeps are indicate by positive and negative angles, respectively. We flagged each head sweep when the magnitude of this angle exceeded 40u. Note that this definition of body bend angle will only be accurate when the bend lies between the L-point and the midpoint, but suffices for flagging the beginning and end of reorientation maneuvers. Finally, in each video frame the user clicked on the 20 points where segment boundaries intersect the boundary of the larva. This operation split the larva image into three thoracic (T1...T3) and eight abdominal

(A1...A8) segments. The left and right boundaries of each segment could be directly quantified as a metric of segment contraction. Alternatively, each segment was split into four quadrants (anterior left, anterior right, posterior left, posterior right) so that fluorescence intensity could be computed from the mean pixel value in each quadrant. The points between segment boundaries were used to define the coordinate system for analyzing body segment dynamics as shown in the schematic of the larva body in Figure 5.3B.

5.7.4 Statistical procedures

In Figure 5.4, the slope of the best fit line and correlation coefficient, r2, were computed with Ordinary Least Squares simple linear regression using MATLAB. In Figure 5.10A, for each head sweep, the anterior and posterior extent of asymmetric contraction, as well as the position of peak asymmetry were recorded. The mean and standard deviations were computed using MATLAB. In Figure 5.10B, for each head sweep, the peak body bend angle and whether or not peristalsis reinitiated from the bent region was recorded. Within each bin for the angle, the total number of head sweeps, n_i, and the number of times peristalsis reinitiated from the bent region, m_i , were used to compute probability and standard error. In Figure 5.10C, for each head sweep, the peak body bend angle and the number of peristalsis pulses needed was recorded. Within each bin for the angle, the mean and standard deviations were computed using MATLAB. For Figure 5.6, thermotaxis speed on spatial gradients was calculated by taking the mean position of the population as a function of time and performing a linear fit of the resulting data. The population position stabilized as larvae reached their preferred temperature; data for times after this occurred were not used. For mean forward speed during peristalsis, we averaged the speed of larvae at each acquired image throughout the recorded Video, excepting larvae in the midst of turning decisions. For temporal gradient thermotaxis, we defined warming (/cooling) to occur when the rate of change of the agar surface temperature was greater (/less) than $0.001^{\circ}C$/sec. We counted the total number of reorientations occurring during heating and cooling, then divided by the total time that warming and cooling occurred during an experiment, which yielded the turn frequency. We also examined the head sweeps that occurred during reorientation events, extracting the angle of the first head sweep,

and then averaging all such events for both warming and cooling reorientations.

5.8 Videos

5.8.1 Video 1

Right panel shows video of freely crawling larva corresponding to the video frames shown in Figure 5.3A. Left panel shows kymograph of fractional changes in fluorescence intensity during the video as shown in lower panel of Figure 5.3B.

5.8.2 Video 2

Right panel shows video of larva exhibiting a small leftward head sweep corresponding to the video frames shown in Figure 5.5A. Upper left panel shows kymograph of fractional changes in fluorescence intensity as shown in upper panel of Figure 5.5B. Lower left panel shows kymograph of the logarithm of the ratio between right and left boundary lengths of each segment as shown in the middle panel of Figure 5.5B.

5.8.3 Video 3

Right panel shows video of larva exhibiting a small leftward head sweep corresponding to the video frames shown in Figure 5.7A. Upper left panel shows kymograph of fractional changes in fluorescence intensity as shown in upper panel of Figure 5.7B. Lower left panel shows kymograph of the logarithm of the ratio between right and left boundary lengths of each segment as shown in the middle panel of Figure 5.7B.

5.8.4 Video 4

Right panel shows video of larva exhibiting a large rightward head sweep corresponding to the video frames shown in Figure 5.8A. Upper left panel shows kymograph of fractional changes in fluorescence intensity as shown in upper panel of Figure 5.8B. Lower left panel shows kymograph of the ratio between right and left boundary lengths of each segment as shown in the middle panel of Figure 5.8B.

5.8.5 Video 5

Right panel shows video of larva exhibiting a leftward then rightward head sweep corresponding to the video frames shown in Figure 5.9A. Upper left panels shows kymograph of fractional changes in fluorescence intensity as shown in upper panel of Figure 5.9B. Lower left panels shows kymograph of the ratio between right and left boundary lengths of each segment as shown in the middle panel of Figure 5.9B.

5.9 Acknowledgments

We thank members of the Garrity and Samuel labs for useful discussions. We thank Ashley Carter for help with programming the tracking stage. We thank Richa Dixit, Marta Zlatic, and Ben de Bivort for comments on the manuscript. We thank two anonymous reviewers for helpful suggestions in improving the manuscript.

5.10 Author Contributions

Conceived and designed the experiments: SL MK PG AS EK. Performed the experiments: SL KS AT MK. Analyzed the data: SL KS AT. Contributed reagents/materials/analysis tools: EK MK MG. Wrote the paper: AS.

5.11 References

1. Rosenzweig M, Brennan KM, Tayler TD, Phelps PO, Patapoutian A, et al. (2005) The *Drosophila* ortholog of vertebrate TRPA1 regulates thermotaxis. Genes Dev 19: 419-424.

2. Rosenzweig M, Kang K, Garrity PA (2008) Distinct TRP channels are required for warm and cool avoidance in *Drosophila* melanogaster. Proc Natl Acad Sci U S A 105: 14668-14673.

3. Liu L, Yermolaieva O, Johnson WA, Abboud FM, Welsh MJ (2003) Identification and function of thermosensory neurons in *Drosophila* larvae. Nat Neurosci 6: 267-273.

4. Luo L, Gershow M, Rosenzweig M, Kang K, Fang-Yen C, et al. (2010) Navigational decision making in *Drosophila* thermotaxis. J Neurosci 30: 4261-4272.

5. Holmes SJ (1905) The selection of random movements as a factor in phototaxis. Journal of Comparative Neurology and Psychology 15: 98-112.

6. Berg HC, Brown DA (1972) Chemotaxis in Escherichia coli analysed by threedimensional tracking. Nature 239: 500-504.

7. Pierce-Shimomura JT, Morse TM, Lockery SR (1999) The fundamental role of pirouettes in Caenorhabditis elegans chemotaxis. J Neurosci 19: 9557-9569.

8. Ryu WS, Samuel AD (2002) Thermotaxis in Caenorhabditis elegans analyzed by measuring responses to defined Thermal stimuli. J Neurosci 22: 5727-5733.

9. Crisp S, Evers JF, Fiala A, Bate M (2008) The development of motor coordination in *Drosophila* embryos. Development 135: 3707-3717.

10. Hughes CL, Thomas JB (2007) A sensory feedback circuit coordinates muscle activity in *Drosophila*. Mol Cell Neurosci 35: 383-396.

11. Berrigan D, Lighton JR (1993) Bioenergetic and kinematic consequences of limblessness in larval Diptera. J Exp Biol 179: 245-259.

12. Dixit R, Vijayraghavan K, Bate M (2008) Hox genes and the regulation of movement in *Drosophila*. Dev Neurobiol 68: 309-316.

13. Neckameyer WS (2010) A trophic role for serotonin in the development of a simple feeding circuit. Dev Neurosci 32: 217-237.

14. Sitaraman D, Zars M, Laferriere H, Chen YC, Sable-Smith A, et al. (2008) Serotonin is necessary for place memory in *Drosophila*. Proc Natl Acad Sci U S A 105: 5579-5584.

15. Rodriguez Moncalvo VG, Campos AR (2009) Role of serotonergic neurons in the *Drosophila* larval response to light. BMC Neurosci 10: 66.

16. Fraenkel GS, Gunn DL (1940) The orientation of animals: kineses, taxes and compact reactions. Oxford: The Clarendon Press. vi, [2] 352 p. incl. tables, diagrs. plates. p.

17. Song W, Onishi M, Jan LY, Jan YN (2007) Peripheral multidendritic sensory neurons are necessary for rhythmic locomotion behavior in *Drosophila* larvae. Proc Natl Acad Sci U S A 104: 5199-5204.

18. Cheng LE, Song W, Looger LL, Jan LY, Jan YN (2010) The role of the TRP channel NompC in *Drosophila* larval and adult locomotion. Neuron 67: 373-380.

19. Louis M, Huber T, Benton R, Sakmar TP, Vosshall LB (2008) Bilateral olfactory sensory input enhances chemotaxis behavior. Nat Neurosci 11: 187-199.

20. Mazzoni EO, Desplan C, Blau J (2005) Circadian pacemaker neurons transmit and modulate visual information to control a rapid behavioral response. Neuron 45: 293-300.

21. Hwang RY, Zhong L, Xu Y, Johnson T, Zhang F, et al. (2007) Nociceptive neurons protect *Drosophila* larvae from parasitoid wasps. Curr Biol 17: 2105-2116.

22. Xiang Y, Yuan Q, Vogt N, Looger LL, Jan LY, et al. (2010) Light-avoidancemediating photoreceptors tile the *Drosophila* larval body wall. Nature 468: 921-926.

23. Turner L, Ryu WS, Berg HC (2000) Real-time imaging of fluorescent flagellar filaments. J Bacteriol 182: 2793-2801.

24. Clark DA, Gabel CV, Lee TM, Samuel AD (2007) Short-term adaptation and temporal processing in the cryophilic response of Caenorhabditis elegans. J Neurophysiol 97: 1903-1910.

6

Appendix 3: Controlling airborne cues to study small animal navigation

6.1 Authors

Marc Gershow, Matthew Berck, Dennis Mathew, Linjiao Luo, Elizabeth A. Kane, John R. Carlson, Aravinthan D. T. Samuel

6.2 Publication note

A version of this appendix was published as the following article: Gershow M, Berck M, Mathew D, Luo L, Kane EA, Carlson JR, Samuel AD. Controlling airborne cues to study small animal navigation. *Nat Methods*. 2012 Jan 15;9(3):290-6.

6.3 Abstract

Small animals such as nematodes and insects analyze airborne chemical cues to infer the direction of favorable and noxious locations. In these animals, the study

of navigational behavior evoked by airborne cues has been limited by the difficulty of precisely controlling stimuli. We present a system that can be used to deliver gaseous stimuli in defined spatial and temporal patterns to freely moving small animals. We used this apparatus, in combination with machine-vision algorithms, to assess and quantify navigational decision making of *Drosophila melanogaster* larvae in response to ethyl acetate (a volatile attractant) and carbon dioxide (a gaseous repellant).

6.4 Introduction

Olfaction is a sophisticated sensory modality. Odor plumes from sources in an animal's environment are carried and mixed by chaotic air currents before reaching an animal's olfactory organ. From a complex olfactory signal, and the resulting time-varying activity of a panel of olfactory neuronal types, an animal strives to locate and discriminate odor sources [1-3].

Olfactory computation may be studied using small invertebrates like *Caenorhabditis elegans* and *D. melanogaster*, which have small circuits and simple behaviors and are amenable to genetic manipulation [4,5]. Quantitative behavioral analysis, an important step in defining olfactory computations, is complicated by the difficulty of delivering precise airborne stimuli to freely moving animals. Classical behavioral assays for these animals quantify migration toward or away from droplets of odor [6-9]. In these assays, evaporation, convection and diffusion create spatially varying concentration gradients that change over time during each experiment. Droplet-based assays can be improved by calibrating the odor profile in closed plates using infrared spectroscopy [8,9]; however, gases such as carbon dioxide (CO_2) that are not liquid at room temperature cannot be used, spatial or temporal gradients cannot be precisely defined, the odor profile cannot be held stable in time, and a relatively small experimental arena must be used, leading to lower throughput. An alternative is to deliver waterborne stimuli using microfluidic devices engineered to the shape and movements of each animal. Such devices constrain behavior to their specific geometries [10-12] and do not easily accommodate many animals including insect larvae. We present a device (Figure 6.1) that allows us to deliver airborne cues in defined spatial and temporal gradients to freely behaving animals. An array of miniature solenoid

valves injects odorant cues into a laminar airflow directed across an experimental arena. The amount of airborne cue injected at each point can be dynamically regulated during each experiment. This device generated long-lasting, stable and highly reproducible spatiotemporal gradients of any gas, including CO_2, a salient cue for *D. melanogaster* and *Anopheles* sp. mosquito [13,14], and features a large experimental arena that allows many small invertebrates to be studied simultaneously for extended periods of time. Using our device, in combination with custom machine-vision software, the multianimal gait and track (MAGAT) analyzer (Figure 6.2 and Supplemental Figure 6.6), we quantified navigational decision making of *D. melanogaster* larvae in response to airborne cues with higher precision and throughput than has been possible with earlier methods. We examined *D. melanogaster* larva chemotaxis to an airborne attractant (ethyl acetate) and repellant (CO_2) and discovered similarities between the larva's response to these gaseous cues and its navigation of thermal gradients.

6.5 Results

6.5.1 Gradient generation

Our device creates airborne gradients in a square arena, 25 cm on a side, allowing extended observation of many animals per experiment and surpassing the throughput of single animal methods [8,15]. A slow laminar airflow (1.2 cm s^{-1}) is directed along the *y* axis of the arena. A row of miniature solenoid valves spaced 8 mm apart is used to generate gradients along the *x* axis. When each valve is open, a dose of gaseous cue is injected at a specific point along the *x* axis into the airflow. The opening of the valves and the odor-carrying airflow may be used to generate defined spatial and temporal gradients of any gaseous cue (see Supplementary Methods).

To characterize the gradients within the arena, we substituted its glass lid with an aluminum plate fitted with miniature gas detectors. We imposed a linear gradient by programming the fraction of time each valve was open to be in proportion to its position along the *x* axis. With either ethyl acetate or CO_2 (Figure 6.1b,c), we found that the deviation from linearity was <3% of the mean concentration in the region in which the behavioral experiments were done.

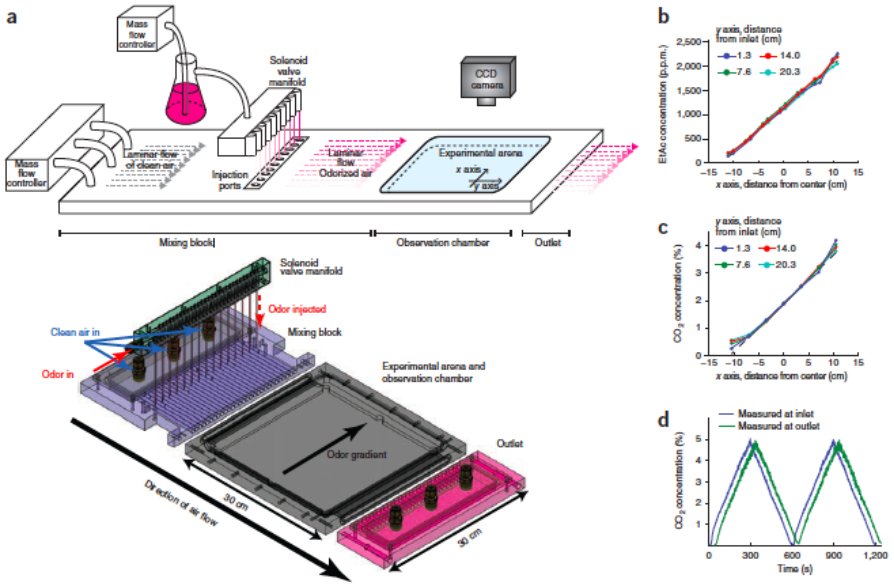

Figure 6.1: Apparatus design and performance. (a) Schematic of the device (top). Clean airflow into the rear of the apparatus is regulated by a mass flow controller. For ethyl acetate experiments, a second mass flow controller controls airflow through a bubbler containing ethyl acetate. Odorized air is injected into points across the laminar airflow within a mixing block using a solenoid valve manifold. The laminar airflow odorized with a spatial gradient of ethyl acetate in the mixing block then passes into an observation chamber containing an experimental arena with transparent ceiling, allowing visualization of animal behavior inside the arena with a charge-coupled device (CCD) camera. Semitransparent isometric projection (bottom) of custom-machined components of the apparatus, including solenoid valve manifold, mixing block, experimental arena and observation chamber, and outlet. Direction of air flow (y axis) and gradient (x axis) are indicated. Odor gradient' arrow points to higher concentration in experiments described here. (b,c) Measurement of precision of linear spatial gradients of ethyl acetate (EtAc; b) or CO_2 (c) in the experimental arena. Gas concentration was measured at specific points in the experimental arena across the airflow (arena x axis) at indicated distances from the inlet (arena y axis). (d) CO_2 concentration at inlet and outlet during a 10-min temporal triangle ramp from 0% to 5% CO_2.

To generate temporal gradients, we mixed odor into the airstream before it entered the device, controlling the odor flow rate into the airstream while monitoring odor concentration at the chamber inlet and outlet (Supplementary Methods and Supplementary Figure **??** and Figure 6.1d). The concentration is constant along the x axis, as the odor is mixed into the airstream before entry into the flow tubes that are used to define a spatial gradient. Along the y axis, the concentration varies as the time-varying odor profile is pushed across the chamber by the moving air flow. We measured a time lag between the detection of an odor change in the inlet and the outlet that corresponds to the flow rate of the gas in the chamber. Thus, the concentration at any point in the chamber is given by $C(y,\mathrm{t}) = C_{inlet}(\mathrm{t}-t_d - y/v_f)$, where v_f is the flow speed in the chamber and td is the time it takes gas to flow from the inlet to the flow chamber entrance.

6.5.2 Behavioral analysis

The trajectories of crawling *D. melanogaster* larvae are characterized by periods of forward movement (runs) that are interrupted by turns. We have previously used a high-resolution tracking microscope to follow individual *D. melanogaster* larvae on temperature gradients [15]. We have shown that a larva biases the frequency, direction and size of turns to move toward favorable temperatures. Here we sought to achieve the same resolution of behavioral analysis in a multianimal experiment. To do this, we developed the MAGAT analyzer software package to follow many larvae in parallel (Video 1, Supplementary Figure 6.6; software updates will be available at https://github.com/samuellab/MAGATAnalyzer) and determine the behavioral state of each larva (running, turning and sweeping the head) at all times (Figure 6.2a,b and Supplementary Methods and Videos 2-6). The MAGAT analyzer quantifies the navigational performance of individual *D. melanogaster* larvae. By collecting navigational statistics across populations of *D. melanogaster* larvae, we uncovered behavioral strategies.

We characterized the navigational strategies of *D. melanogaster* larvae in response to ethyl acetate and CO_2 using defined spatial and temporal gradients. First, we examined the response to ethyl acetate, a volatile attractant [16], in linear spatial gradients with defined steepness [6]. We placed second instar Canton-S larvae in the middle of each gradient and quantified the resulting trajectories (Fig-

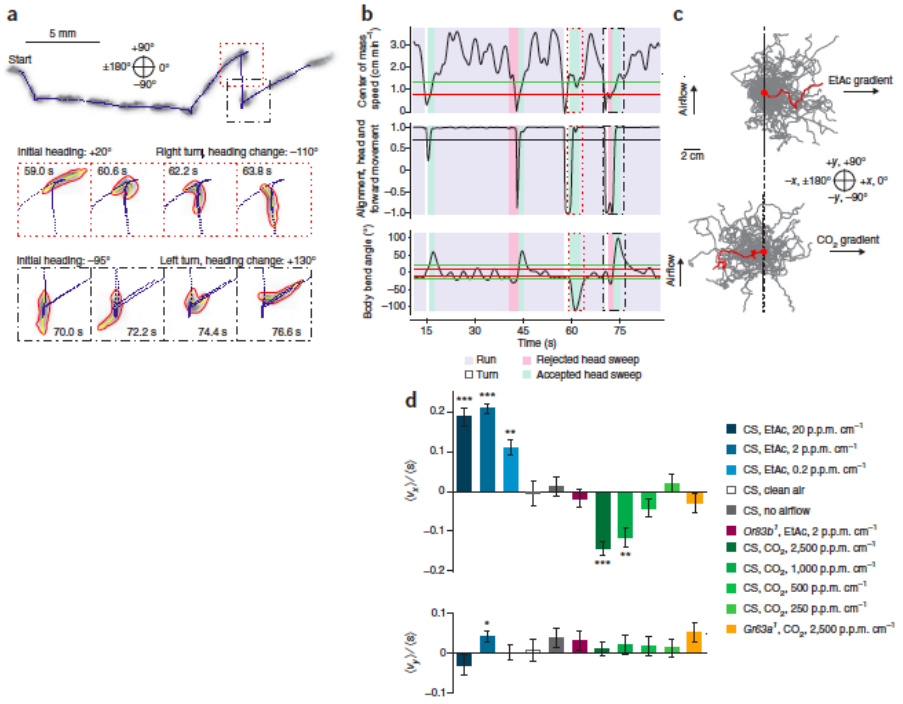

Figure 6.2: Response to spatial gradients. (a) Image sequence of wild-type second instar larva crawling from left to right over 80 s (top). Blue dots, midpoint of larva every 200 ms. Still frames (bottom) highlight two turns in which larva achieved heading changes. Red and yellow lines, contour and midline of larva, respectively. (b) Metrics derived from the track in a and used to determine behavioral state over time. Dotted and dashed boxes outline times for corresponding frames in a. Horizontal lines, hysteretic thresholds for run determination (top), threshold for run determination (middle) and hysteretic thresholds for head sweep determination (bottom). (c) Trajectories (40 selected for each condition) of larvae navigating linear gradients of ethyl acetate (top; 2 p.p.m. cm^{-1}) and CO_2 (bottom; 2,500 p.p.m. cm^{-1}). Trajectories start at same point (red dot). Single trajectories are red. (d) Navigational indices for wild-type and mutant larvae navigating gradients of varying concentrations of ethyl acetate and CO_2. Values are mean ± s.e.m. *** and **, rejection of hypothesis that navigation index is closer to 0 than ±0.1 and ±0.05, respectively, at $P < 0.01$ using one-tailed t-test. *, rejection of hypothesis that navigation index is 0 at $P < 0.01$ using two-tailed t-test. (For further experimental details, see Supplementary Figure 6.9). CS, Canton-S.

ure 6.2c). Throughout this study, we used a compass in which 0° indicates movement up the gradient (+*x* direction), 180° indicates movement down the gradient (-*x* direction), +90° indicates movement downwind, orthogonal to the gradient (+*y* direction) and -90° indicates movement upwind, orthogonal to the gradient (-*y* direction). To quantify the overall navigational response in each linear spatial gradient, we computed a navigational index by dividing the mean velocity of all larvae in the *x* direction, $\langle vx \rangle$, by the mean crawling speed $\langle s \rangle$. Hence, the navigational index was ± 1 if the larvae crawled uniformly straight up or down the gradient and 0 if the movement was unbiased. This index (Figure 6.2d) was significantly greater than zero ($P < 0.01$) across three ethyl acetate gradient steepnesses that we studied, indicating that chemotaxis toward ethyl acetate persists over two orders of magnitude in ethyl acetate concentration.

We did two control experiments without odorant, one in which the valves injected clean air into the laminar flow and one in which no laminar flow was provided (Figure 6.2d). In both cases, the navigational index in the *x* direction was 0. We also tested *Orco*^{1} larvae, which lack function in all olfactory neurons [16,17] and did not navigate ethyl acetate gradients (Figure 6.2d).

Next, we examined the response to CO_2, as gaseous repellant [18], in linear spatial gradients with different steepnesses. The navigational indices were negative (indicating repulsion) and depended strongly on steepness (Figure 6.2d). Reducing the steepness by 90% essentially abolished navigation away from CO_2. We verified that a loss-of-function mutation in *Gr63a*, a required CO_2 chemosensory receptor [13,18,19], disrupts CO_2 avoidance (Figure 6.2d).

To assess whether the larvae responded to the laminar airflow itself (that is, exhibited rheotaxis), we computed the orthogonal navigational index, the mean velocity of all larvae in the *y* direction divided by the mean crawling speed (Figure 6.2d). In all cases, orthogonal indices were approximately 0 and were not correlated with navigational indices in the gradient direction, indicating that airflow does not disrupt navigational response to the airborne cue.

6.5.3 Navigation in spatial gradients

What biases in the sequence of runs and turns along each trajectory enable the larvae to ascend ethyl acetate gradients (Figure 6.3) and descend CO_2 gradients

(Figure 6.4)? We describe the motion of larvae during runs by the magnitude (run speed) and direction (run heading) of the velocity vector. We calculated the fraction of time that larvae spent crawling in different directions on linear spatial gradients by making a histogram of run heading, and found that larvae spent the most time moving up ethyl acetate gradients and down CO_2 gradients (Figure 6.3b and Figure 6.4b). Larvae also crawled slightly faster when heading up ethyl acetate gradients than down and crawled slightly slower when heading up CO_2 gradients than down (Figure 6.3c and Figure 6.4c).

We examined the rate at which larvae initiated turns as a function of heading on linear spatial gradients, and found that the probability of larvae initiating a turn per unit time on linear gradients of ethyl acetate or CO_2 (Figure 6.3d and Figure 6.4d) was a smoothly varying function of heading with maximum at 180° or 0°, respectively. Thus, larvae extended runs in favorable directions, up gradients of ethyl acetate and down gradients of CO_2 (Figure 6.3e and Figure 6.4e). This strategy, termed the biased random walk, is also exhibited during *Escherichia coli* chemotaxis [20].

D. melanogaster larvae have been proposed to directly orient toward higher attractant concentrations during periods of forward movement [8]. To investigate whether larvae steer within runs, we compared headings at the end and beginning of each run. If larvae were steering toward more favorable directions during runs, we would expect that, on average, runs would end with more favorable headings than they began. We examined the angle change during runs (final heading minus initial heading) as a function of initial headings (Figure 6.3f and Figure 6.4f). The mean heading change (Figure 6.3h and Figure 6.4h) during runs was nearly zero regardless of initial heading, so larvae did not seem to orient themselves during runs.

To examine whether larvae modulate the size and direction of turns to augment the number of runs in a favorable direction, we examined the heading change effected by each turn (Video 5). When larvae turned after a run up or down either ethyl acetate or CO_2 gradients (Figure 6.3g and Figure 6.4g), the heading change distributions were bimodal and roughly symmetric but narrower when larvae were initially headed in the favorable direction. When larvae turned after a run oriented

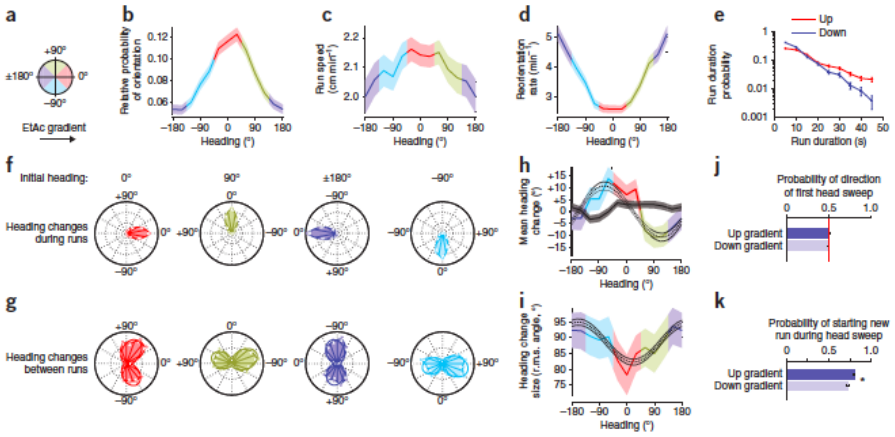

Figure 6.3: Navigation of a 2 p.p.m. cm^{-1} ethyl acetate concentration gradient. (a) Schematic of heading angles; 0° is toward higher concentration. For data in this figure, ten experiments, 202 *D. melanogaster* larva and 29 h of behavior were analyzed. (b) Relative probability of headings during runs. (c) Speed versus heading during runs. (d) Turn rate versus heading. (e) Durations of runs headed up (1,537 runs) or down (1,091 runs) gradients. (f) Heading changes during runs sorted by initial heading: up gradients (red, 1,499 runs), orthogonal with higher concentration to right (gold, 1,354 runs), down gradients (blue, 1,062 runs) and orthogonal with higher concentration to left (cyan, 1,184 runs). (g) Heading changes achieved by turns, sorted as in f on the basis of heading immediately before the turn (0°, 1,201 reorientations; 90°, 1,214 reorientations; 180°, 1,105 reorientations; -90°, 1,049 reorientations). (h) Mean heading change achieved by runs (black line) versus initial heading and turns (colored line) versus heading before turn. Shaded regions indicate ± s.e.m. (i) r.m.s. turn angle versus run heading before turn. Dashed and dotted lines in h,i represent prediction and 95% confidence interval of model (Supplementary Methods). (j,k) Statistics of head sweeps during turns after runs headed orthogonal to concentration gradient. Probability of direction of first head sweep (j; 1,967 head sweeps) and probability that larva initiates a new run during head sweeps (k; 2,341 head sweeps). Asterisk, rejection of hypothesis that probabilities are the same at $P < 0.01$ (Welch's *t*-test). Mean ± s.e.m. calculated as described in Supplementary Methods (b,c), mean ± s.e.m. derived from counting statistics (d-g,j,k) and mean ± s.e.m (h,i).

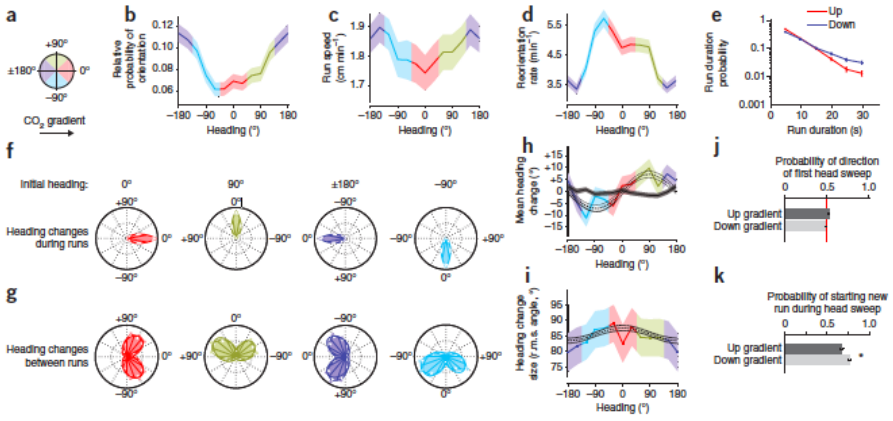

Figure 6.4: Navigation of a 2,500 p.p.m. cm^{-1} CO_2 concentration gradient. (a) Schematic of heading angles; 0° is toward higher concentration. For data in this figure, 21 experiments, 168 *D. melanogaster* larva and 31 h of behavior were analyzed. (b) Relative probability of headings during runs. (c) Speed versus heading during runs. (d) Turn rate versus heading. (e) Durations of runs headed up (1,494 runs) or down (1,866 runs) gradients. (f) Heading changes during runs sorted by initial heading: up (red, 1,484 runs), down gradients (blue, 1,844 runs), orthogonal with higher concentration to right (gold, 1,651 runs) and orthogonal with higher concentration to left (cyan, 1,664 runs). (g) Heading changes achieved by turns, sorted as in f on the basis of heading immediately before the turn (0°, 1,196 reorientations; 180°, 1,336 reorientations; 90°, 1,306 reorientations; -90°, 1,375 reorientations). (h) Mean heading change achieved by runs (black line) versus initial heading and turns (colored line) versus heading before turn. (i) r.m.s. turn angle versus run heading before turn. Dashed and dotted lines in h,i, prediction and 95% confidence interval, respectively, of model described in Supplementary Methods. (j,k) Statistics of head sweeps during turns after runs headed orthogonal to concentration gradient. Probability of direction of first head sweep (j; 2,497 head sweeps) and probability that the larva initiates a new run during head sweeps (k; 3,254 head sweeps). Asterisk, rejection of hypothesis that probabilities are the same at $P < 0.01$ (Welch's t-test). Mean ± s.e.m. calculated as described in Supplementary Methods (b,c), mean ± s.e.m. derived from counting statistics (d-g,j,k) and mean ± s.e.m. (h,i).

perpendicular to the gradient, they did so with the same distribution of angular sizes to the left or right, but made more turns toward the favorable direction. For any given initial heading, the angular distribution of heading changes after turns could be modeled as the sum of two skew-normal distributions (see Supplementary Methods).

To quantify how turns enhance orientation during navigation, we measured the moments of heading-change distributions as functions of initial heading. In contrast to the mean zero heading change achieved during runs, the mean heading change after turns (Figures 6.3h and Figure 6.4h) showed significant biases ($P < 0.01$ using the model described in Supplementary Methods) to orient the larvae toward higher concentration of ethyl acetate or lower concentration of CO_2 after orthogonal runs. The r.m.s. heading change (Figures 6.3i and Figure 6.4i) showed larger heading changes in turns after runs pointed toward lower ethyl acetate concentration or toward higher CO_2 concentration.

During a turn, a larva sweeps its head to one side, after which it either starts a new run or initiates a new head sweep (Figure 6.2 and Video 6). To uncover bias in these detailed head sweeping movements, we analyzed the statistics of all head sweeps initiated by larvae after runs pointed orthogonal to ethyl acetate or CO_2 gradients. In contrast to a recent report [9], we found that the direction of the initial head sweep in each turn was unbiased by gradient direction (Figures 6.3j and Figure 6.4j). However, the larva more often initiated new runs during head sweeps that pointed in the favorable direction (Figures 6.3k and Figure 6.4k).

6.5.4 Navigation in temporal gradients

The larva detects odors via the dorsal organ and CO_2 via the terminal organ [21]. Because right and left dorsal and terminal organs are separated by only approximately 10 μm, the larva probably detects spatial gradients by making temporal comparisons during its movements rather than by directly comparing the activity of the two sensory organs. Indeed, larvae with unilateral olfactory function exhibited chemotaxis toward volatile attractants8 nearly as well as larvae with bilateral olfactory function. We used our system to determine whether patterns of behavior exhibited on spatial gas gradients could be driven with temporal gradients of ethyl acetate or CO_2 concentration that were spatially uniform along the x axis

(Supplementary Figure 6.7 and Figure 6.1d). Triangular waveforms with linearly increasing and decreasing gas concentrations over time mimic the temporal stimulus experienced by a larva crawling in a straight line up or down a linear spatial gradient. When subjected to increasing concentration of CO_2 over time, larvae reoriented more frequently, crawled more slowly and turned with larger angles (Figure 6.5a) than when the concentration was decreasing, consistent with our observations of larvae on spatial gradients (Figure 6.4c,d).

We also explored sensorimotor response to CO_2 using step stimuli (Figure 6.5b,c). We found that a small temporal step change (increase or decrease) in CO_2 concentration produced a transient increase or decrease, respectively, in turning rate. Large steps in CO_2 concentration were less adaptive, producing a sustained change in the turning rate. Very small concentration change (to 0.25%) did not affect turning rate but modulated crawling speed. Crawling speed was slow to adapt for small concentration changes and did not adapt at all for large concentration changes. The fact that turning rate adapted differently than crawling speed might indicate differences in the sensorimotor pathways between CO_2 detection and the circuits that regulate crawling speed and turn initiation. To verify lack of adaptation to changes in CO_2, we extended the step waveform period to 480 s and still saw no evidence for adaptation in response parameters (Figure 6.5c). Mutants lacking the *Gr63a* sensor for CO_2 modulated their behavior minimally in response to temporal changes in CO_2 concentration (Figure 6.5c). Thus, CO_2-evoked changes in turning behavior and crawling speed were due to active sensorimotor responses and not a metabolic consequence of higher CO_2 concentration.

We examined larva behavior in temporal gradients of ethyl acetate. When larvae were subjected to a continuously increasing concentration of ethyl acetate over time, they reoriented less frequently and turned with smaller angles (Figure 6.5d), consistent with their behavior on spatial gradients (Figure 6.3c,d). Changes in crawling speed induced by linear ramps of ethyl acetate were not apparent (Figure 6.5d). In contrast to the response to step changes in CO_2 (Figure 6.5b,c), the response to step changes in ethyl acetate was adaptive across a wide range of concentrations (Figure 6.5e). A temporal step increase or decrease in ethyl acetate concentration produced, respectively, a transient decrease or increase in the rate

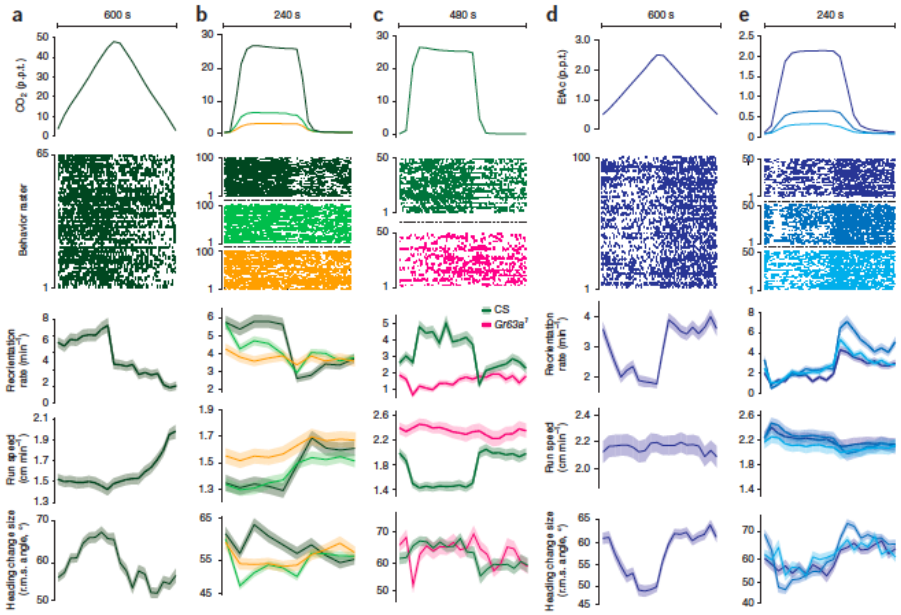

Figure 6.5: Temporal CO_2 and ethyl acetate gradients. (a-e) Statistics of turning decisions of larvae subjected to spatially uniform temporal gradients of CO_2 delivered as repeating cycles of triangle waves (a) and steps (b,c) and of ethyl acetate delivered as triangle waves (d) and steps (e). Top, one cycle of stimulus waveform. Raster plots, periods in which an individual larva was turning during the cycle; each row represents one larva tracked continuously through a cycle (a, n = 65; b, n = 100 for each condition; c, n = 50 for each condition; d,e, n = 100 for each condition). Bottom, turning rate (mean ± s.e.m.) derived from counting statistics, mean crawling speeds ± s.e.m. calculated as described in Supplementary Methods and root mean square heading change after turns ± s.e.m. versus time within each cycle. Data from wild-type larvae (CS) are in a,b,d,e. Step response of wild-type larvae and Gr63a1 mutant larvae are compared in c.

of turn initiation, slightly higher or lower crawling speeds and a transient decrease or increase in the size of turns (Figure 6.5e).

6.6 Discussion

Animals may sense the direction of a local gradient either directly, for example, by instantaneously comparing the activity of bilateral sensory organs or by decoding temporal signals generated by moving their sensory organs through the gradient. Here we found evidence for the latter for both odor and CO_2 gradients; larvae initiated turns more often when their forward movement caused an unfavorable change in concentration, and larvae based their turning decisions on the favorability of changes encountered during head sweeps, similar to our results in thermotaxis [13]. As in our studies of thermotaxis, we used time-varying spatially uniform signals to evoke behaviors observed in spatial gradients. We did not see signs of direct gradient measurement; specifically, larvae did not steer during runs and did not favor the preferred direction in the first head sweep of a turn. In experiments involving odor and agar substrates, some odorant can be absorbed into the gel. Substantial odorant absorption into the substrate could affect stimulus presentation during temporal gradients, but as *D. melanogaster* larva responded consistently to abrupt changes in odor concentration over the course of our experiments, any effect of odorant absorption was modest. Our ability to present rapid changes in odor concentration was slightly compromised by the design of the reservoirs in the apparatus, but the 10-90% rise time for a step change (20.8 s) was smaller than the bin sizes in Figure 6.5. The rise time can be decreased by redesigning the reservoirs or increasing the flow rate. In experiments in which we suddenly reversed the direction of the gradient (data not shown), larvae followed the new gradient direction rather than the old, also indicating that odorant absorption does not confound airborne navigation.

In navigation experiments, asymmetry with respect to the arena boundary can confound the results. For example, without stimulus, larvae placed at the left edge of a plate will show a navigational bias to the right because they are physically constrained from moving left. For this reason, we began each experiment with the larvae placed roughly in the center of the arena. Otherwise, as the spatial odor gradient in our apparatus is linear in the x direction, constant in the y direction and

steady in time, experiments in our apparatus are less sensitive to initial placement of the larvae than droplet-based assays.

Our apparatus flexibly and accurately provided airborne stimulants to freely moving larva. Using this apparatus and machine-vision analysis that is sensitive to time-varying position and posture of each larva, we analyzed the algorithmic structure of navigational behavior with precision. We determined the navigational strategies of larvae in response to ethyl acetate and CO_2, showed internal consistency between their behavioral response to spatial gradients and temporal gradients, and uncovered a nonadaptive response for temporal changes in CO_2. The marked similarities between the algorithmic structure of navigational strategies during chemotaxis and thermotaxis suggest that homologous sensorimotor circuits might be used to encode larval navigation in response to diverse sensory inputs [15].

6.7 Methods

6.7.1 Strains

Wild-type larvae were Canton-S (CS). *Gr63a* (Bloomington stock 9941) and *Orco*^{1} (Bloomington stock 23129) flies were obtained from the Bloomington stock center. *Orco* represents the new gene name for *Or83b* [17]. All behavioral experiments were done on second instar larvae. Adult flies were allowed to lay eggs on grape-juice agar growth plates with yeast for 3 h. After egg laying, plates were kept at 22°C on a 12 h day-night cycle. Experiments were carried out at 22°C during the day cycle or early hours of the night cycle. Time since egg laying was used to roughly stage larvae, and actual stage was verified by examining spiracle morphology.

6.7.2 Odor gradient apparatus

The odor gradient apparatus (Figure 6.1a) comprises a controlled clean air source, an odor source, an array of microcontroller-activated valves, a mixing flow block and a laminar flow chamber. Compressed air was regulated to 140 kPa and cleaned with a charcoal filter (Agilent HT200-4) before delivery to a computer-controllable mass-flow controller (MFC; Aalborg GFC 17). A second MFC was used to inject air-

borne chemical stimulants into the laminar airflow. For ethyl acetate experiments, the second MFC injected air into a bubbler made up of a 250-ml glass bottle with a stainless steel cap and frit, containing ethyl acetate (Mallinckrodt) either pure or diluted in deionized water. This generated an odorized air stream with the concentration of ethyl acetate in the air determined by the concentration of ethyl acetate in the bubbler. The water-ethyl acetate mixture does not obey Raoult's Law, so the ethyl acetate vapor pressure of the mixture was measured directly using a photoionization detector (PID; Baseline-Mocon Pidtech Plus). For CO_2 experiments, pure CO_2 was metered using an MFC calibrated for CO_2.

The carrier air was injected into the rear of the mixing flow block. For temporally varying, spatially uniform stimuli (Figure 6.1d and Supplementary Figure 6.7), the outlet of the odor source was connected to the inlet of the mixing block at the same location as the carrier air. The total amount of odor in the chamber was set by adjusting the flow rate of odor while holding the carrier flow rate constant (generally 2 min^{-1}). The odor concentration was monitored during each experiment at the inlet using either a PID or a nondispersive infrared CO_2 sensor (http://www.CO2meter. com/, GSS C20).

For spatially varying, temporally uniform stimuli (Figure 6.1b,c), the outlet of the odor source was connected to the inlet of the valve manifold. Compact solenoid valves (Lee, LHDA1221111H) were used to meter odor through a section of teflon tubing into each flow tube in the mixing block. The valves were controlled by a custom circuit board based on SpokePOV (Adafruit Industries) and were programmed to open for linearly increasing amounts of time over a period of approximately 1.5 s. The valves were operated in a pattern that kept exactly half open at any time, presenting a constant impedance to the MFC (Supplementary Figure 6.8). The minimum continuous time a valve was opened or closed was therefore approximately 50 ms, whereas the valve switching time was 3 ms. The mean concentration of the gradient was set by varying the ratio of odor flow to carrier air flow and was monitored at the outlet of the flow chamber by the appropriate gas sensor. Diffusion smooths odor profiles generated by the valves. Between the outlet of the mixing block and the start of the experimental arena, diffusion smooths the profile with a length scale of 1.2 cm for ethyl acetate and 1.7 cm for CO_2. By the far edge of the experimental arena, the smoothing length scale is 1.8 cm and 2.5 cm for ethyl acetate and CO_2, respectively. Thus, spatial irregularities owing to

the discrete injection points are relaxed by the time the laminar airflow enters the arena, but the gradient itself is not dissipated before the airflow exits the arena.

The laminar airflow containing spatial or temporal gradients of ethyl acetate or CO_2 passed through an experimental arena made from a solid piece of black anodized aluminum. A glass lid provided a viewing window for observing behavior. A hinged, pneumatic compressor was used to press the glass ring against an O-ring, creating a reliable seal. The integrity of all O-ring seals (at the inlet, outlet and glass lid) was continuously verified by monitoring the airflow rate at the outlet. Video microscopy of larvae within the experimental arena was done using dark-field illumination with red LEDs (624 nm, outside the range of larval phototaxis) that were mounted at the perimeter of the experimental arena. Video was recorded at 5 frames s-1 using a 5-megapixel USB camera (Mightex BCE-B050-U) and an 18-mm focal-length C-mount lens (Edmund Optics NT54-857). Each pixel in the captured images corresponded to a 0.063 mm x 0.063 mm square of the experimental arena.

6.7.3 Behavior experiments

Before each experiment, larvae were staged, washed in phosphate-buffered saline and placed on 10-cm Petri dish containing clean 1% (wt/vol) Bacto agar medium for at least 5 min to allow the larvae to adapt to the medium used in the experiments and shed any residual odorous contaminants. After each behavioral experiment, all larvae were discarded. The substrate for the behavioral experiments was a approximately 4-mmthick Bacto agar gel (1% wt/vol) on top of square, flat, black, anodized aluminum plates (24 cm x 24 cm). Each plate with the gel on top could be placed in the experimental arena, providing a large uniform substrate for the larvae to navigate without edges to impede or distort airflow. Larvae were transferred from 10-cm Petri dishes to experimental arena using a paintbrush, the chamber was pneumatically sealed and the entire apparatus was enclosed in a light-tight box. After the chamber was pneumatically sealed, it took approximately 30 s for the laminar airflow to fully purge the chamber and establish a defined spatial gradient. We discarded the first 2 min of recorded behavior during analysis. We recorded behavior for 25-30 min per experiment; for experiments involving spatial gradients, we analyzed the first 15 min (after the discarded 2 min), after

which larvae started nearing the edges of the gradients.

6.7.4 Behavioral analysis

The MAGAT analyzer software package is available at https://github.com/ samuellab/MAGATAnalyzer. Larval positions and postures were extracted from video records using custom machine vision software written in C++ and based on OpenCV, an open-source computer vision software suite. With similar features to software that has been written to automatically follow *C. elegans* behavior22-25, our software tracks each larva throughout the arena and records an image of the larva, the position of center of mass, the outline of the body, the position of the head and tail and a midline running down the center of the larva (Figure 6.2a and Supplementary Figure 6.6). Using data analysis software written in MATLAB (MathWorks),we analyzed navigational statistics such as path curvature, speed, heading and angle of head relative to body (Figure 6.2b). These were used to segment trajectories into an alternating sequence of runs and turns. To calculate statistics involving center-of-mass movement along larval trajectories (for example, distributions of instantaneous heading and speed in Figure 6.3b,c and Figure 6.4b,c and navigational indices in Figure 6.2d) we needed to estimate the number of independent observations of quantities of center-of-mass movement along each larval trajectory. To do this, we calculated the autocorrelation function of the direction of motion

$$C(\tau) = \left\langle \hat{v}(t) \cdot \hat{v}(t+\tau) \right\rangle_t$$

and extracted the time constant, T, of its component of exponential decay,

$$C(\tau) = e^{-\tau/T}$$

.

This correlation time constant was typically approximately 20 s. To calculate the s.e.m. of center-of-mass motion statistics, we estimated the number of independent observations as the total observation time for each measurement divided by twice the correlation time constant [23].

To calculate statistics of decision making along trajectories, trajectories were segmented into a sequence of alternating runs and turns. Runs (Video 4) were defined as continuous periods of forward movement with head direction aligned

with direction of forward travel (Figure 6.2b). A hysteretic threshold for run speed was determined on an individual *D. melanogaster* larva basis by examining the speed near points of high curvature in the path; the speed to begin a run was higher than the speed to end one. The head was considered aligned with the direction of forward motion if the angle between the mid-head vector and the heading was $<37^{\circ}$. Turns separated successive runs. The initiation of each head sweep (Video 6) during a turn was flagged when the body bend angle between the anterior and posterior of the *D. melanogaster* larva was $>20^{\circ}$ (Figure 6.2b). Each head sweep ended when the body bend angle was $<10^{\circ}$ or changed sign (head swept to other side of body) or when a new run began. Each turn ended at the start of a new run. Thus, each turn could involve zero or more head sweeps. Turns with zero head sweeps (pauses) were excluded from the statistics of reorientation after turns. Rare head sweeps in which the body bend angle was so extreme that the head touched the tail created difficulty during feature extraction because the tracker could no longer effectively distinguish head from tail. These head sweeps were also excluded from statistical analysis.

Video records of each larva along its trajectory could be played back, overlaid by extracted contour, head and tail locations, and path with annotations noting runs, turns and head sweeps (Videos 2 and 3). A subset of these videos was examined visually to verify the performance of automated segmentation and analysis of larval trajectories.

6.7.5 Statistical model for heading change distributions after turns

To describe the distribution of heading changes after turns, we developed a statistical model to represent our observation that heading changes, $\Delta\theta$, are biased in size and direction by head sweeping movements and contingent on the initial heading on spatial gradients before each turn, θ_i . In this model, the magnitude of heading change is drawn from skew-normal distributions whose mean and skewness depend on θ_i, thereby allowing the size of turns to depend on initial heading on spatial gradients as observed. The direction of heading change (to the left ($\Delta\theta > 0$) or right ($\Delta\theta < 0$)) is determined by a biased coin-flip distribution whose mean depends on θ_i, thus biasing the likelihood of initiating new runs to the left or right:

$$P(\Delta\theta|\theta_i) = \left(\frac{1}{2} - A\sin(\theta_i - \theta_0)\right) \times SN\left(\Delta\theta, \mu - B\cos(\theta_i - \theta_0),\right.$$
$$\left.\sigma, \alpha - C\cos(\theta_i - \theta_0)\right) + \left(\frac{1}{2} + A\sin(\theta_i - \theta_0)\right)$$
$$\times SN\left(-\Delta\theta, \mu - B\cos(\theta_i - \theta_0), \sigma, \alpha - C\cos(\theta_i - \theta_0)\right)$$

where

$$SN(x, \mu, \sigma, \alpha) = \frac{e^{-\frac{(x-\mu)^2}{2\sigma^2}}}{\sigma\sqrt{2\pi}} Erfc\left(\frac{-\alpha(x-\mu)}{\sigma\sqrt{2}}\right)$$

We adjusted the parameters of the model (A, B, C, μ, σ, α and θ_0) to maximize the likelihood of the observed initial heading-heading change pairs. The solid lines overlaying the histograms in Figure 6.3h and Figure 6.4h and dashed lines overlaying the plots of heading change magnitude and direction in Figure 6.3e,f and Figure 6.4e,f represent predictions of the model fit to the experimental data. For both ethyl acetate and CO_2, we assessed the statistical model represented by the above equations by also calculating the maximum likelihood of observed data given null models that eliminated certain features from the full statistical model by setting one or more parameters to zero. We computed the logarithm of the ratios of maximum likelihood for the null model and full statistical model. These results are summarized in Supplementary Figure 6.10. All null models could be rejected in favor of the full statistical model at $P < 0.01$.

6.7.6 Supplementary Methods

Construction Details and Logistics

The linear and dynamic gaseous gradient apparatus consists of these major components: a computer controllable source of carbon dioxide or odorant, a microcontroller actuated valve array for generating a stepwise linear gradient, a linear flow chamber where experiments are carried out, camera and lighting for observing and recording behavior, and ancillary structures for support, light management, and gas handling.

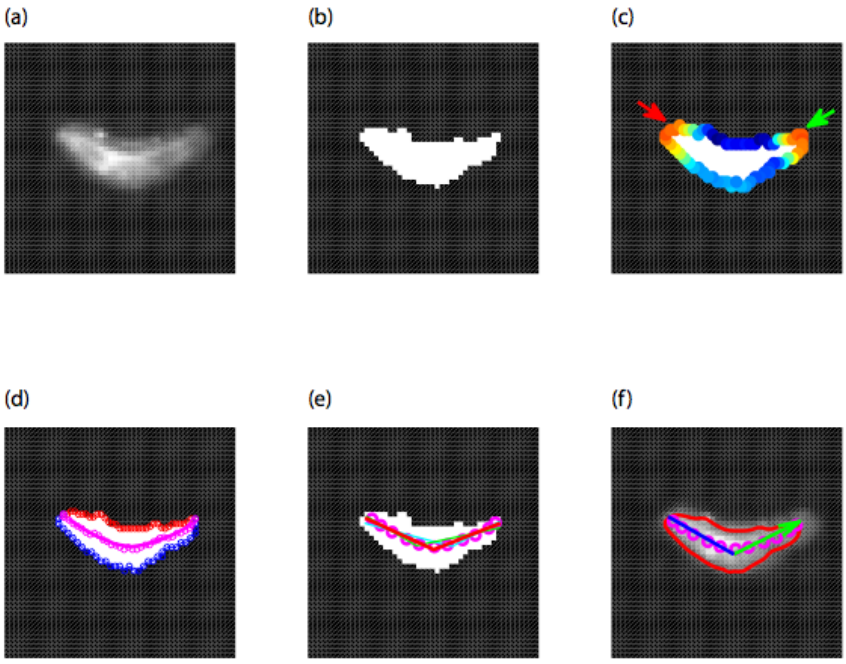

Figure 6.6: Feature Extraction during MAGAT Analysis. (a) Grayscale image of a larva. (b) thresholded image. (c) Contour of the larva with curvature indicated by color (red = highest curvature). Arrows indicate determined head/tail locations (at this stage of the analysis, the head is not differentiated from the tail). (d) Contour divided into two segments (red and blue) resampled to have equal numbers of points, midline (purple) is the point by point average of these two segments (e) points along the midline (purple circles) and prospective fits of the midline to two straight lines; the thicker red line fits best (f) grayscale image of the the larva overlaid by the contour (red line), midline (purple circles), and prospective tail-mid and mid-head lines.

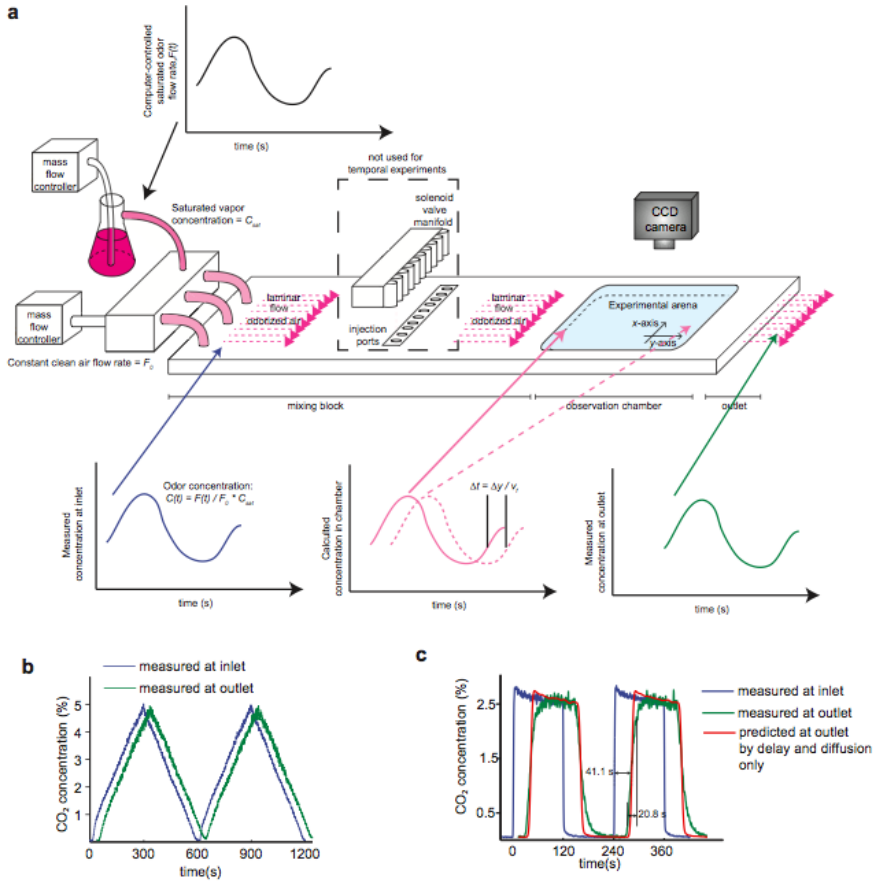

Figure 6.7: Temporal Gradients. (a) Schematic of setup for temporal gradient experiments. The valve array is bypassed. Odor/gas is combined with clean air prior to the device inlet. Gas concentration is manipulated by setting the flow rate of odor/gas relative to the flow rate of clean air. The concentration in the chamber is constant in the x-direction and varies in the y-direction as the temporal waveform flows across the chamber. The concentration at any point in the chamber can be calculated using the measured inlet concentration, the y-position and the gas flow rate (v_f). (b) Carbon dioxide concentration during triangle wave (same conditions as Figure 6.5a, reproduced from Figure 6.1). (c) Carbon dioxide concentration measured during square wave (same conditions as Figure 5b). 2 complete periods are shown. Blue line - concentration measured immediately upstream of the mixing block inlet . Green line - concentration measured immediately downstream of flow chamber outlet; Orange line - expected measurement at outlet taking into account diffusion and flow time from inlet to outlet. The time delay (41.1 s) agrees with the prediction obtained by dividing the chamber volume by the gas flow rate. The rise time (20.8 s) is longer than that predicted by diffusion.

Computer controlled odor/carbon dioxide source

The odor source is based around an AALBORG mass flow controller (MFC) and interfaces to the computer via a LabJack USB data acquisition device. We use Labview to control the LabJack, but drivers are available for a number of programming languages. For carbon dioxide delivery, the MFC is calibrated for CO_2 and used to meter gas directly to the valve array device (for spatial gradients) or to the flow chamber inlet (for temporal gradients). For odor delivery, the MFC is calibrated for and used to meter clean air into a bubbler, which then connects to the valve array or the flow chamber inlet. A second MFC controlled by the same LabJack is used to provide carrier air flow. The odor source can be made from off-the-shelf components in less than one day. Familiarity with compression fittings (e.g. Swagelok) is required as is some basic computer programming.

Microcontroller actuated valve array

The valve array consists of 29 Lee company LHD Series miniature solenoid valves mounted on a custom-machined gas handling manifold, a custom designed circuit board, and a flow block to mix the output of the valves with air prior to delivery to the flow chamber. The valve manifold is connected to the mixing block via Teflon tubing and secured using 10-32 flat bottom fittings, both from Upchurch Scientific.

We estimate that machining of the manifold, mixing block, outlet and accessories will require 20-30 hours of machine shop time. The circuit board can be ordered from a PCB manufacturing company (we favor Advanced Circuits) with a lead time of 5 days and requires a few hours of soldering to assemble. Source code to program the microcontroller is included on the website.

The valve array as we constructed it requires a good deal of custom work. However, there are opportunities for later iterations to use more off-the-shelf or user-friendly components. In particular, one might take advantage of the increasing availability of USB-programmable microcontroller development boards (e.g. the Arduino and the Teensy) and also of the number of manifolds the lee company makes to fit its LHD Series solenoid valves.

Assembly of the components into the completed valve array will require a day of work, with an hour or two devoted to cutting the tubing to length and attaching

the fittings securely in a somewhat confined space. Some soldering, microcontroller programming, and mechanical assembly are required.

Valve timing algorithm

The valves are timed so that each valve is open for one continuous block of time during each duty cycle (1 second). To create a linear gradient, the length of time each valve is open is linearly proportional to its position in the array. The valves are opened and closed at specific times during the duty cycle so that exactly half are open at any one point. A simple graphical algorithm for generating a valve timing sequence that achieves these goals for N valves is as follows: Take a sheet of graph paper and mark off an NxN block of squares. Each column represents a valve and each row represents a fraction (1/N) of the duty cycle. Place a single *x* in the upper left box. This indicates valve 1 is open for the first fraction of the duty cycle only. Now move down and to the right one box and place two Xs in the second column in rows two and three, indicating that valve 2 is open for the second and third fractions of the duty cycle. Repeat this process, marking M boxes in column M, beginning with the box to the lower right of the last box marked in column M-1. When you reach the bottom row, wrap back to the top row and continue marking. The finished graph paper is a valve timing diagram; each valve is open for the portion of the duty cycle marked with Xs. An example of this timing diagram for 29 valves is shown in Supplementary Figure 6.8.

Flow/Observation Chamber

The flow chamber is machined from a solid block of aluminum and anodized. Plans are available on the website. We estimate 10 hours of shop time to machine the flow block. A glass lid (available from any glass shop) is sealed to the roof of the flow chamber using an o-ring seal. To compress the glass against the o-ring we built a custom pneumatic hinge from 80/20 *t*-slot extrusion. Assembly of the pneumatic hinge and connection of the flow cell to the mixing block and outlet will take less than half a day and requires no special expertise.

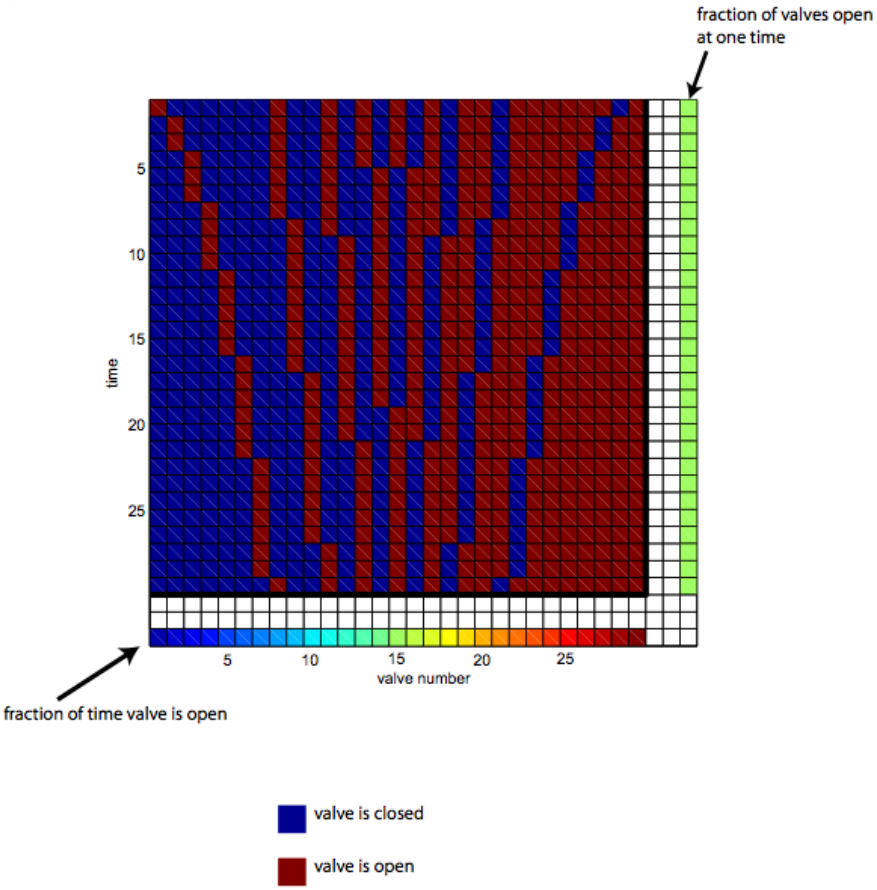

Figure 6.8: Valve timing diagram. Time in the cycle progresses vertically from top to bottom, valve number increments horizontally from left to right. Blue squares indicate the valve is closed at a particular time in the cycle, red squares that the valve is open.

Supplemental Table 1: Numbers of experiments and animals and observation times for Figure 2d

Genotype	Odorant	Steepness	n experiments	n animals	hours of behavior
CS	EtAc	20 p.p.m. cm^{-1}	4	87	10.6
CS	EtAc	2 p.p.m. cm^{-1}	10	202	29.2
CS	EtAc	0.2 p.p.m. cm^{-1}	4	89	14.3
CS	clean air	n/a	8	56	10.4
CS	no airflow	n/a	5	90	14.2
Or83b^{1}	EtAc	2 p.p.m. cm^{-1}	4	78	12.4
CS	CO_2	2,500 p.p.m. cm^{-1}	21	168	31.4
CS	CO_2	1,000 p.p.m. cm^{-1}	5	90	16.3
CS	CO_2	500 p.p.m. cm^{-1}	6	85	15.1
CS	CO_2	250 p.p.m. cm^{-1}	9	92	17.8
Gr63a^{1}	CO_2	2500 p.p.m. cm^{-1}	10	84	14.7

Figure 6.9: Numbers of experiments and animals and observation times for Figure 6.2d

6.7.7 Camera and Lighting

Lighting is provided by a set of red LEDs (624 nm, 30 degree, CREE C503B-RCNCW0Z0AA1) mounted on the pneumatic hinge. We were unsatisfied with commercially available led light sources, so we fabricated our own. We used a 5 megapixel USB 2.0 camera from Mightex, but any high pixel density camera that supports a frame rate of at least 5 Hz may be used. We favored the Mightex camera for its low cost, but others might choose a more user friendly camera that features better integration with third party software. Assembly of the light bars requires cutting the PCB and spending a few hours soldering. Mounting the light bars and the camera to the setup requires less than an hour.

Support Structure

To exclude light and provide rigid support for the camera and apparatus, we constructed an enclosure from 80/20 *t*-slotted extrusion and ABS paneling. Plans and a list of materials for this enclosure are included in the Supplementary Methods. The camera was connected to the enclosure using standard optical mounting components from Thorlabs. We found that a blackout curtain attached to the front of the enclosure with Velcro was the most convenient way to block light from the experiment while maintaining ease of access. Depending on one's familiarity with *t*-slot extrusion, assembly of the enclosure will take between an hour and half a day.

Supplementary Table 2: Fit of statistical model to reorientation after turning decisions

Description of null model	Parameter(s) set to zero	Change in log-likelihood of fit to navigational data	
		EtAc gradients (Figure 3)	CO_2 gradients (Figure 4)
No bias in turn direction	A	-19.3 ($p<0.01$)	-12.3 ($p<0.01$)
No bias in turn magnitude	B,C	-30.2 ($p<0.01$)	-4.8 ($p<0.01$)
No skew	σ,C	-23.5 ($p<0.01$)	-132.0 ($p<0.01$)
No bias	A,B,C	-51.8 ($p<0.01$)	-17.8 ($p<0.01$)

Recall:

$$P(\Delta\theta|\theta_i) = (\frac{1}{2} - A\sin(\theta_i - \theta_0)) \times SN(\Delta\theta, \mu - B\cos(\theta_i - \theta_0), \sigma, \alpha - C\cos(\theta_i - \theta_0))$$
$$+ (\frac{1}{2} + A\sin(\theta_i - \theta_0)) \times SN(-\Delta\theta, \mu - B\cos(\theta_i - \theta_0), \sigma, \alpha - C\cos(\theta_i - \theta_0))$$

where

$$SN(x, \mu, \sigma, \alpha) = \frac{e^{\frac{-(x-\mu)^2}{2\sigma^2}}}{(\sigma\sqrt{2\pi})} Erfc\left(\frac{-\alpha(x-\mu)}{\sigma\sqrt{2}}\right)$$

Figure 6.10: Fit of statistical model to reorientation after turning decisions.

Gas handling and additional materials

The apparatus requires at a minimum a source of clean compressed air at approximately 20 psi. Additionally, for carbon dioxide experiments, a source of compressed carbon dioxide at similar pressure is required. For carbon dioxide experiments, no special handling of the exhaust is required, but for ethyl acetate or other volatile odorants, it may be desirable to vent the exhaust outside the lab to avoid disturbing other experiments. If toxic odorants are used, special handling is required, probably involving placing the apparatus in a fume hood. In addition to the materials mentioned in the preceding section, assembly of the apparatus will require a standard assortment of fittings, valves, tubing, and hardware. Low pressure regulators can be desirable, especially as building compressed air and carbon dioxide are often delivered at higher pressures than desirable. We filter our building's compressed air with an activated charcoal filter and use a photoionization detector to verify it is free of volatile organic compounds. Finally, a flow meter on the outlet of the observation chamber is essential for verifying a proper seal, and other flow meters may be useful during setup. Final assembly and testing of the apparatus can be completed in one to two days depending on the number of problems (e.g. leaky connections) revealed by testing.

6.7.8 Calibration of Temporal Gradients

The measurement scheme used to calibrate the spatial gradient cannot be used to measure the temporal gradients as the equilibration time of detectors placed in the ceiling of the flow chamber is roughly one minute, significantly longer than the time it takes to change odor concentration in the flow chamber. However, the detectors integrated directly into the flow stream at the inlet and outlet can achieve fast response times. For all temporal experiments, we continuously monitored the odor concentration at the inlet. These measurements are shown (averaged over repeated trials) as the concentration in Figure 6.5.

To calibrate the effects of diffusion and mixing in the chamber we used carbon dioxide and placed a second detector on the outlet of the chamber. We provided a square wave of carbon dioxide varying from 0 to 2.5% with a 240 second period (Supplementary Figure 6.7c, the conditions of Figure 6.5b). At the inlet to the chamber we measured a 10-90% rise time of 1.4 seconds, and a 90-10% fall time of 2.2 seconds (both of these measurements likely also reflect the response times of the NDIR detector, which is not designed to operate at high speeds). Based on the volume of the chamber between the inlet and outlet and the set flow rate, we would expect 41.3 seconds to pass between detection of the carbon dioxide step at the inlet and outlet detectors. We measure this time to be 41.1 seconds. Based on the concentration at the inlet, the flow speed of gas in the chamber, and the diffusion constant of carbon dioxide, we would expect a rise time of 7.3 seconds at the outlet and a fall time of 9.0 seconds. In fact, we measure these times to be 20.8 seconds and 33.5 seconds. This likely reflects the presence of unswept (dead) volumes in the inlet and outlet reservoirs. Future iterations of Lady Gaga will remove this dead volume to eliminate these lags. In any case, the rise time at the outlet is greater than the rise time in the flow chamber as the latter involves only the dead volume in the inlet chamber. The data presented in Figure 6.5 has a minimum temporal bin size of 24 seconds, so the bin size is approximately equal to or greater than the rise time within the flow chamber.

We also produced a 10 min triangle wave of carbon dioxide with a peak concentration of 5% (the conditions of Figure 6.5a). The concentration at the outlet registered with the same delay as for the square wave, and we could see no distortion of the wave form due to diffusion or mixing (Supplementary Figure 6.7b,

Figure 6.1d).

6.7.9 MAGAT analyzer algorithms

Analysis of larval behavior proceeds in two stages. In the first, the larva's position and posture are extracted from video records by a feature extractor written in C++ using the openCV library. In the second, descriptions of the paths, including speed, posture, heading angle, and segmentation into runs and turns are done using custom MATLAB scripts. Separating the tasks in this fashion allows the most computationally intensive tasks to run quickly as compiled software while allowing rapid development and flexible access using the scripted MATLAB language.

Machine Vision Algorithm (C++)

Raw data is supplied to the feature extraction software as a sequence of still images. In the experiments described here, frames were acquired at a rate of 5 Hz, but because analysis takes place offline, any frame rate is supported.

The feature extractor assumes dark field illumination - larvae are always brighter than the surface on which they travel. Thus the first step of feature extraction is to determine a background by taking the minimum value of each pixel over a sequence of images. This sequence could be the entire recording, but to avoid errors from gradual shifts in light levels we recalculate the background every 40 seconds (200 frames). Once the background is determined, we subtract it from each image in the sequence.

In the first pass of feature extraction, bright spots in the background subtracted image are assembled into individual animal tracks. In every frame, each spot whose brightness and area exceed user defined thresholds is either added to an existing track or forms the start of a new track. A bright spot is added to an existing track if that track's terminus at the previous frame was closer to this point than any other and if that distance is below a user-defined threshold (this prevents tracks that end from jumping to new, unrelated points). In the case where two tracks converge to the same bright spot, we attempt to rethreshold the single bright spot to produce two independent spots. When this can be done, both tracks continue to their respective spots. When this proves impossible, both tracks are terminated. After this sequence, any remaining bright spots begin their own tracks. Each track

consists of a sequence of points representing the center of mass of the spot and a sequence of images of the bright spot and surrounding region.

In the second pass of feature extraction, we determine the outer contour, midline, and head and tail locations for each tracked larva. Proceeding in two steps allows us to use the entire sequence of images to determine features that are common to all images in the sequence, e.g. the size of the animal. This also allows flexibility in development. To analyze the posture of a different animal, e.g. *C. elegans*, we only need to modify this portion of the code as the first-pass track extraction is indifferent to the type of animal. The first step of larval posture analysis is to use the entire set of images to determine the size of the larva (in pixels). Subsequently each image in the track is thresholded to produce a white region of the appropriate size on a black background (Supplementary Figure 6.6b). Thus the analysis is insensitive to changes in overall illumination that may occur as the larva explores a large surface. The border of the white thresholded region is the contour of the larva. We determine the head and tail locations by finding the two "pointiest" regions on the contour separated by at least 1/4 the total perimeter of the contour (Supplementary Figure 6.6c). If the tracker cannot find exactly two separated pointy regions (as for instance if the larva touches its head to its tail forming a circle), the point is flagged. The midline is determined by dividing the contour up into two segments with an equal number of points between the head and tail and then taking the point-by-point average of these two segments (Supplementary Figure 6.6d). Head-tail identity is determined by minimizing the distance between corresponding midline points from one frame to the next and by the rule that the tail to head direction is generally parallel to the direction of motion, ignoring head-tail indeterminate images. The body bend angle is calculated by finding two lines that best fit the midline and taking the angle between them (Supplementary FIgure 6.6e).

Behavioral Analysis (MATLAB)

When experimental data is loaded into MATLAB, we supply a calibration file (generated by taking an image of a 1 cm checkerboard in the behavioral arena) to turn pixel locations in the image into real units, removing lens distortion in the process. We also supply a metadata file containing information about externally supplied

stimuli, e.g. when odor concentration varies temporally over the course of an experiment.

Experimental data is loaded into MATLAB as a sequence of tracks. Each track has a sequence of points. Each point describes the position and posture of a larva at a single point in time. The MATLAB analysis scripts use these sequences of points to generate time varying descriptions of the animals' behavior. The velocity vector is a lowpassed derivative of the midpoint position, the heading angle is the four quadrant arctangent of the velocity vector, the body bend angle is the angle between the tail-mid and mid-head lines, and so on.

Optionally, we discard tracks that likely contain invalid data. For instance, tracks with near zero speed and frequently indeterminate head-tail positions may represent dust that has fallen on the arena lid or a larva that has found a crevice in the agar into which it can burrow. Animals that continuously circle in one direction may have motor defects that interfere with their ability to navigate.

Finally, the sequence of behavioral data is turned into a sequence of behaviors by segmenting the tracks into runs and turns. Runs are defined as continuous periods of forward movement with the head direction aligned with the direction of forward travel. Turns separate successive runs. The initiation of each head sweep during a turn is flagged when the body bend angle between the anterior and posterior of the animal exceeds 20°. Each head sweep ends when the body bend angle drops below 10°, changes sign (the head swept to the other side of the body), or a new run begins. Each turn ends at the start of a new run. Thus, each turn can involve zero or more head sweeps. Head sweeps that begin a new run are termed "accepted." Head sweeps that are followed by another head sweep or by the straightening of the body without forward movement are "rejected." The MATLAB script keeps track of the time indices defining each run, turn, and headsweep and calculates metrics like run length, mean run heading, and number of head sweeps and change in angle achieved by a turn. Thus we can determine the answers to questions like "what is the mean speed of runs headed perpendicular to the gradient and lasting at least 15 seconds?" or "how likely is a head sweep to the left to be accepted given the larva was previously headed at 30 degrees to the gradient direction?" We can also return to the original sequence of images that determine a particular track and play back all or part of the image sequence overlaid by our analysis results. The software is capable of arbitrary playback - thus we can ask

to see all rejected headsweeps to the left and the 3 seconds preceding them or all points at which the tracker thinks the larva executed a turn with no headsweeps. This feature allows us to make sure that our analysis has produced results that align with what we would produce were we to score the behavior by hand (an impossible task, given the hundreds of hours of maggot tracks analyzed here).

6.8 Videos

6.8.1 Video 1

Overview of video analysis steps. Video shows in sequence (1) raw image of larvae in a 2ppm cm^{-1} EtAc gradient (gradient increases in concentration to the right) (2) individual larvae are all tracked separately (colored tracks show movement history, circles indicate current position) (3) for each larva, we find a contour, midline, head and tail (4 larvae shown as examples) (4) from extracted position and postural features, we derive metrics (speed, body bend angle shown here) and behavioral states (1 larva shown as an example). At default playback speed of 30 frames per second (fps), video is 6 x real time.

6.8.2 Video 2

Video complement to Figure 6.2a,b. Video sequence of still images depicted in Figure 6.2a, accompanied by navigational metrics (speed, dot product between head direction and direction of forward movement, body bend angle) presented in Figure 6.2b. Cyan dot on each data plot shows value associated with current frame. Text overlay on video shows elapsed time (time matches that shown in Figure 6.2a,b) and behavioral state. As in Figure 6.2b, colored regions under data plots indicate behavioral state. At default playback speed of 10 fps, video is 2 x real time.

6.8.3 Video 3

Extended playback of track excerpted in Video 2. Video sequence, accompanied by navigational metrics (speed, dot product between head direction and direction of forward movement, body bend angle). Cyan dot on each data plot shows value associated with current frame. Text overlay on video shows elapsed time (time

matches that shown in Figure 6.2a,b) and behavioral state. As in Figure 6.2b, colored regions under data plots indicate behavioral state. At default playback speed of 25 fps, video is 5 x real time.

6.8.4 Video 4

Example of runs and turns. Larva's track over video period indicated by white dots. As the video show the larva moving along the track, portions of the trajectory corresponding to runs and turns are indicated. At default playback speed of 25 fps, video is 5 x real time.

6.8.5 Video 5

Description of turn angles. The same larva and track from Video 4 are shown. As the video plays, the prior heading angle (orange θ) and heading angle change (green $\Delta\theta$) are graphically indicated for each turn. Figure 6.3g and Figure 6.4g show distributions of $\Delta\theta$, sorted according to θ. Figure 6.3h and Figure 6.4h show the mean of $\Delta\theta$ versus θ. Figure 6.3i and Figure 6.4i show the root mean square of $\Delta\theta$ versus θ. At default playback speed of 25 fps, video is 5 x real time (except for pauses to highlight turn angles).

6.8.6 Video 6

Example of rejected and accepted head sweeps. A portion of the video and track shown in Videos 4, 5; the larva executes at rejected head sweep to its left followed by an accepted head sweep to its right. At default playback speed of 10 fps, video is 2 x real time (except for pauses to highlight head sweeps).

6.9 Acknowledgements

We thank E. Soucy and J. Greenwood for engineering advice and suggestions. This work was supported by a US National Institutes of Health (NIH) Pioneer award to A.D.T.S., NIH grants to J.R.C. and an NIH National Research Service award to E.A.K.

6.10 Author contributions

M.G. designed and constructed the linear and dynamic gaseous gradient apparatus, designed and wrote MAGAT analyzer software, designed and carried out experiments, analyzed all data and assembled figures. M.B. designed and carried out experiments. D.M. and L.L. designed and carried out preliminary experiments. E.A.K. designed experiments. J.R.C. and A.D.T.S. supervised the project and designed experiments. M.G., E.A.K. and A.D.T.S. wrote the manuscript.

6.11 References

1. Brody, C.D. Hopfield, J.J. Simple networks for spike-timing-based computation, with application to olfactory processing. Neuron 37, 843-852 (2003).

2. Cleland, T.A. Linster, C. Computation in the olfactory system. Chem. Senses 30, 801-813 (2005).

3. Hopfield, J.J. Olfactory computation and object perception. Proc. Natl. Acad. Sci. USA 88, 6462-6466 (1991).

4. Chalasani, S.H. et al. Dissecting a circuit for olfactory behaviour in *Caenorhabditis elegans*. Nature 450, 63-70 (2007).

5. Masse, N.Y., Turner, G.C. Jefferis, G.S. Olfactory information processing in Drosophila. Curr. Biol. 19, R700-R713 (2009).

6. Bargmann, C.I., Hartwieg, E. Horvitz, H.R. Odorant-selective genes and neurons mediate olfaction in *C. elegans*. Cell 74, 515-527 (1993).

7. Kreher, S.A., Mathew, D., Kim, J. Carlson, J.R. Translation of sensory input into behavioral output via an olfactory system. Neuron 59, 110-124 (2008).

8. Louis, M., Huber, T., Benton, R., Sakmar, T.P. Vosshall, L.B. Bilateral olfactory sensory input enhances chemotaxis behavior. Nat. Neurosci. 11, 187-199 (2008).

9. Gomez-Marin, A., Stephens, G.J. Louis, M. Active sampling and decision making in Drosophila chemotaxis. Nat. Commun. 2, 441 (2011).

10. Chronis, N., Zimmer, M. Bargmann, C.I. Microfluidics for in vivo imaging of neuronal and behavioral activity in *Caenorhabditis elegans*. Nat. Methods 4, 727-731 (2007).

11. Lockery, S.R. et al. Artificial dirt: microfluidic substrates for nematode neurobiology and behavior. J. Neurophysiol. 99, 3136-3143 (2008).

12. Albrecht, D.R. Bargmann, C.I. High-content behavioral analysis of *Caenorhabditis elegans* in precise spatiotemporal chemical environments. Nat. Methods 8, 599-605 (2011).

13. Jones, W.D., Cayirlioglu, P., Kadow, I.G. Vosshall, L.B. Two chemosensoryreceptors together mediate carbon dioxide detection in Drosophila. Nature 445, 86-90 (2007).

14. Cayirlioglu, P. et al. Hybrid neurons in a microRNA mutant are putative evolutionary intermediates in insect CO_2 sensory systems. Science 319, 1256-1260 (2008).

15. Luo, L. et al. Navigational decision making in Drosophila thermotaxis. J. Neurosci. 30, 4261-4272 (2010).

16. Larsson, M.C. et al. Or83b encodes a broadly expressed odorant receptor essential for Drosophila olfaction. Neuron 43, 703-714 (2004).

17. Vosshall, L.B. Hansson, B.S. A unified nomenclature system for the insect olfactory coreceptor. Chem. Senses 36, 497-498. (2011).

18. Faucher, C., Forstreuter, M., Hilker, M. de Bruyne, M. Behavioral responses of Drosophila to biogenic levels of carbon dioxide depend on life-stage, sex and olfactory context. J. Exp. Biol. 209, 2739-2748 (2006).

19. Kwon, J.Y., Dahanukar, A., Weiss, L.A. Carlson, J.R. The molecular basis of CO_2 reception in Drosophila. Proc. Natl. Acad. Sci. USA 104, 3574-3578 (2007).

20. Berg, H.C. Brown, D.A. Chemotaxis in Escherichia coli analysed by three-dimensional tracking. Nature 239, 500-504 (1972).

21. Vosshall, L.B. Stocker, R.F. Molecular architecture of smell and taste in Drosophila. Annu. Rev. Neurosci. 30, 505-533 (2007).

22. Baek, J.H., Cosman, P., Feng, Z., Silver, J. Schafer, W.R. Using machine vision to analyze and classify *Caenorhabditis elegans* behavioral phenotypes quantitatively. J. Neurosci. Methods 118, 9-21 (2002).

23. Cronin, C.J., Feng, Z. Schafer, W.R. Automated imaging of *C. elegans* behavior. Methods Mol. Biol. 351, 241-251 (2006).

24. Swierczek, N.A., Giles, A.C., Rankin, C.H. Kerr, R.A. High-throughput behavioral analysis in *C. elegans*. Nat. Methods 8, 592-598 (2011).

25. Ramot, D., Johnson, B.E., Berry, T.L.J., Carnell, L. Goodman, M.B. The Parallel Worm Tracker: a platform for measuring average speed and drug-induced paralysis in nematodes. PLoS ONE 3, e2208 (2008).